A Vortex-particle Mesh Method for Large Eddy Simulation of Bluff Body Aerodynamics

PhD Thesis

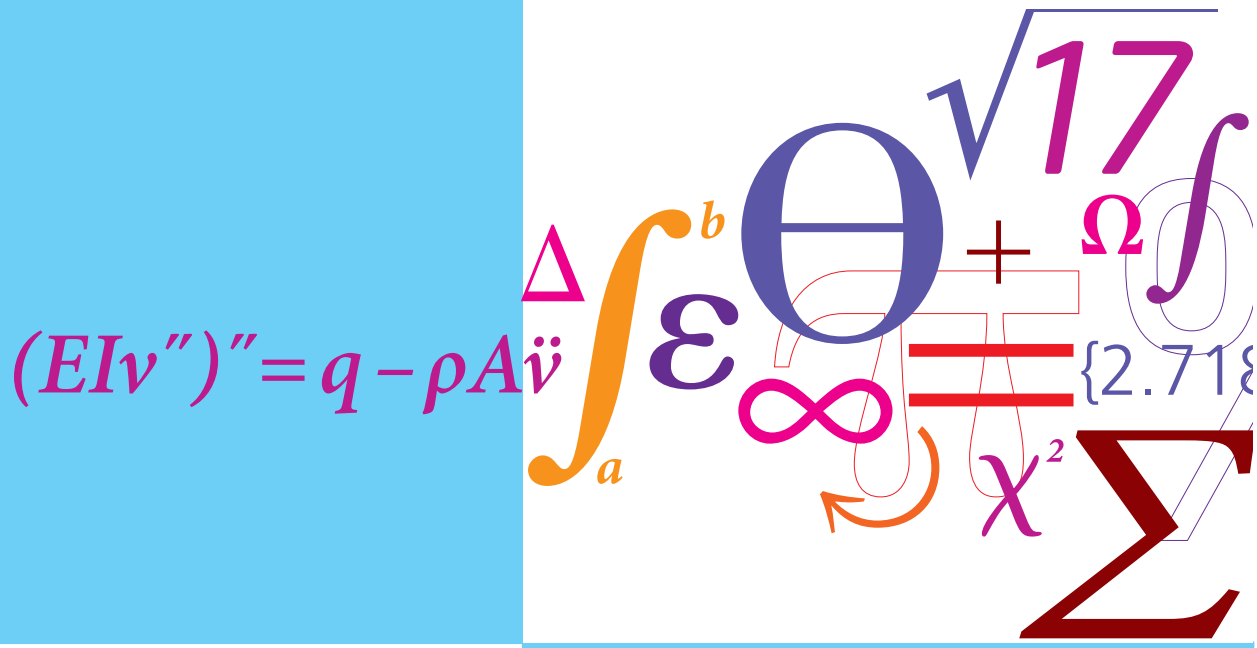

Henrik Juul Spietz
DCAMM Special Report No. S248
June 2018

DTU Mechanical Engineering
Department of Mechanical Engineering

A Vortex-particle Mesh Method for Large Eddy Simulation of Bluff Body Aerodynamics

by
Henrik Juul Spietz

A dissertation submitted for the degree of Philosophiae Doctor
at the Technical University of Denmark

Dissertation by:
Henrik Juul Spietz

Supervisor:
Jens Honoré Walther

Institution:
Section for Fluid Mechanics, Coastal and Maritime Engineering
Department of Mechanical Engineering
Technical University of Denmark

Nils Koppels Allé, Building 403
DK-2800, Kgs. Lyngby, Denmark

Report type:	Ph.D. dissertation.
Project period:	April 1, 2015 – June 30, 2018
Field:	Fluid Mechanics
Classification:	Unclassified
Revision:	Last edited on: October 20, 2018
Remarks:	This dissertation is submitted as a partial fulfillment of the requirements for the degree of Philosophiae Doctorat the Technical University of Denmark.

Preface

This dissertation concludes the work carried out in a Ph.D. project at the Department of Mechanical Engineering at the Technical University of Denmark during the period April 1, 2015 – June 30, 2018. The content of this dissertation is original work where most parts have been published in scientific journals or presented at conferences.

Published journal papers

1. **Spietz, H. J.**, Hejlesen, M. M., Walther, J. H., 2017. *Iterative Brinkman penalization for simulation of impulsively started flow past a sphere and a circular disk.* J. Comput. Phys. 336, 261–274.

2. **Spietz, H. J.**, Hejlesen, M. M., Walther, J. H., 2018. *A regularization method for solving the Poisson equation for mixed unbounded-periodic domains.* J. Comput. Phys. 356, 439–447.

3. Ramos-García, N., **Spietz, H. J.**, Sørensen, J. N., Walther, J. H., 2018. *Vortex simulations of wind turbines operating in atmospheric conditions using a prescribed velocity-vorticity boundary layer model.* Wind Energy 21 (11), 1216–1231.

Structure of the dissertation

The dissertation proceeds chapter by chapter as the complexity of the presented numerical model increases: Chapter 1 introduces a Fourier-based Poisson solver for a mixture of unbounded, periodic and homogeneous Dirichlet or Neumann boundary conditions. Chapter 2 outlines the base flow solver; a vortex-particle method for incompressible fluid flow simulation in the absence of solid bodies. The method relies on the Poisson solver from Chapter 1. In Chapter 3 the method is extended to three dimensional flow past solid bodies using the iterative Brinkman penalization technique. The method is applied for low Reynolds number ($\mathrm{Re} \leq 10^3$) and simple shapes. Local refinement using a multiresolution formulation of the Poisson solver and multilevel particle-vorticity redistribution is presented in Chapter 4. The procedure is verified by simulating the Taylor-Green vortex in 3D and the transitional flow past a 3D section of a circular cylinder. Chapter 5 regards large-eddy-simulation and subgrid-scale stress modeling based on a Smagorinsky model and a Lagrangian averaged dynamic variation of this. These are tested for simulating homogeneous turbulence and the flow past a square cylinder at a moderate Reynolds number ($\mathrm{Re} \geq 10^4$). Chapter 6 describes an application of the method for numerical investigation of aerodynamic instability.

Acknowledgements

Much of I work carried out has been a continuation of work initiated by Mads Mølholm Hejlesen, to whom I am thankful for everything from coding assistance to co-authorship and for being available for discussions even after his departure from the Technical University of Denmark (DTU). Also, the patient guidance of my supervisor Prof. Jens Honoré Walther has

been much appreciated. Further, I would like to thank Néstor Ramos-García from the Department of Wind Energy at DTU and Allan Larsen from COWI A/S for the interest they have taken in the project and its applications. To FORCE Technology and Søren Vestergaard Larsen for putting one of their wind tunnels at our disposal for experiments. Finally, my fellow PhD students at from the Section for Fluid Mechanics, Coastal and Maritime Engineering and from the Department of Wind Energy deserve a special thanks for constituting a positive and humorous work environment throughout the duration of the project.

The research presented in this dissertation has been funded by the Danish Council for Independent Research grant no. 4184–00349B.

Henrik Juul Spietz
DTU, Kgs. Lyngby, Denmark
June 2018.

Resumé (in danish)

En vortex-partikel net metode, der gør brug af net med lokalt forfinet opløsning, præsenteres til beregning af strømninger om faste legemer vha. Brinkman penalisering.

Vortex-partikel net metoden beror på regularisede Greens funktioner til løsning af Poisson ligningen med åbne randbetingelser. Poisson-løseren er baseret på foldningsmetoden af Hockney and Eastwood (1988) og udvidet til at omfatte kombinerede periodiske- og homogene Dirichlet eller Neumann randbetingelser. Mix af åbne- og periodiske betingelser opnås via teknikken af Chatelain and Koumoutsakos (2010), hvor Poisson ligningen først Fourier transformeres i de periodiske retninger. Dernæst løses en modificeret Helmholtz ligning af reduceret dimensionalitet for hvert diskrete bølgetal. Raten hvormed fejlen aftager svarer til ordenen af regulariseringsfunktionen anvendt, enten Gaussisk eller det ideele diskrete low-pass filter, hvilket påvises for test problemer. Homogene Dirichlet og Neumann betingelser opnås ved at medtage refleksioner af problemets egentlige ladning om domænets rande. Poisson løseren implementeres parallel algoritme og en god skalering demonstreres derved. Brug af løseren i en vortex metode vises og kombinationens konsistens demonstreres ved simulering af et semi-periodisk problem bestående af en ustabil konfiguration af to parallelle aflange hvirvler også studeret af Chatelain and Koumoutsakos (2010).

Vortex metoden udvides til at omfatte faste legemer i tredimensionelle strømninger ved brug af en Brinkman penaliseringsteknik af Hejlesen et al. (2015a).

En god opløsning af de faste legemers overflade er en nødvendighed for at kunne simulere strømninger med høj nøjagtighed, derfor bruges en multi-opløsningsformulering af metoden baseret på lokale forfiningsnet. Multi-opløsningsformuleringen anvendes for strømning om en circulær cylinder ved lavt Reynoldstal ($\mathrm{Re} = 300$) i tre dimensioner. Resultaterne, der opnås herved, er i god overenstemmelse med det der reporteres i litteraturen med hensyn til kraftkoefficienter, vækstrate- og topologien af den dominerende modalform i transitionen fra to- til tredimensionel strømning.

Large-eddy-simulation ved brug af to forskellige *subgrid-scale stress* modeller bliver herefter implementeret og verificeret for problemer bestående af homogen turbulens. Dernæst anvendes metoden for strømning om faste legemer ved moderat høje Reynoldstal ($\mathrm{Re} \geq 10^4$). En kvalitativ god overenstemmelse med eksperimentelle og numeriske resultater opnås herved, men der identificeres dog nogle udfordringer for metoden anvendt til løsning af sådanne problemer.

Abstract

This dissertation presents a vortex-particle mesh method for bluff body aerodynamics using iterative Brinkman penalization, local mesh refinement and large-eddy-simulation. The method relies on regularized Green's function solutions to the unbounded Poisson equation. The Poisson solver is based on the convolution approach by Hockney and Eastwood (1988) and is extended to a mixture of unbounded, periodic and homogeneous Dirichlet or Neumann conditions. A mixture of unbounded and periodic conditions is achieved using the technique of Chatelain and Koumoutsakos (2010), where the Poisson equation is initially Fourier transformed in the periodic directions. For each discrete wavenumber a modified Helmholtz equation of reduced dimensionality is then solved. The rate of convergence corresponds to the order of the regularization function used, either Gaussian or an ideal low-pass filter, which is demonstrated for test problems. Homogeneous Dirichlet or Neumann conditions are achieved using the method of images. The Poisson solver is implemented in parallel and demonstrated to be highly scalable. It is used within a remeshed vortex-method and the consistency of this combination is demonstrated for a semi-periodic problem of an unstable system of two parallel vortex pairs also considered by Chatelain and Koumoutsakos (2010).

The vortex method is extended to handle solid bodies using the iterative Brinkman penalization technique by Hejlesen et al. (2015a) for three dimensional flow. An accurate prediction of bluff body flow requires that the solid interface is well resolved, hence a multiresolution formulation of the method is applied based on refinement patches. The technique depends on a superposition of solutions to a scale-decomposed Poisson equation, which are obtained level wise in a mesh hierarchy. The multiresolution method is applied for the flow past a circular cylinder at low Reynolds number ($\mathrm{Re} = 300$) in three dimension.The obtained results are found to be in excellent agreement with what is reported in the literature, in terms of force coefficients, growth rate and the topology of spectral profile of the primary unstable mode of the transition from two- to three dimensional flow.

Large-eddy-simulations using two different subgrid-scale stress models are implemented and verified for benchmark cases of homogeneous turbulence. Subsequently, the models are applied for bluff body flow at moderate Reynolds number ($\mathrm{Re} \geq 10^4$). A qualitative good agreement is obtained with experimental and numerical results from the literature, but several challenges of the method applied for such applications are also identified.

Contents

Preface **i**

Resumé **iii**

Abstract **v**

Introduction **1**

1 A Fourier-based solver for the Poisson Equation **3**
1.1 Mixed free-space and periodic boundary conditions 7
1.2 Homogeneous Dirichlet and Neumann conditions 10
1.3 Parallel implementation of the Poisson solver 13
1.4 Summary 15

2 Vortex-particle mesh methods **19**
2.1 Approximation with particles and meshes 19
2.2 Constraints on the time-step size 23
2.3 Vorticity re-projection 23
2.4 Instability of counter rotating vortex pairs 24
2.5 Summary 25

3 Solid bodies **29**
3.1 The Brinkman penalization method 30
3.2 Numerical implementation of the Brinkman penalization method in a re-meshed vortex method 31
3.3 Calculation of the aerodynamic force and moment 34
3.4 Results 35
3.5 Summary 48

4 Multiresolution **53**
4.1 Multilevel decomposition 53
4.2 Mesh-to-mesh interpolation between levels 56
4.3 Convergence test of the multilevel Poisson solver in 1D 56
4.4 Multilevel particle-strength redistribution 59

4.5 Remarks on the implementation . . . 59
4.6 Verification of the combined procedure . . . 62
4.7 Multiresolution simulation of the flow past a circular cylinder at $\mathrm{Re} = 400$. 63
4.8 Summary . . . 67

5 Large eddy simulation **71**
5.1 Modeling . . . 71
5.2 Implementation in vortex-particle mesh method . . . 76
5.3 Verification . . . 77
5.4 Breakdown of counter rotating vortex pairs . . . 83
5.5 Flow past a square cylinder at $\mathrm{Re} = 2.2 \times 10^4$ . . . 83
5.6 Summary . . . 88

6 Application of the method for prediction of aerodynamic flutter **93**
6.1 Extraction of aerodynamic derivatives for a flat plate . . . 94
6.2 1-DOF flutter of H-shaped section . . . 98
6.3 Summary . . . 103

Conclusions **107**

Appendix **109**

A Regularized Green's functions in 1D **111**

B Discrete Transforms **113**
B.1 The Discrete Fourier Transform . . . 113
B.2 The Discrete Trigonometric Transforms . . . 115

C Efficiency of the parallel Poisson solver in 3D **121**

Bibliography **123**

Introduction

The ability to predict the motion of fluid flow and its interaction with solid structures is essential for engineering design. Examples include the design of tall buildings and long span suspension bridges. The aerodynamic loads on such structures may lead to failure, due to aerodynamic instability. Perhaps, the best known example is the first Tacoma Narrows Bridge in 1940, which collapsed after being set into large amplitude torsional oscillations by the oncoming wind as seen in Fig.1. A posterior investigations revealed that the H-shaped design of the free-span cross section was especially prone to vortex induced vibrations caused by unsteady separation of the boundary layers due to sharp corners at the leading edge.

Through experiments, engineers must carefully establish such error-prone designs to be able to guarantee the mechanical integrity before construction and operation. Computer simulation may be a cost efficient complement to physical experiments. However, computers can only handle a limited amount of data, hence they will neccesarily be based on a simplified reality. The main challenge of simulation is to resemble the physics sufficiently well to be able to draw the relevant conclusions from the simulated results.

During the many last decades continuing development of the simulation models has been undertaken and a wide range of different methods have been proposed. One branch of methods is vortex-particle methods. They rely on a Lagrangian approach due to the high spatial adaptivity, numerical stability and accuracy that may be achieved with those. If combined with a computational mesh the methods are sometimes referred to as the vortex-particle mesh (VPM) methods. The applications of VPM methods range from simulation of wind turbine wakes (Chatelain et al., 2013; Backaert et al., 2015; Branlard et al., 2015) to prediction of animal locomotion (Gazzola et al., 2011a; Gazolla et al., 2012). Further, simple methods based on two dimensional (2D) analysis has been applied as a complementary design tool for bridge aerodynamics (Walther and Larsen, 1997; Larsen and Walther, 1997, 1998; Rasmussen et al., 2010; Hejlesen et al., 2015c) The extension of such a tool to three dimensions (3D) is relevant as bluff body flow even at moderate Reynolds numbers exhibit a high degree of three-dimensionality and turbulent nature (Sohankar et al., 1999; Luo et al., 2003).

Unlike Eulerian methods, where the solid bodies are captured directly by enforcing no-slip boundary conditions on the solid interface with body fitted meshes, vortex methods have no natural way to do this accurately and efficiently. Another major challenge is to preserve a high numerical accuracy while minimizing computational efforts. These are still ongoing topics of research and the ones addressed in this dissertation.

Figure 1: Large amplitude torsional oscillations of the first Tacoma Narrows Bridge in 1940.

Chapter 1

A Fourier-based solver for the Poisson Equation

This chapter introduces a solver for the Poisson equation for problems of mixed boundary conditions. Parts of the chapter are based on the paper "A regularization method for solving the Poisson equation for mixed unbounded-periodic domains" published in Journal of Computational Physics 2018 (Spietz et al., 2018).

The solution to the scalar Poisson equation

$$\nabla^2 u(\boldsymbol{x}) = -f(\boldsymbol{x}) \tag{1.1}$$

is by application of Green's theorem the convolution in d dimensions

$$u(\boldsymbol{x}) = \int_{-\infty}^{\infty} G(\boldsymbol{x}-\boldsymbol{x}')f(\boldsymbol{x}')\,\mathrm{d}^d\boldsymbol{x}' \quad \Leftrightarrow \quad u(\boldsymbol{x}) = G(\boldsymbol{x}) * f(\boldsymbol{x}), \tag{1.2}$$

where the notation $\int \mathrm{d}^d\boldsymbol{x}$ should be interpreted as $\int\int\int \mathrm{d}x_1\mathrm{d}x_2\mathrm{d}x_3$ in the following, here exemplified for $d = 3$. $G(\boldsymbol{x})$ in Eq.(1.2) is the Green's function that satisfies the elementary equation

$$\boldsymbol{\nabla}^2_{\boldsymbol{x}} G(\boldsymbol{x},\boldsymbol{x}') = -\delta(\boldsymbol{x}-\boldsymbol{x}'). \tag{1.3}$$

By integration of Eq. (1.3) over a hyper-sphere of radius $r = |\boldsymbol{x}-\boldsymbol{x}'|$ centered at $\boldsymbol{x}'$

$$\int \nabla_{\boldsymbol{x}} \cdot \nabla_{\boldsymbol{x}} G(\boldsymbol{x},\boldsymbol{x}')\,\mathrm{d}V = \int -\delta(\boldsymbol{x}-\boldsymbol{x}')\,\mathrm{d}V \tag{1.4}$$

$$\tag{1.5}$$

and further by applying Gauss' theorem

$$\int \nabla_{\boldsymbol{x}} G(\boldsymbol{x},\boldsymbol{x}') \cdot \boldsymbol{n}\,\mathrm{d}S = -1, \tag{1.6}$$

it is easy to verify that the Green's function solutions are

$$G(\boldsymbol{x},\boldsymbol{x}') = \begin{cases} -\frac{1}{2}|x-x'| + c_1 & \text{in 1D} \\ -\frac{1}{2\pi}\ln\left(|\boldsymbol{x}-\boldsymbol{x}'|\right) + c_2 & \text{in 2D} \\ \frac{1}{4\pi|\boldsymbol{x}-\boldsymbol{x}'|} & \text{in 3D} \end{cases} \tag{1.7}$$

with c_1 and c_2 being arbitrary constants. The condition of the solution to be *unbounded* or *free-space* refers to the behavior $u(\boldsymbol{x}) \to 0$ for $|\boldsymbol{x}| \to \infty$. Only in 3D the Green's function goes

to zero at infinity, which implies that the solution obtained by Eq. (1.2) does the same if the right hand side is compact. In 2D however the derivative of the Green's function vanish at large distances, which is what is of primary interest in methods considered here.

The solution to Eq. (1.2) may be obtained either by applying a quadrature technique directly to determine the integral, with an appropriate treatment of the singularity, or by computing the convolution sum via Fourier-space

$$u(\boldsymbol{x}) = G(\boldsymbol{x}) * f(\boldsymbol{x}) \quad \Leftrightarrow \quad \widehat{u}(\boldsymbol{k}) = \widehat{G}(\boldsymbol{k})\widehat{f}(\boldsymbol{k}). \tag{1.8}$$

In Eq. (1.8) $\boldsymbol{k}$ is the wavenumber vector and $\widehat{u}(\boldsymbol{k})$ is the Fourier coefficients obtained with the Fourier transform for the space of dimensionality, d defined as

$$\widehat{u}(\boldsymbol{k}) = \int_{-\infty}^{\infty} u(\boldsymbol{x}) e^{-\iota \boldsymbol{k}\cdot\boldsymbol{x}} \,\mathrm{d}^d\boldsymbol{x}. \tag{1.9}$$

The solution is recovered from the Fourier coefficients by applying the inverse transform defined as

$$u(\boldsymbol{x}) = \left(\frac{1}{2\pi}\right)^d \int_{-\infty}^{\infty} \widehat{u}(\boldsymbol{k}) e^{\iota \boldsymbol{k}\cdot\boldsymbol{x}} \,\mathrm{d}^d\boldsymbol{k}. \tag{1.10}$$

The Fourier transform of Eq. (1.3) gives the Fourier coefficients of the Green's function directly as

$$-\boldsymbol{k}^2 \,\widehat{G}(\boldsymbol{k}) = -1 \qquad \Rightarrow \qquad \widehat{G}(\boldsymbol{k}) = \widehat{G}(k) = \frac{1}{k^2}, \tag{1.11}$$

where $k = |\boldsymbol{k}|$ is the magnitude wavenumber vector.

For numerical simulation a Fourier-space representation of the elementary function as Eq. (1.11) would be sufficient, but the singularity of Eq. (1.11) prevents the direct use of the spectral function in Fourier-space.

Hejlesen et. al (Hejlesen et al., 2013; Hejlesen, 2016; Hejlesen et al., 2017) and Vico et al. (2016) demonstrated that by requiring the Green's function to be bounded in either real- or Fourier-space the representation in the complementary-space becomes regular and smooth.

Vico et al. (2016) truncated the real-space functions Eq. (1.7) using a radial box filter to derive regular Fourier-space expressions for various linear operators. By truncating the Green's function at a radius larger than the maximum distance between any two sources in the problem, the solution procedure obtains the spectral accuracy imposed by the trapezoidal integration-rule used with the discrete Fourier transform (DFT). The Fast Fourier Transform (FFT) which is a fast DFT-algorithm is commonly used to compute unbounded convolution using the domain doubling technique by Hockney and Eastwood (1988). In this case the extended domain must cover twice the truncation radius ($2R$) to avoid error from the truncated convolution integral (Vico et al., 2016). In 3D for the unit domain the truncation radius may conservatively be chosen as $R = 2 > \sqrt{3}$ which impose a extended domain of $(4N)^3$, where N is the unit resolution along in all directions. The necessary length of the transforms may be reduced the original $(2N)^3$ after a precomputation step based on the $(4N)^3$ transform. However in the general case the truncation radius must be larger than the length of leading dimension of the

domain. Hence for domains with large aspect ratios, this requirement has been found to render the procedure impractical.

Alternatively, the procedure by Hejlesen et. al (Hejlesen et al., 2013; Hejlesen, 2016; Hejlesen et al., 2017) relies on deriving regular Green's functions in real-space by convolution of the singular solutions with a filter, whose spectral transfer function $\zeta(k)$ approximates the ideal low-pass filter and removes content above the Nyquist wavenumber ($k = \pi/h$)

$$\widehat{\zeta}(k) = \begin{cases} 1 & k = 0 \\ 0 & k = \frac{\pi}{h}. \end{cases} \tag{1.12}$$

The ideal regularization function may be derived from the multidimensional Fourier transform of a radial function expressed by the Hanckel transform in d dimensions

$$\widehat{\zeta}(k) = (2\pi)^{\frac{d}{2}} k^{-\frac{d-2}{2}} \int_0^\infty r^{\frac{d}{2}} f(r) J_{\frac{d-2}{2}}(kr)\,\mathrm{d}r. \tag{1.13}$$

By introducing the normalized radius, $\rho = r\ \sigma$ and corresponding wavenumber $s = \sigma k$

$$\widehat{\zeta}(s) = s^{-\frac{d-2}{2}} \int_0^\infty (2\pi)^{\frac{d}{2}} \sigma^d \rho^{\frac{d}{2}} \zeta(\rho) J_{\frac{d-2}{2}}(s\rho)\,\mathrm{d}\rho, \tag{1.14}$$

a property of the integral of a Bessel function product

$$s^{\frac{-d-2}{2}} \int_0^\infty J_{d/2}(\rho) J(s\rho)\,\mathrm{d}\rho = \begin{cases} 1 & s < 0 \\ \frac{1}{2} & s = 1 \\ 0 & s > 1 \end{cases} \tag{1.15}$$

may be used to obtain filters which frequency response has bandwidth $1/\sigma$. Choosing the normalization $\sigma = h/\pi$ the cut-off falls at the Nyquist wavenumber. The ideal filters for $d \leq 3$ are

$$\zeta(\rho) = \frac{J_{d/2}(\rho)}{(2\pi)^{\frac{d}{2}} \sigma \rho^{\frac{d}{2}}} = \begin{cases} \frac{\sin(\rho)}{\pi\rho\sigma} & d = 1 \\ \frac{\mathrm{J}_1(\rho)}{2\pi\sigma^2\rho} & d = 2 \\ \frac{\sin(\rho) - \cos(\rho)\rho}{2\pi^2\sigma^3\rho^3} & d = 3. \end{cases} \tag{1.16}$$

By radial integration of Eq. (1.3) convolved with the filters

$$\nabla^2 G(r) = -\zeta(r) \tag{1.17}$$

the associated Green's functions become

$$G(r) = \begin{cases} -\frac{\sigma}{\pi}(\mathrm{Si}(\rho)\rho + \cos(\rho)) + c_1 & d = 1 \\ \frac{1}{2\pi}\mathrm{Ji}_0(\rho) + c_2 & d = 2 \\ \frac{\mathrm{Si}(\rho)}{2\pi^2\sigma\rho} & d = 3. \end{cases} \tag{1.18}$$

The constants c_1 and c_2 are arbitrary because a condition has only be imposed on the derivatives of the Green's function for $d \leq 2$. The function, $\mathrm{Si}(\rho)$ which occurs in the expressions is the sine-integral function

$$\mathrm{Si}(\rho) = \int_0^\rho \frac{\sin(t)}{t}\,\mathrm{d}t, \tag{1.19}$$

which may be approximated to arbitrary accuracy using a fast evaluation technique based on polynomial expansion. The Bessel-integral of zeroth order

$$\mathrm{Ji}_0(\rho) = \int_0^\rho \frac{\mathrm{J}_0(t) - 1}{t}\,\mathrm{d}t, \tag{1.20}$$

may be evaluated by a similar approximation technique based on a rapidly converging expansion in Chebyshev polynomials (Luke, 1962, Tab. 9.3).

An alternative method for truncating the spectral function is based on high order Gaussian filters, which are constructed by approximate deconvolution (Hejlesen et al., 2013). By multiplying the Gaussian function with the $m/2$ first terms of the Taylor expansion of its inverse (D_m)

$$\widehat{\zeta}_m(k) = e^{\frac{-k^2}{2}} D_m(k) \quad \text{where} \quad D_m(k) = \sum_0^{m/2-1} \frac{1}{n!}\left(\frac{k^2}{2}\right)^n, \tag{1.21}$$

the m-first derivatives are nullified at $k = 0$

$$\left.\frac{d^\beta \widehat{\zeta}_m}{dk^\beta}\right|_{k=0} = \int_{-\infty}^{\infty} r^\beta\, \zeta_m(r)\,\mathrm{d}^d\boldsymbol{x} = 0^\beta \quad \text{for} \quad \beta = 0, 2, ..., m-2. \tag{1.22}$$

This corresponds to conserving moments of the corresponding real-space function. Note that m is an even number and that the moments for odd integers of β are automatically satisfied due to the radial symmetry of the function. The filter does not satisfy $\widehat{\zeta}(\pi/h) = 0$ due to the infinite support of the Gaussian function. So, again a normalization of the coordinates as $\rho = r/\sigma$ and the wavenumber $s = k\sigma$ through a smoothing radius ($\sigma = \alpha h$) is introduced, here to ensure that the filter is well resolved when sampled

$$\widehat{\zeta}_m(s) = \widehat{D}_m(s)\, e^{-\frac{s^2}{2}} \qquad \text{where} \qquad \widehat{D}_m(s) = \sum_{n=0}^{m/2-1} \frac{1}{n!}\left(\frac{s^2}{2}\right)^n. \tag{1.23}$$

At the maximum resolved wavenumber $k_{\max} = k_s/2 = \pi/h$ the truncation of the regularization function is $\widehat{\zeta}(\pi\alpha)$. Hence the choice of normalization ensures that the truncation is independent of the mesh resolution. The regularised kernels by radial integration of Eq. (1.17) are given in (Hejlesen et al., 2013; Hejlesen, 2016) for 2D and 3D and in Appendix A for 1D.

Spectral transfer functions of various filters have been plotted in Fig. 1.1 and the corresponding Green's functions in Fig. 1.2 for comparison.

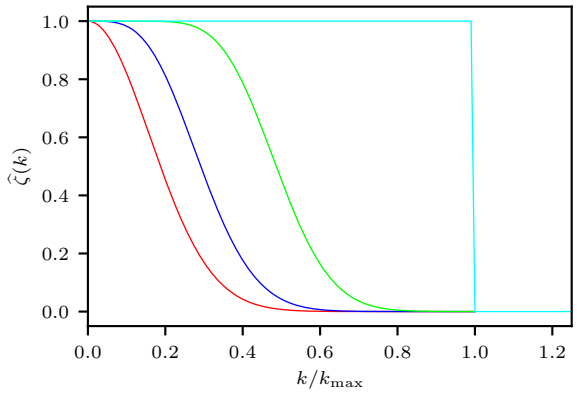

Figure 1.1: Spectral transfer function of filters used to derive regular Green's function solution for free-space problems: Gaussian function for $m = 2$ and $\alpha = 2$ (—) Gaussian function for $m = 4$ and $\alpha = 2$ (—) Gaussian function for $m = 10$ and $\alpha = 2$ (—) and ideal regularization function (—) .

1.1 Mixed free-space and periodic boundary conditions

To obtain a Green's function representation in the case of a mixture of free-space and periodic boundary condition the procedure by Chatelain and Koumoutsakos (2010) is applied that consists of initially Fourier transforming the Poisson equation (Eq. (2.4)) in the periodic directions. Subsequently, a modified Helmholtz equation of reduced dimensionality is solved for each wavenumber before applying the inverse transform.

E.g. in 2D with one periodic (the y-direction) and one free-space (the x-direction) boundary condition, the partly transformed regularized elementary equation is

$$\boldsymbol{\nabla}_x^2 \widehat{G}(x, k_y) - k_y^2 \widehat{G}(x, k_y) = -\zeta(x)\widehat{\zeta}(k_y), \tag{1.24}$$

The solution to Eq. (1.24) using normalized coordinates, is

$$\widehat{G}(\rho_x, s_y) = \frac{\sigma}{2\pi} \int_{-\infty}^{\infty} \frac{\widehat{\zeta}\left(\sqrt{s_x^2 + s_y^2}\right)}{s_x^2 + s_y^2} e^{\iota\, s_x\, \rho_x}\, \mathrm{d}s_x, \tag{1.25}$$

where $s_x = \sigma\, k_x$, $s_y = \sigma\, k_y$, and $\rho_x = |x|/\sigma$. A closed form expression for Eq. (1.25) has been derived in Hejlesen (2016); Spietz et al. (2018). A discrete spectral representation is sufficient to compute the discrete convolution. Rather than solving the integral Eq. (1.25), it is noted that the singularity lies on the line $s_y = 0$. For $s_y = 0$ the problem Eq. (1.24) reduces to a 1D Poisson equation which regularized solution has already been derived.

The Fourier transform of the Green's function for the combination of a free-space condition (x-direction) and a periodic condition (y-direction) may be written semi-explicitly as

$$\widehat{G}(s_x, s_y) = \begin{cases} \widehat{G}^{\mathrm{1D}}(s_x) & \text{for } s_y = 0 \\ \frac{\widehat{\zeta}(s)}{s^2} & \text{otherwise.} \end{cases} \qquad \text{where } s^2 = s_x^2 + s_y^2 \tag{1.26}$$

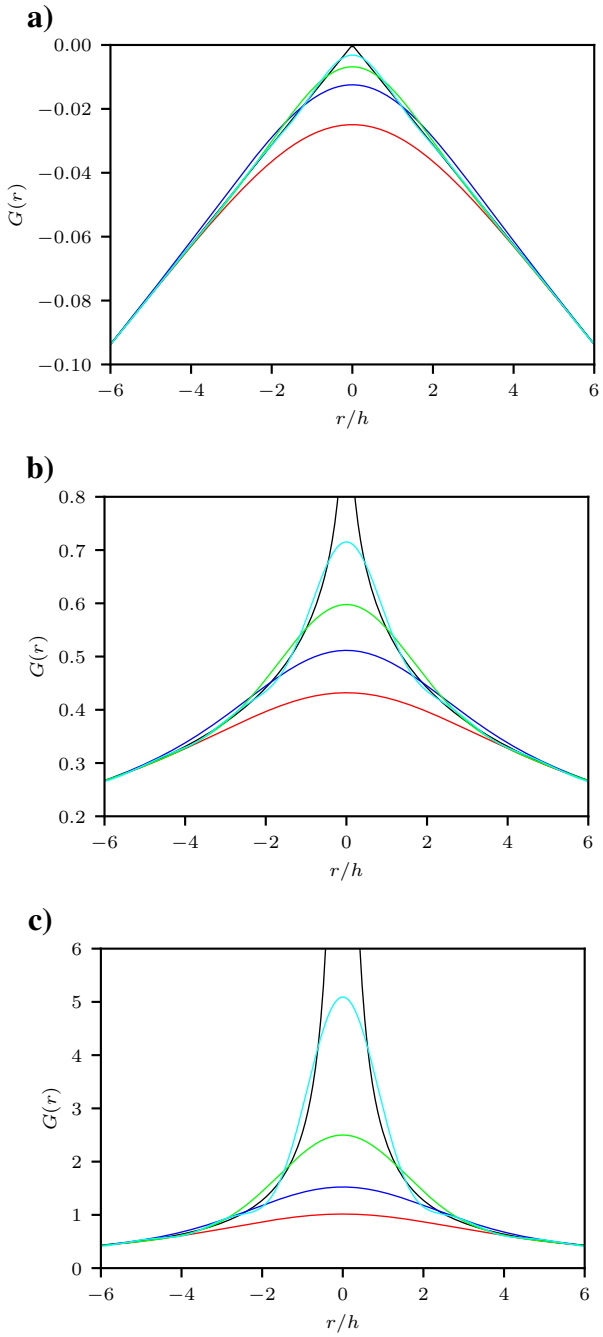

Figure 1.2: Free-space Green's functions for the Laplace operator in 1D (a), in 2D (b) and in 3D (c): Singular (—) , Gaussian regularization for $\alpha = 2$ and $m = 2$ (—) , $m = 4$ (—) , $m = 10$ (—) and ideal regularization (—) .

The discrete convolution kernel in Fourier-space is obtained by taking the DFT of $G^{\text{1D}}(\rho_x)$ from either Eq. (1.18) or Eq. (A.2) on the strip $s_y = 0$ and by direct evaluation of the non-singular spectral expression for $s_y \neq 0$.

Similarly in 3D the Green's function in fourier-space for a single free-space condition (x-direction) and two periodic conditions (x, y-directions) is obtained by taking the DFT of the regularised 1D Green's function on the strip $s_y = s_z = 0$

$$\widehat{G}(s_x, s_y, s_z) = \begin{cases} \widehat{G}^{\text{1D}}(s_x) & \text{for } s_y = s_z = 0 \\ \frac{\widehat{\zeta}(s)}{s^2} & \text{otherwise.} \end{cases} \qquad \text{where } s^2 = s_x^2 + s_y^2 + s_z^2 \tag{1.27}$$

For a two free-space conditions (x, y-directions) and a single periodic condition (z-direction) we use the regularised 2D Green's function from Eq. (1.18) or (Hejlesen et al., 2015b) on the slice $s_z = 0$

$$\widehat{G}(s_x, s_y, s_z) = \begin{cases} \widehat{G}^{\text{2D}}(\sqrt{s_x + s_y}) & \text{for } s_z = 0 \\ \frac{\widehat{\zeta}(s)}{s^2} & \text{otherwise.} \end{cases} \qquad \text{where } s^2 = s_x^2 + s_y^2 + s_z^2 \tag{1.28}$$

1.1.1 Verification of the consistency of the Poisson solver for mixed free-space and periodic boundary conditions

We verify the consistency of the proposed FFT-based solver with mixed unbounded and periodic conditions using a test function that is bounded within the computational domain in the unbounded directions and fully continuously differentiable in the periodic directions.

For simplicity we consider only the scalar poisson equation here. The unbounded scalar Poisson kernels in 1D and in 2D provide solutions that are arbitrary up to a constant. Hence we require the integral of the test function (u_{test}) in the unbounded directions to be zero so that the dependency of the constant is removed. This could also have been achieved by comparing derivatives of the solution only.

To meet these requirements we use sine functions for the periodic directions and a normalized bump function distribution in the unbounded directions, which both are of class C^∞ i.e. it has an infinite number of continuous derivatives. The bump function is defined as

$$b(q) = \begin{cases} \exp\left(c\left[1 - \frac{1}{1-q^2}\right]\right) & \text{for} \quad |q| < 1 \\ 0 & \text{for} \quad |q| \geq 1, \end{cases} \tag{1.29}$$

where c is an arbitrary positive constant. For the presented cases $c = 400$ is used. Further we ensure that test function is non-zero when averaged in the periodic direction to verify a consistent treatment of the singularity.

For the 2D case with one unbounded (x) and one periodic (y) direction, we solve the scalar equation of Eq. (1.1) using the test function solution

$$u_{\text{test}}(x, y) = b\,(x)\ [1 + \ \sin\,(2\pi\, y)]\,. \tag{1.30}$$

Similarly, for the 3D case with one unbounded (x) and two periodic (y and z) directions, we use the test function solution

$$u_{\text{test}}(x, y, z) = b\,(x)\ [1 + \ \sin\,(2\pi\, y)\ \ \sin\,(2\pi\, z)]\,. \tag{1.31}$$

For the 3D case with two unbounded (x and y) and one periodic (z) directions

$$u_{\text{test}}(x, y, z) = b\left(\sqrt{x^2 + y^2}\right)\ [1 + \ \sin\,(2\pi\, z)]\,. \tag{1.32}$$

When solving

$$\nabla^2 u = -f, \quad \text{where } f = -\nabla^2 u_{\text{test}} \tag{1.33}$$

we measure the error as the second norm of the deviation on the mesh points

$$\text{error} = \left(\sum_{i=1}^{N} \left(u(\boldsymbol{x}_i) - u_{\text{test}}(\boldsymbol{x}_i)\right)^2 / \sum_{i=1}^{N} u_{\text{test}}(\boldsymbol{x}_i)^2\right)^{1/2} \tag{1.34}$$

The error for the various cases is shown in Fig. 1.3 where it is compared to the non-regularized method of Chatelain and Koumoutsakos (2010). It is seen that the method obtains the convergence rate corresponding to the respective design parameters of the Green's functions. The regularized method is shown to quickly produce an error which is significantly lower than that of Chatelain and Koumoutsakos (2010) for $m > 2$. Using the ideal regularization function the error decays exponentially until it flattens out near the level arithmetic precision.

1.2 Homogeneous Dirichlet and Neumann conditions

Homogeneous Dirichlet and Neumann conditions may also be imposed. This is achieved using the method of images. The method of images is a domain extension technique convenient for simple symmetric domains such as cuboids, where image charges are added outside the original domain to satisfy the conditions on the original boundaries. By the uniqueness theorem an extended solution that complies with the boundary conditions is also the correct solution within the original domain.

E.g. the elementary solution to the half-unbounded 2D problem

$$\boldsymbol{\nabla}^2 G_D(\boldsymbol{x}, \boldsymbol{x}') = -\boldsymbol{\delta}(\boldsymbol{x} - \boldsymbol{x}'), \quad x \geq 0, -\infty < y < \infty \tag{1.35}$$

$$G_D(\boldsymbol{x}, \boldsymbol{x}') = 0, \qquad x = 0 \tag{1.36}$$

may be obtained solving the extended problem with the unit source at $\boldsymbol{x} = (x, y)$ oddly reflected in $(x = 0, y)$ corresponding to the location $\tilde{\boldsymbol{x}} = (-x, y)$

$$\boldsymbol{\nabla}^2 G_D(\boldsymbol{x}, \boldsymbol{x}') = -\boldsymbol{\delta}(\boldsymbol{x} - \boldsymbol{x}') + \boldsymbol{\delta}(\boldsymbol{x} - \tilde{\boldsymbol{x}}'), \quad -\infty < x, y < \infty. \tag{1.37}$$

The solution for this problem is the superposition of the free-space Green's functions. Clearly the boundary condition is satisfied for a radially symmetric Green's function ($G(\boldsymbol{x}, \boldsymbol{x}') = G(|\boldsymbol{x} - \boldsymbol{x}'|)$)

$$G_D(\boldsymbol{x}, \boldsymbol{x}')|_{x=0} = G(|\boldsymbol{x} - \boldsymbol{x}'|) - G(|\boldsymbol{x} - \tilde{\boldsymbol{x}}'|) = 0 \tag{1.38}$$

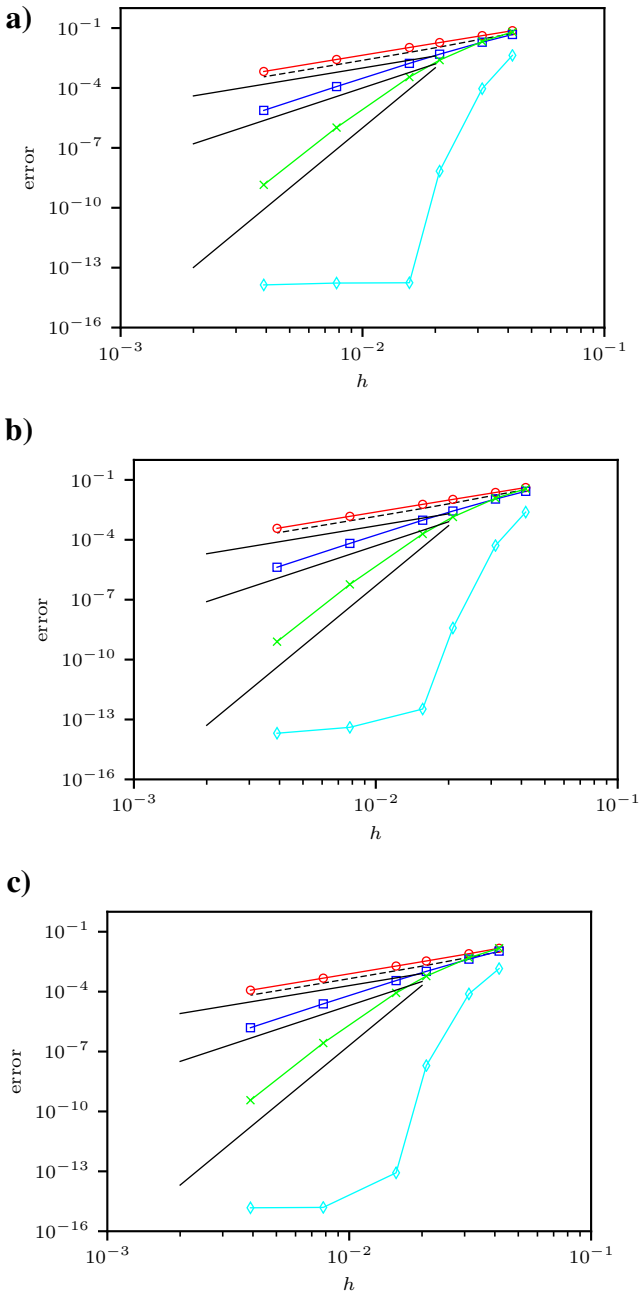

Figure 1.3: Error obtained when solving mixed free-space and periodic Poisson equation for periodic-free 2D problem (a), periodic-periodic-free 3D problem (b) and periodic-free-free 3D problem (c). Lines indicate the solution obtained using a non-regularized Green's function (Chatelain and Koumoutsakos, 2010) (- - -) and using a regularized Green's function with Gaussian regularization for $m = 2$ and $\alpha = 0.75$ (—○—) , Gaussian regularization for $m = 4$ and $\alpha = 1.5$ (—□—) , Gaussian regularization for $m = 10$ and $\alpha = 2.0$ (—×—) and ideal regularization (—◇—) . Orders of convergence of convergence from top to bottom $\mathcal{O}(h^2)$, $\mathcal{O}(h^4)$, $\mathcal{O}(h^{10})$ (——) .

as $|\boldsymbol{x} - \boldsymbol{x}'| = |\boldsymbol{x} - \tilde{\boldsymbol{x}}'|$ at $x = 0$.

Similarly the half-unbounded problem with a Neumann condition

$$\boldsymbol{\nabla}^2 G_N(\boldsymbol{x}, \boldsymbol{x}') = -\boldsymbol{\delta}(\boldsymbol{x} - \boldsymbol{x}'), \quad x \geq 0, -\infty < y < \infty \tag{1.39}$$

$$\frac{\mathrm{d}G_N(\boldsymbol{x}, \boldsymbol{x}')}{\mathrm{d}x} = 0, \qquad x = 0 \tag{1.40}$$

is equivalent to

$$\boldsymbol{\nabla}^2 G_N(\boldsymbol{x}, \boldsymbol{x}') = -\boldsymbol{\delta}(\boldsymbol{x} - \boldsymbol{x}') - \boldsymbol{\delta}(\boldsymbol{x} - \tilde{\boldsymbol{x}}'), \quad -\infty < x, y < \infty. \tag{1.41}$$

By differentiation it is confirmed that the boundary condition is satisfied at $x = 0$ for a radially symmetric Green's function

$$\frac{\mathrm{d}G_N(\boldsymbol{x}, \boldsymbol{x}')}{dx} = (x - x') \left[\frac{1}{r}\frac{\mathrm{d}G}{\mathrm{d}r}\right]_{r=|\boldsymbol{x}-\boldsymbol{x}'|} + (x + x') \left[\frac{1}{r}\frac{\mathrm{d}G}{\mathrm{d}r}\right]_{r=|\boldsymbol{x}-\tilde{\boldsymbol{x}}'|}. \tag{1.42}$$

To achieve a doubly bounded interval $0 \leq x \leq L$, e.g. with any combination of homogenous conditions using the method of images an infinite array of images must be considered as illustrated in Fig. 1.4: To impose a condition at $x = 0$ a single image reflection is added as in Eq. (1.37) or Eq. (1.41), then in order impose the boundary condition at $x = L$, image reflections of not only the primary charge but also its image reflection about $x = 0$ must be added. The influence of the newly added images must then be corrected at $x = 0$ and so on.

It is straight forward to impose a single Neumann or Dirichlet boundary condition by constructing the correct Green's function by image summation and to use this with the zero-padding technique. To impose a doubly bounded direction this is not practical as the construction of the Green's function impose a sum of infinite terms. Rather than constructing the Green's function for the extended problem the extended problem may be solved directly and subsequently the solution, which is not within the region of interest, may be discarded. This is done by noting that the convolution to compute is symmetric-periodic. A survey of various symmetric convolutions and how to compute them using discrete trigonometric transforms (DTTs) was given by Martucci (1994). Further, by the use of a DTT the domain-doubling requirement in that direction is eliminated and the discrete transform coefficients are real valued. For a doubly bounded direction of pure Dirichlet or Neumann conditions the extended problem has a $2N$ periodicity in the bounded directions, hence the convolution kernel to be used must be for the $2N$-periodic problem. Likewise for doubly bounded problems of a mixture of Dirichlet and Neumann type conditions the extended problem has a $4N$ periodicity in the bounded directions, hence the convolution kernel to be used must be for the $4N$-periodic problem in this case. The relevant DTTs and their relation to the DFT has been outlined in App. B.2.

1.2.1 1D examples

The capability of imposing boundary conditions using the method of images is tested in 1D using a normalized Gaussian right-hand-side

$$f(x) = \frac{1}{\sigma\sqrt{2\pi}} \exp\left(-\frac{x^2}{2\sigma^2}\right). \tag{1.43}$$

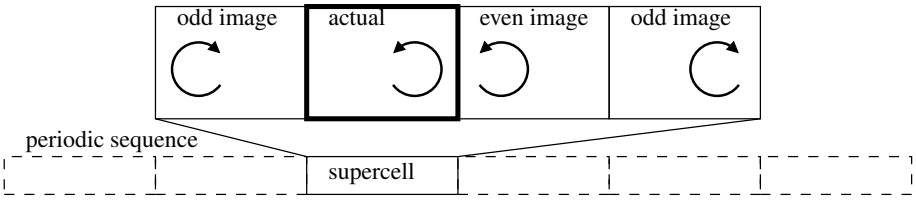

Figure 1.4: A doubly bounded direction with a mixture of Dirichlet (to the left) and Neumann (to the right) conditions is obtained by including an infinite array of even and odd images of the actual vorticity.

Fig. 1.5 compares the solution for various boundary conditions imposed on the problem. A bounded solution may either be obtained by explicitly extending the computational domain to account for the required images. Alternatively, a symmetric-convolution may be applied for which any derivative of the solution may be approximated by spectral differentiation. Finally, for single bounded directions explicit summation of Green's functions may be applied with zero-padding technique for the active domain only. By using the last technique the derivatives are not obtainable by spectral differentiation as seen in Fig. 1.5(b) and Fig. 1.5(c). The derivatives obtained hereby show a oscillatory behavior near the boundaries. Derivatives may be obtained by analytic differentiation of the Green's function sum. Alternatively, the derivatives may be approximated by finite-difference approximation.

It should be noted that the 1D procedure is valid also for multidimensional problems, by applying it in the bounded directions and the usual domain-doubling procedure in the unbounded directions.

1.3 Parallel implementation of the Poisson solver

Computations of convolution sums using DFTs are here carried out using efficient FFT algorithms from the Intel MKL library (Wang, 2014) or the FFTW library (Frigo and Johnson, 2005). The 3D DFT is separable, and is computed by sequentially applying the 1D DFT along the three axis directions.

For parallel computation a pencil-block decomposition of the global mesh-array is employed as illustrated in Fig. 1.6 for a 9 processor example: For each of the three transform directions the global mesh-array is decomposed into blocks of 1D strips aligned with the transform direction, such that the 1D FFT/IFFT may be computed locally on each processor. Subsequently a global mapping operation is required to align the data with the pencil-decomposition of the next transform direction and so on. This approach supports a parallel decomposition using as many processors as entries in any 2D slice of the global mesh array, but implies two array transpositions more than a decomposition based on blocks of 2D slices.

The domain doubling technique by Hockney and Eastwood (1988) increase computational cost from $\mathcal{O}(N^d \log\left(N^d\right))$ to $\mathcal{O}((2N)^d \log\left((2N)^d\right))$. The increased cost due to domain doubling may be reduced by discarding redundant regions of the transforms. This is done by only partly extending the pencil-block mesh layouts as needed. The cost may be reduced even further taking into account the symmetries of the DFT. E.g. solving a Poisson equation for real num-

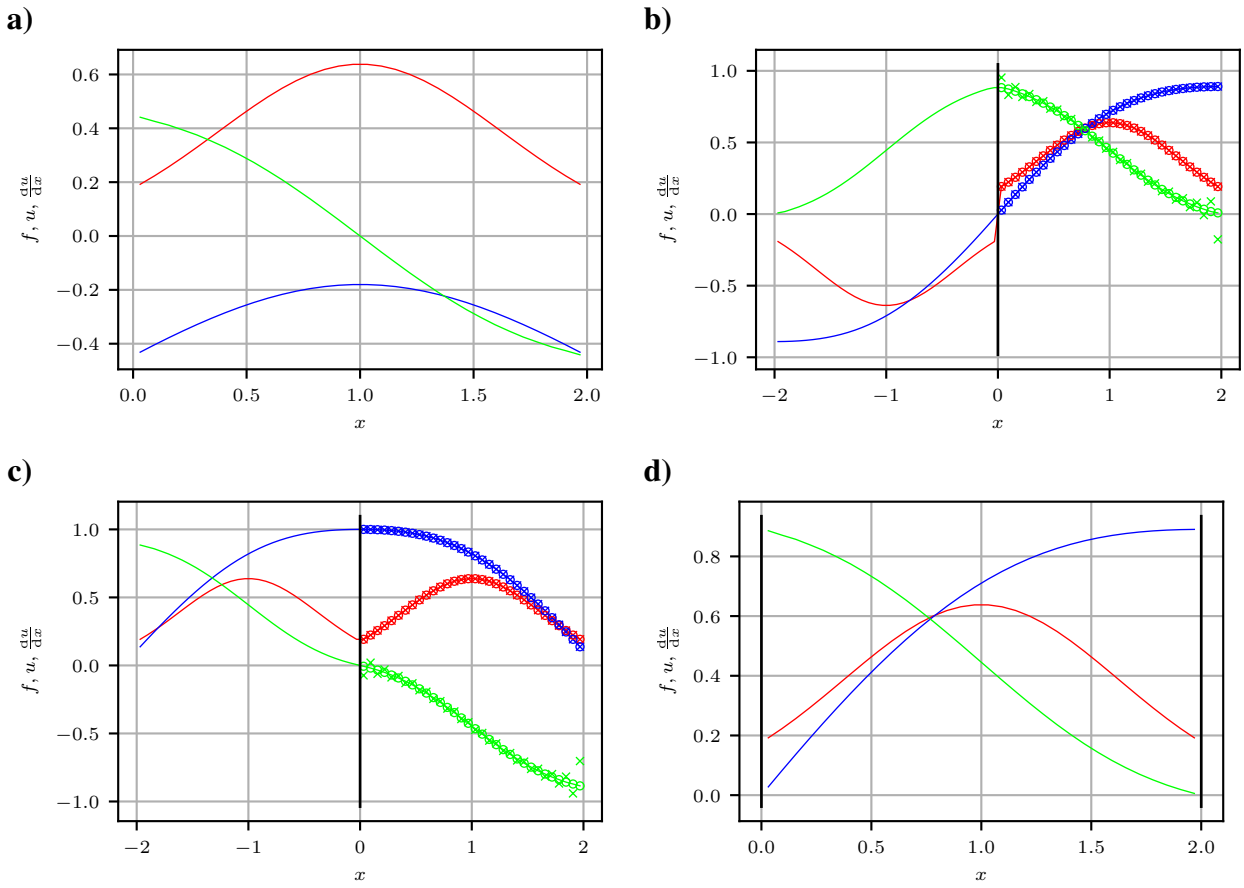

Figure 1.5: The solutions ($u(x)$) (—) to the 1D poisson equation for right-hand-side (f) (—) and various boundary conditions. Also indicated the derivative ($\frac{du}{dx}$) obtained by spectral differentiation (—) : (a) Unbounded solution. (b) Half-unbounded solution with a Dirichlet condition imposed at $x = 0$ by solving the extended problem with free-space conditions (—) , by solving the extended problem using zero-padded symmetric convolution via DCT2/DST2 (○) and by solving the extended problem using explicit summation of free-space Green's functions (×) . (c) Half-unbounded solution with a Neumann condition imposed at $x = 0$ by solving the extended problem with free-space conditions (—) , by solving the extended problem using zero-padded symmetric convolution via DCT2/DST2 (○) and by solving the extended problem using explicit summation of free-space Green's functions (×) . (d) Doubly-bounded solution with a Dirichlet and Neumann condition imposed at respectively $x = 0$ and $x = 2$ obtained using symmetric convolution via DCT4/DST4.

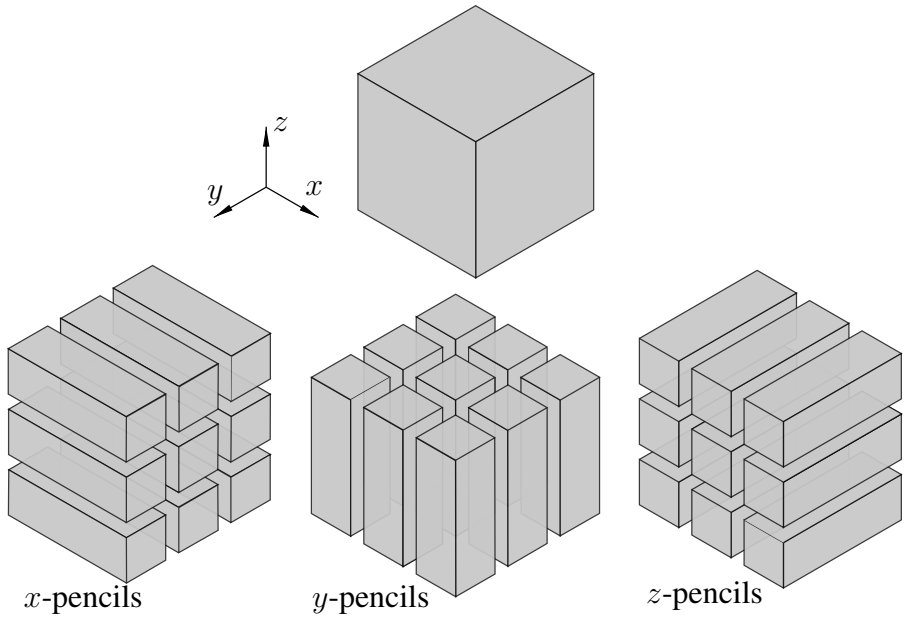

Figure 1.6: Decomposition of the global mesh array into pencils for parallel computation of a 3D FFT. Illustrated for 9 processes.

bers implies a real-to-complex transform in the first transform direction. The discrete Fourier coefficients of a real function are Hermitian symmetric ($\widehat{x}_{-k} = \widehat{x}_k^*$, where $(\cdot)^*$ denotes the complex conjugate) hence coefficients $\widehat{x}_{i,j,k}$, $i = -N/2, ..., -1$ may be discarded on the second and third transform directions (reducing computational efforts and storage by a factor 2). The discarded coefficients can be restored on the inverse transform. This is implicitly done with a real-to-complex (r2c) and complex-to-real (c2r) transform pair from the Intel MKL or FFTW library.

The use of DTTs does not impose additional computational costs as compared to the use of DFTs. On the contrary the discrete trigonometric transforms (DTT) work purely with real numbers (r2r transforms), hence the coefficient takes up half the storage and if the DTT is applied for the first transform direction, Hermitian symmetry may be utilized on the second transform direction. For the N-point DTTs considered fast algorithms based on the FFT are used, which are at most twice as expensive as the N-point FFT (Frigo and Johnson, 2005).

The procedure of the convolution using partly extended mesh-arrays and Hermitian symmetry has been illustrated in Fig. 1.7.

The implementation is tested in terms of parallel efficiency in App. C and found to show a good parallel speedup.

1.4 Summary

In this chapter regularised Green's functions based on either Gaussian filters or the ideal low-pass filter were introduced. The derivations were based on those by Hejlesen et al. (2013); Hejlesen (2016). The solution for unbounded problems was extended to a mixture of unbounded, periodic and homogeneous Dirichlet or Neumann conditions. The Dirichlet and Neu-

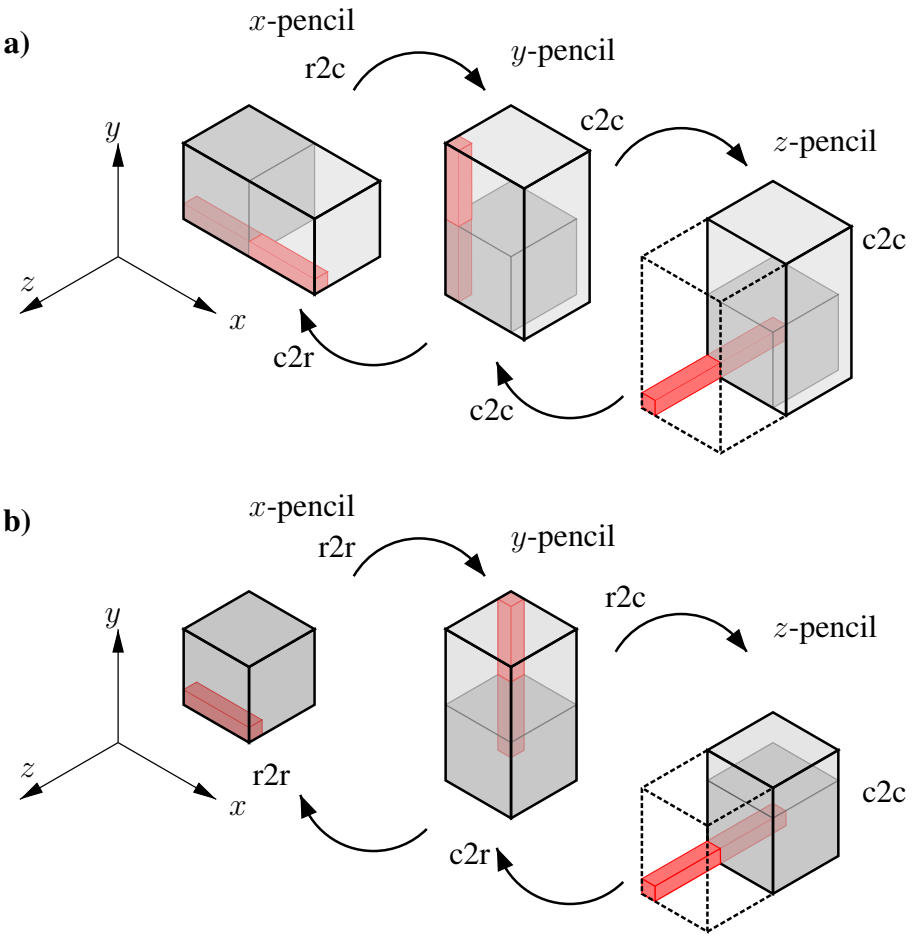

Figure 1.7: Layouts of the partly-extended mesh array used for solving the Poisson equation discarding redundant regions and utilizing the Hermitian symmetry of real-to-complex transform. The red regions illustrate a representative mesh-block held by a single process, which is transformed using a 1D FFT algorithm. The dark-gray regions indicate the original computational domain. The light-gray region indicates non-zero input/output to/from the FFT that must be stored in memory and transferred to the next layout for the following transform. The combined light-gray and dashed region indicate the extent of the Green's function Fourier coefficients: (a) An unbounded problem: zero-padding is applied in all directions. A real-to-complex transform is used in the first direction (x) and Hermitian symmetry of the discrete Fourier coefficients is assumed for the subsequent transforms. (b) A mixed doubly-bounded (x) and unbounded (y, z) problem: A real-to-real transform is used in this direction, hence the real-to-complex transform is applied in the second direction.

mann conditions are well suited for fluid flow simulations, when it is necessary to impose e.g. a through-flow or a no-through condition in one or more directions. It should be noted that a no-through condition based on the homogenous boundary conditions may further be extended to a no-slip condition in vortex-particle mesh methods using a vortex-panel diffusion approach as in Koumoutsakos et al. (1994); Ploumhans and Winckelmans (2000); Ploumhans et al. (2002).

Chapter 2

Vortex-particle mesh methods

This chapter introduces the vortex-particle mesh method for fluid flow simulation. The implementation is based on the Fourier-based Poisson solver from the previous chapter. Some of the results presented were published in Spietz et al. (2018).

Incompressible fluid flow may be described mathematically by the Navier-Stokes equations in their velocity-pressure form

$$\frac{D\boldsymbol{u}}{Dt} = \frac{\partial \boldsymbol{u}}{\partial t} + (\boldsymbol{u}\cdot\boldsymbol{\nabla})\boldsymbol{u} = -\frac{\boldsymbol{\nabla} p}{\rho} + \nu\boldsymbol{\nabla}^2\boldsymbol{u}, \quad \boldsymbol{\nabla}\cdot\boldsymbol{u} = 0. \tag{2.1}$$

In the analysis of many flows it is natural to formulate the problem in terms of vorticity ($\boldsymbol{\omega} = \boldsymbol{\nabla}\times\boldsymbol{u}$). By looking at the vorticity the coherent structures of the flow may be identified directly. Further more, in bluff body flows the evolution of vorticity is directly related to the variation of the fluid force.

Vortex methods discretize the vorticity rather than fluid momentum and are based on the Navier-Stokes equations (Eq. (2.1)) recast into the vorticity transport equation

$$\frac{D\boldsymbol{\omega}}{Dt} = \frac{\partial \boldsymbol{\omega}}{\partial t} + (\boldsymbol{u}\cdot\boldsymbol{\nabla})\boldsymbol{\omega} = (\boldsymbol{\omega}\cdot\boldsymbol{\nabla})\boldsymbol{u} + \nu\boldsymbol{\nabla}^2\boldsymbol{\omega}. \tag{2.2}$$

A relation between the velocity and vorticity is derived by decomposing the velocity into potential functions as

$$\boldsymbol{u} = \boldsymbol{\nabla}\times\boldsymbol{\Psi} - \nabla\phi, \quad \nabla\cdot\boldsymbol{\Psi} = 0. \tag{2.3}$$

By further taking the curl of Eq. (2.3) a Poisson equation for the vector potential is obtained

$$\boldsymbol{\nabla}^2\boldsymbol{\Psi} = -\boldsymbol{\omega}, \quad \boldsymbol{u}_{\boldsymbol{\omega}} = \boldsymbol{\nabla}\times\boldsymbol{\Psi}. \tag{2.4}$$

2.1 Approximation with particles and meshes

In vortex-particle methods the vorticity in d-dimensions

$$\boldsymbol{\omega}(\boldsymbol{x},t) = \int \boldsymbol{\omega}(\boldsymbol{x}',t)\delta(\boldsymbol{x}-\boldsymbol{x}')\,\mathrm{d}^d\boldsymbol{x}' \tag{2.5}$$

is approximated using discrete particles

$$\boldsymbol{\omega}(\boldsymbol{x},t) \approx \sum_p \boldsymbol{\omega}_p(t) v_p \zeta(\boldsymbol{x}-\boldsymbol{x}_p), \tag{2.6}$$

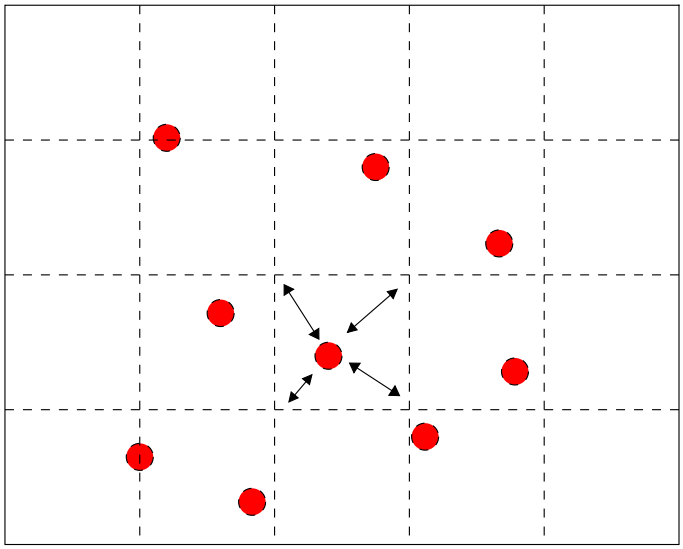

Figure 2.1: Interpolation between particles (red markers) and a uniform in mesh (dashed lines) is used with the vortex-particle mesh method to aid the particle approximation.

where $\zeta(\boldsymbol{x})$ is a smooth approximation to the Delta function ($\delta(\boldsymbol{x})$) and v_p is the volume represented by a particle p. The quantity $\omega_p v_p$ is denoted the particle-strength, which corresponds to the circulation represented by a particle in 2D with units m^2/s. In 3D the particle-strength is a vector quantity of units m^3/s. By inserting Eq. (2.6) into Eq. (2.2) a system of coupled differential equations is obtained, which is solved in a Lagrangian frame of reference using explicit time-step schemes

$$\frac{d\boldsymbol{x}_p}{dt} = \boldsymbol{u}(\boldsymbol{x}_p), \tag{2.7}$$

$$\frac{d\boldsymbol{\omega}_p}{dt} = \left[(\boldsymbol{\omega}\cdot\boldsymbol{\nabla})\boldsymbol{u} + \nu\boldsymbol{\nabla}^2\boldsymbol{\omega}\right]_p. \tag{2.8}$$

Redistribution of particle-strength onto a structured set of points – a mesh (*re-meshing*) is necessary to preserve the consistency of the method (Koumoutsakos and Leonard, 1995; Koumoutsakos, 1997). By using a mesh of spacing h, this impose that the particle volume corresponds to the cell volume, e.g. $v_p = h^3$ in 3D. Further, by distribution of the vortex-particle strength onto a mesh, the right-hand-side of Eqs. (2.7)–(2.8) may be computed using mesh-based approximations. In this case centered finite-difference schemes of fourth order accuracy have been used to approximate partial derivatives. The procedure outlined in Chap. 1 is used to solve the Poisson equation (Eq.(2.4)). The approximated rate-of-change of vorticity and the velocity is then interpolated back to the particles, to advance particle-position and particle-vorticity. The particle mesh interpolation is illustrated in Fig. 2.1.

The distribution of particle-vorticity onto a uniform mesh is written

$$\boldsymbol{\omega}(\boldsymbol{x},t) \approx \sum_p \boldsymbol{\omega}_p(t) v_p W\left(\frac{\boldsymbol{x}-\boldsymbol{x}_p}{h}\right), \tag{2.9}$$

where W is an interpolation kernel. The multidimensional tensor product of the twice differentiable interpolation function $M_4'(x)$ in Eq. (2.11) (Monaghan, 1985) is commonly used for W in

vortex methods. It conserves the first three moments of the distribution interpolated. Also the fourth order accurate function in Eq. (2.12) (M_6^*), introduced by Bergdorf (2007), has been considered in the current work. It was shown van Rees et al. (2011) that a kernel based on the M_6^* function significantly improves the accuracy of the 3D vortex method in marginally resolved and underresolved simulations at the cost of increased computational cost. The 3D stencil of the discrete interpolation operator based on M_4' has a support of 3^3 grid points whereas M_6^* requires 4^3. For completeness, also the second order kernel with 2^3 support (M_2) is given in Eq. (2.10), which is positive and conserves the first two moments. The interpolation functions have been plotted in Fig. 2.2 in real-space and Fourier-space.

$$M_2(x) = \begin{cases} 0 & \text{for } |x| > 1 \\ 1 - |x| & \text{for } |x| \leq 1, \end{cases} \tag{2.10}$$

$$M_4'(x) = \begin{cases} 0 & \text{for } |x| > 2 \\ \frac{1}{2}(2 - |x|)^2(1 - |x|) & \text{for } 1 < |x| \leq 2 \\ 1 - \frac{5|x|^2}{2} + \frac{3|x|^3}{2} & \text{for } |x| \leq 1. \end{cases} \tag{2.11}$$

$$M_6^*(x) = \begin{cases} 0 & \text{for } |x| > 3 \\ -\frac{1}{24}(|x| - 2)(|x| - 3)^3(5|x| - 8) & \text{for } 1 < |x| \leq 2 \\ \frac{1}{24}(|x| - 1)(|x| - 2)(25|x|^3 - 114|x|^2 + 153|x| - 48) & \text{for } 1 < |x| \leq 2 \\ -\frac{1}{12}(|x| - 1)(25|x|^4 - 38|x|^3 - 3|x|^2 + 12|x| + 12) & \text{for } |x| \leq 1 \end{cases} \tag{2.12}$$

Evaluation of the particle velocity by solving the Poisson equation Eq. (2.4) constitute a critical part of vortex-methods in terms of accuracy and computational efficiency. The Poisson equation is an elliptic equation hence the solution at one point relies on information from all other points in the problem. The basis of most approaches to this problem is to formulate the solution as a convolution of the right-hand-side with the elementary solution to the Poisson equation (G) known as the Green's function solution

$$\boldsymbol{\Psi}(\boldsymbol{x}) = \int_{-\infty}^{\infty} G(\boldsymbol{x} - \boldsymbol{x}')\boldsymbol{\omega}(\boldsymbol{x}')\,\mathrm{d}^d\boldsymbol{x}', \quad \boldsymbol{\nabla}^2 G = -\delta(\boldsymbol{x} - \boldsymbol{x}') \tag{2.13}$$

$$\boldsymbol{u}_{\boldsymbol{\omega}}(\boldsymbol{x}) = \int_{-\infty}^{\infty} \boldsymbol{\nabla} G(\boldsymbol{x} - \boldsymbol{x}') \times \boldsymbol{\omega}(\boldsymbol{x}')\,\mathrm{d}^d\boldsymbol{x}'. \tag{2.14}$$

Using the particle approximation (Eq. (2.6)) it follows that the potential and velocity are approximated correspondingly as

$$\boldsymbol{\Psi}(\boldsymbol{x}) = \sum_p^N G(\boldsymbol{x} - \boldsymbol{x}_p)\boldsymbol{\omega}(\boldsymbol{x}_p)v_p, \quad \boldsymbol{\nabla}^2 G_\epsilon = -\zeta(\boldsymbol{x} - \boldsymbol{x}') \tag{2.15}$$

$$\boldsymbol{u}_{\boldsymbol{\omega}}(\boldsymbol{x}) = \sum_p^N \nabla G_\epsilon(\boldsymbol{x} - \boldsymbol{x}_p) \times \boldsymbol{\omega}(\boldsymbol{x}_p)v_p. \tag{2.16}$$

The direct evaluation of Eq. (2.15) or Eq.(2.16) requires $\mathcal{O}(N^2)$ arithmetic operations. The Fast Multipole Method (FMM) (Greengard and Rokhlin, 1987; Carrier et al., 1988) achieves optimal

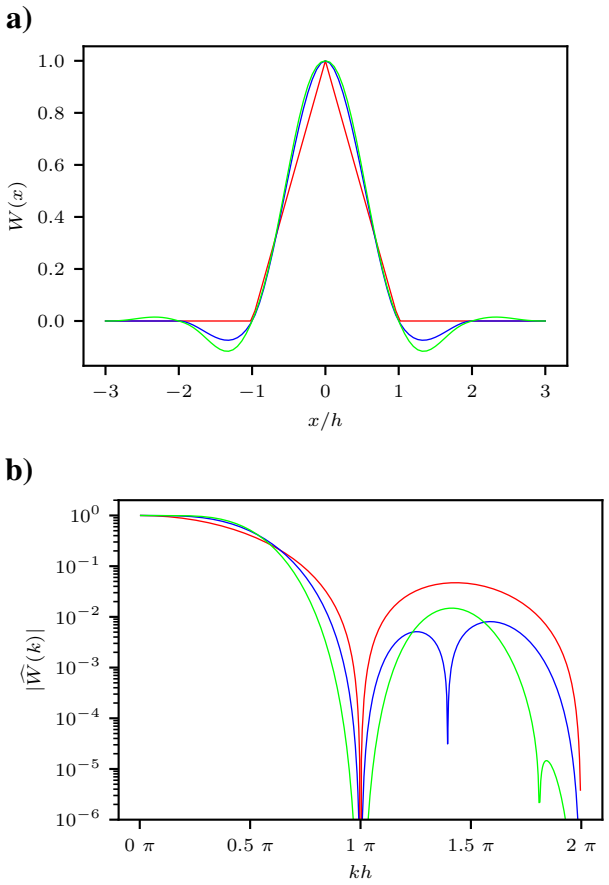

Figure 2.2: Interpolation kernels using M_2 (—) , M_4' (—) , M_6^* (—) : (a) Real-space. (b) Fourier-space. h is the mesh spacing and k is the wavenumber.

$\mathcal{O}(N)$ scaling of operation by including only the nearest neighbor particles in the direct summation and otherwise the lumped charges (by multipole expansion) of well separated particles in larger and larger clusters, using a hierarchical decomposition of the computational domain. This method is very versatile in the sense that it handles well a non-uniform distribution of the particles.

Particle-mesh methods may utilize fast mesh-based Poisson solvers, by either convolution via the fast Fourier transforms and the domain doubling technique by Hockney and Eastwood (1988) to achieve unbounded directions or by inversion of the discrete Laplacian operator (e.g. constructed by finite-difference approximations) using fast linear solvers such as as Multigrid. In the later case the boundary conditions are restricted to be of type Dirichlet, Neumann or periodic. Previous work have achieved unbounded directions by combining the FMM with the solvers that are not based on convolution. In that case, FMM is responsible for computing the Dirichlet conditions required by the mesh-based solver. This has also been done to achieve efficient adaptive multilevel decomposition without the need to perform Schwarz-iterations (Bergdorf et al., 2005; Cocle et al., 2008)

This work use the Fourier-based solver introduced in Chap. 1. The reader is referred to the references (Langston et al., 2011; Malhotra and Biros, 2015) for details on higher-order FMM methods for partial differential equations in general and (Gholami et al., 2016) for a detailed comparison of the computational efforts required by the various methods mentioned.

2.2 Constraints on the time-step size

The use of explicit time stepping in vortex-methods constrains the size of the time-step for numerical stability. The convective transport term $((\boldsymbol{u} \cdot \boldsymbol{\nabla})\boldsymbol{\omega})$ does not explicitly appear in the Lagrangian formulation Eq. (2.7) and Eq. (2.8), hence the time step used with the method is not limited by the usual Eulerian CFL condition. Instead, the time step is limited by a strain time scale

$$\|\omega\|_\infty \Delta t < C_{\text{LCFL}}, \tag{2.17}$$

where $C_{\text{LCFL}} \approx \mathcal{O}(1)$ (Chatelain et al., 2008). In addition, the spatiotemporal discretization of the solution yields a Fourier condition due to the viscous term as in Eulerian methods

$$\frac{\nu \Delta t}{h^2} < C_{\text{Fo}}. \tag{2.18}$$

The constant (C_{Fo}) depends on the time stepping scheme. Here, explicit Runge-Kutta schemes are considered with $C_{\text{Fo}} \geq \frac{1}{4}$.

2.3 Vorticity re-projection

In vortex-particle methods the velocity field is computed from the vorticity field by solving Eq. (2.4), which ensures that the velocity is divergence free (to the level of accuracy of the discrete approximation). This is not ensured for the vorticity. To avoid an accumulation of divergence of the vorticity field during simulation, the intermediate vorticity field ($\tilde{\boldsymbol{\omega}}$) is typically

re-projected onto a divergence-free field ($\boldsymbol{\omega} = \boldsymbol{\nabla} \times \boldsymbol{u}$) once every few time-steps by applying a Helmholtz decomposition to the vorticity field

$$\tilde{\boldsymbol{\omega}} = \boldsymbol{\nabla} \times \boldsymbol{u} - \boldsymbol{\nabla} a, \quad \boldsymbol{\nabla} \cdot \boldsymbol{u} = 0. \tag{2.19}$$

A Poisson equation (Eq. (2.20)) is solved for the scalar potential (a) which is used to correct intermediate vorticity as

$$\boldsymbol{\nabla}^2 a = -\boldsymbol{\nabla} \cdot \tilde{\boldsymbol{\omega}} \tag{2.20}$$

$$\boldsymbol{\omega} = \tilde{\boldsymbol{\omega}} + \boldsymbol{\nabla} a. \tag{2.21}$$

It is noted that the re-projection (Eq. (2.21)) does not modify the vorticity field if the vorticity divergence is zero. The correction is conveniently applied in Fourier-space when solving for the velocity using that

$$a = \boldsymbol{\nabla} \cdot \boldsymbol{\Psi}. \tag{2.22}$$

Hence the additional computational efforts of this operation are those associated with the inverse DFT of the corrected vorticity Fourier coefficients.

2.4 Instability of counter rotating vortex pairs

We illustrate an application of the FFT-based Poisson solver with the VPM method for a problem with mixed boundary conditions (two unbounded and one periodic direction) by simulating the evolution of two counter rotating vortex pairs from an initial state (Winckelmans et al., 2005; Chatelain et al., 2008; Chatelain and Koumoutsakos, 2010). For the Poisson solver we use the Green's function derived by Gaussian regularization with $m = 10$ and $\alpha = 1.5$.

The initial vorticity field consists of two counter rotating vortex-pairs given as

$$\boldsymbol{\omega} = \sum_i^2 \frac{\Gamma_i}{\pi} \left(\frac{\phi}{p_i^2 + \phi^2} \right)^2 \boldsymbol{e}_z - \sum_i^2 \frac{\Gamma_i}{\pi} \left(\frac{\phi}{q_i^2 + \phi^2} \right)^2 \boldsymbol{e}_z, \tag{2.23}$$

$$p_i^2 = (x + b_i)^2 + (y - \epsilon)^2, \quad q_i^2 = (x - b_i)^2 + (y - \epsilon)^2, \tag{2.24}$$

where z is the periodic direction and p_i, q_i are the perturbed radii of the respective vortices in the unbounded plane. Following (Winckelmans et al., 2005; Chatelain et al., 2008; Chatelain and Koumoutsakos, 2010) we use $\Gamma_2/\Gamma_1 = -0.3$, $b_2/b_1 = 0.3$, $\phi_1/b_1 = 0.075$ and $\phi_2/b_1 = 0.05$ and define the timescale and the Reynolds number based on the initial circulation ($\Gamma_0 = \Gamma_1 + \Gamma_2$) and centroid ($b_0 = [\Gamma_1 b_1 + \Gamma_2 b_2] / \Gamma_0$)

$$T = 2\pi b_0^2 / \Gamma_0, \quad \mathrm{Re} = \Gamma_0 / \nu = 3500. \tag{2.25}$$

The system is primarily unstable to the mode of wave length $\lambda_z/b_0 = 0.76$ (Winckelmans et al., 2005; Chatelain et al., 2008). To onset the instability the perturbation is set as $\epsilon(z) = 10^{-5} b_0 \sin(2\pi z/\lambda_z)$. The computational domain spans a single wave length of this mode in the periodic direction ($L_z = \lambda_z$) and the span in the unbounded directions is adapted to encapsulate vortex-particles for which $|\boldsymbol{\omega}_p| > 10^{-4} |\boldsymbol{\omega}|_{\max}$.

We measure the time variation of the enstrophy (Ω) and the distribution of kinetic energy among wave numbers ($E(k_z)$)

$$\Omega = \int \boldsymbol{\omega}(x,y,z) \cdot \boldsymbol{\omega}(x,y,z)\, dV \tag{2.26}$$

$$E(k_z) = \int\int \frac{1}{2}\left(\widehat{\boldsymbol{\Psi}}^*(x,y,k_z) \cdot \widehat{\boldsymbol{\omega}}(x,y,k_z) + \widehat{\boldsymbol{\omega}}^*(x,y,k_z) \cdot \widehat{\boldsymbol{\Psi}}(x,y,k_z)\right)\, dx\, dy. \tag{2.27}$$

The enstrophy evolution has been plotted in Fig. 2.3(a). It may be seen that the obtained results converge (with mesh refinement) towards the same solution as obtained in (Chatelain and Koumoutsakos, 2010) (for $h/L_z = 256$). Furthermore the time history of kinetic energy associated with first three modes has been plotted in Fig. 2.3(b) and shows very similar growth rates as in (Chatelain and Koumoutsakos, 2010) though the current results are slightly delayed possible due different perturbation applied or other variations in the algorithms (e.g. time stepping and projection-scheme). isocontours of the vorticity magnitude have been plotted at several times in Fig. 2.4. These show a transition from a 2D state into a 3D state primarily through the perturbed wave length. The 3D dynamic involves a stretching of one pair member around the other and creation of smaller scales in the solution through non-linear interaction.

2.5 Summary

In this chapter the VPM method was outlined and demonstrated for a mixture of free-space and periodic boundary condition by simulating the break down of two counter rotating vortex pairs.

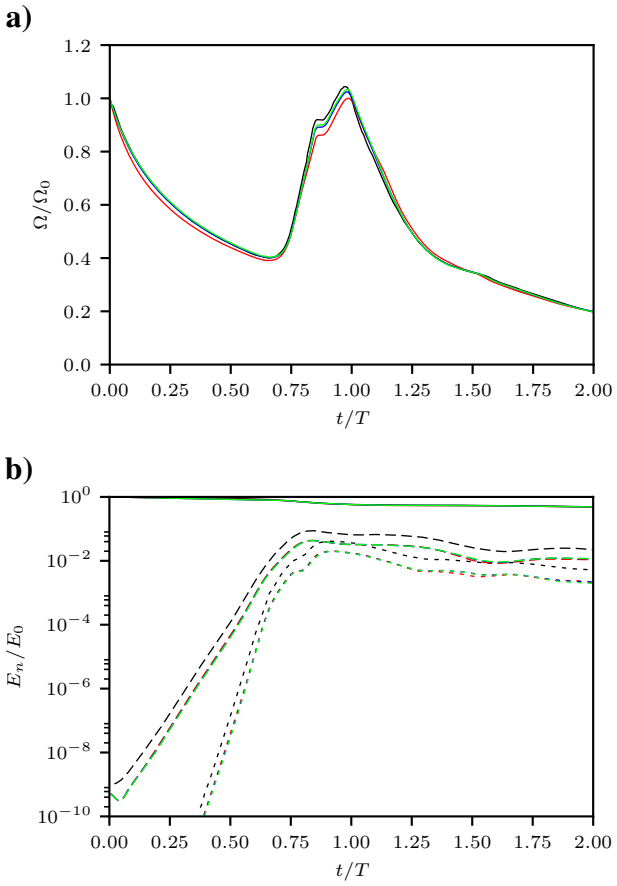

Figure 2.3: (a) Evolution of enstrophy. (b) Evolution of kinetic energy associated with first three modes: 0^{th} (solid), 1^{st} (dashed), 2^{nd} (dotted). Line colors indicate results from: (Chatelain and Koumoutsakos, 2010) (—) , simulation for $h/L_z = 64$ (—) , simulation for $h/L_z = 128$ (—) , simulation for $h/L_z = 256$ (—) .

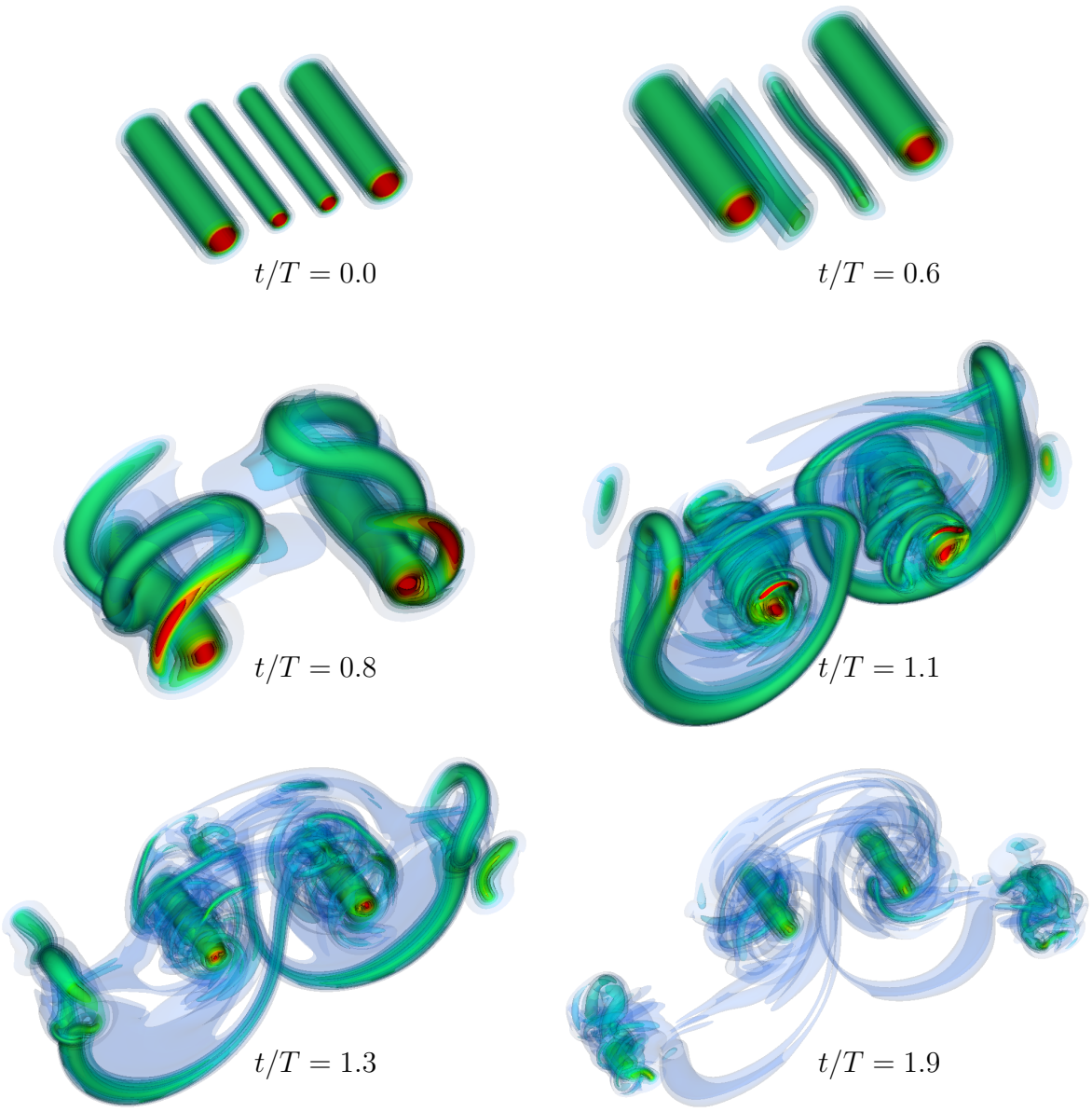

Figure 2.4: Isocontours of the vorticity magnitude from blue to red $|\boldsymbol{\omega} b_1^2/\Gamma_0| = [1, 4, 8, 12, 16, 20, 24, 28, 32]$ at various times for simulation with $h/L_z = 128$.

Chapter 3

Solid bodies

This chapter regards modeling of fluid flow past solid bodies. The chapter is an edited version of the paper "Iterative Brinkman penalization for simulation of impulsively started flow past a sphere and a circular disk" published in Journal of Computational Physics 2017 (Spietz et al., 2017a). Further, it include some new material.

Conventionally, the analysis of fluid-structure interaction requires the use of conformal meshes to enforce the no-slip boundary condition on computational points located at the solid-fluid interface. The solid boundary condition may also be enforced with non-conformal meshes using immersed boundary methods Peskin (1972); Goldstein et al. (1993) or fictitious domain methods which rely on a modification of the governing equations. These methods may be interesting since they avoid time consuming generation of high quality, non-orthogonal grids, that require non-trivial solution algorithms.

One immersed boundary method is the Brinkman penalization method (Angot et al., 1999; Khadra et al., 2000; Kevlahan and Ghidaglia, 2001). The principle of the method is to model a fluid flow in a porous medium by adding volume forcing to the governing equations. The porous medium flow tends to the primary flow past a non-porous immersed body as the permeability is reduced to zero in the part of the flow occupied by the solid body.

The main challenge of the penalization method is that it may lead to mollified interface. Another interesting branch of the immersed boundary methods for particle methods aims at providing sharp interfaces, by introducing control points on the interface itself not neccesarily coinciding with the background mesh (Poncet, 2009; Marichal et al., 2016; Gillis et al., 2018). The main complexity of these *immersed interface methods* lies in the adaptation of the numerical schemes near the interface.

In the field of vortex methods several numerical schemes are based on the penalization method (Coquerelle and Cottet, 2008; Rossinelli et al., 2010; El Ossmani and Poncet, 2010; Rasmussen et al., 2010; Hejlesen et al., 2015a; Gazzola et al., 2011b; Mimeau et al., 2015, 2016). Hejlesen et al. (2015a) proposed an iterative variation of the explicit scheme for the simulation of 2D fluid flow past solid obstacles with the VPM method. This iterative method uses a split-step scheme that overcomes a drawback of the conventional non-iterative schemes for vorticity-velocity formulation of the Navier-Stokes equations. For the non-iterative schemes an accurate enforcement of the solid boundary condition restricts the time step size because the numerical formulation lacks the global coupling of the Poisson equation. In this chapter we present this technique and show that it is extendable to 3D flows.

The proposed method is applied to the impulsively started flow past a sphere and the results are compared to those of Mimeau et al. (2016) and Ploumhans et al. (2002). The work by Mimeau et al. (2016) includes a study of the flow past a sphere using the non-iterative implicit penalization. The focus of their studies is on the space-developing simulations since the

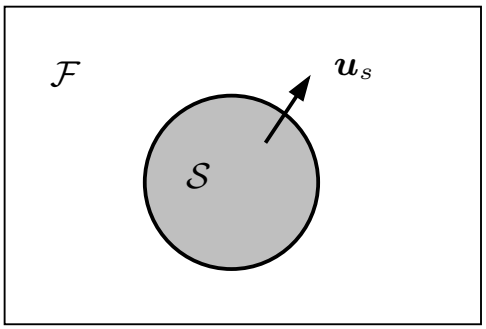

Figure 3.1: Domain consisting of a solid and a fluid part.

velocity-vorticity relation is solved using a periodic Poisson solver with a velocity correction step to account for outflow of vorticity in the stream wise direction. Results are obtained for $\mathrm{Re} = 300$ and $\mathrm{Re} = 1000$ in simulated times long enough for the flows to reach a steady state. In this chapter, we focus on the impact of the iterative process on accelerated flows, hence our approach avoids potential artifacts due to outflow boundary conditions. However, this limits the time span of the simulation due to growing extent of domain with time. In Sec. 3.4.3 we briefly assess the need to modify the unbounded boundary condition when using wake truncation in bluff body flow. Ploumhans et al. (2002) studied the flow past a sphere at various Reynolds numbers using a particle vortex method combined with a boundary element method (BEM) and panel-vortex diffusion to enforce the no-slip condition at the fluid-solid interface. They did not use outflow boundary conditions, but a mapping to a non-uniform grid to reduce the computational costs. Moreover, we present results for the simulation of the impulsively started flow normal to a circular disc of finite thickness at $\mathrm{Re} = 500$.

3.1 The Brinkman penalization method

We solve the incompressible Navier-Stokes equations in a domain (Ω) consisting of a solid region ($\mathcal{S} \in \Omega$) and a fluid region ($\mathcal{F} = \Omega \setminus \mathcal{S}$) cf. Fig.3.1. We introduce the Brinkman term that penalizes the difference between the solid velocity ($\boldsymbol{u}_s$) and the flow fluid velocity ($\boldsymbol{u}$) within the solid body to be close to zero (Angot et al., 1999). Here we consider the vorticity-velocity formulation of the Navier-Stokes equations

$$\frac{\partial \boldsymbol{\omega}}{\partial t} + (\boldsymbol{u} \cdot \boldsymbol{\nabla})\boldsymbol{\omega} = (\boldsymbol{\omega} \cdot \boldsymbol{\nabla})\boldsymbol{u} + \nu \boldsymbol{\nabla}^2 \boldsymbol{\omega} + \boldsymbol{\nabla} \times \left[\lambda \chi (\boldsymbol{u}_s - \boldsymbol{u})\right], \tag{3.1}$$

where λ is a penalization parameter, which may be seen as the inverse permeability of the solid region and χ is the characteristic function of $\mathcal{S}$

$$\chi(\boldsymbol{x}) = \begin{cases} 1 & \text{for } \boldsymbol{x} \in \mathcal{S} \\ 0 & \text{for } \boldsymbol{x} \in \mathcal{F}. \end{cases} \tag{3.2}$$

We note that the Brinkman penalization term may be expanded as

$$\boldsymbol{\nabla} \times [\lambda \chi (\boldsymbol{u}_s - \boldsymbol{u})] = \lambda \boldsymbol{\nabla} \chi \times (\boldsymbol{u}_s - \boldsymbol{u}) + \lambda \chi (\boldsymbol{\omega}_s - \boldsymbol{\omega}), \tag{3.3}$$

where $\boldsymbol{\omega}_s = \boldsymbol{\nabla} \times \boldsymbol{u}_s$. The term causes a production of vorticity in Eq. (3.1) due to residual in the velocity field ($\boldsymbol{u}_s - \boldsymbol{u}$) and vorticity field ($\boldsymbol{\omega}_s - \boldsymbol{\omega}$). $\boldsymbol{\nabla}\chi$ is a vector field with non-zero magnitude only at the fluid-solid interface and is orientated normal to the interface. Hence, this production term is zero where the residual velocity ($\boldsymbol{u}_s - \boldsymbol{u}$) is also normal to the interface. As a consequence, when the Brinkman term is approximated separately from the elliptic kinematic relation between the dependent variables, the enforcement of the solid boundary condition will be delayed in time. This short-coming is distinctive in accelerated flows past objects, whose geometries have the majority of the surface area normal to the flow direction. This effect has been illustrated by Hejlesen et al. (2015a) for the impulsively started flow normal to a flat plate and it is the motivation for considering the impulsively started flow normal to a circular disc in the present study.

3.2 Numerical implementation of the Brinkman penalization method in a re-meshed vortex method

We solve the modified vorticity transport equation (Eq. (3.1)) in a split-step algorithm

$$\frac{\partial \boldsymbol{\omega}}{\partial t} = \boldsymbol{\nabla} \times \left[\lambda\chi\left(\boldsymbol{u}_s - \boldsymbol{u}\right)\right], \tag{3.4}$$

$$\frac{D\boldsymbol{\omega}}{Dt} = (\boldsymbol{\omega}\cdot\boldsymbol{\nabla})\boldsymbol{u} + \nu\boldsymbol{\nabla}^2\boldsymbol{\omega}. \tag{3.5}$$

Using the discrete approximation, Eq. (3.5) becomes a system of coupled ordinary differential equations, which is solved in the Lagrangian frame of reference

$$\frac{\mathrm{d}\boldsymbol{x}_p}{\mathrm{d}t} = \boldsymbol{u}(\boldsymbol{x}_p, t) \tag{3.6}$$

$$\frac{\mathrm{d}\boldsymbol{\omega}_p}{\mathrm{d}t} = \left[(\boldsymbol{\omega}\cdot\boldsymbol{\nabla})\boldsymbol{u} + \nu\boldsymbol{\nabla}^2\boldsymbol{\omega}\right]_p. \tag{3.7}$$

We denote the solution to Eq. (3.4) $\boldsymbol{\omega}^*$ and the corresponding velocity field $\boldsymbol{u}^*$. We write the solution as a correction ($\boldsymbol{\xi}$) to the vorticity field prior to this step ($\boldsymbol{\omega}$)

$$\boldsymbol{\omega}^* = \boldsymbol{\omega} + \boldsymbol{\xi}. \tag{3.8}$$

The correction may be determined by discretizing Eq. (3.4) using either the explicit or the implicit Euler scheme as respectively

$$\boldsymbol{\xi}_{\text{exp}} = \boldsymbol{\nabla} \times (\Delta t\lambda\chi\boldsymbol{v}_0) \tag{3.9}$$

or

$$\boldsymbol{\xi}_{\text{imp}} = \boldsymbol{\nabla} \times [\Delta t\lambda\chi(\boldsymbol{u}_s - \boldsymbol{u}^*)] = \boldsymbol{\nabla} \times \left(\frac{\Delta t\lambda\chi}{1+\Delta t\lambda\chi}\boldsymbol{v}_0\right), \tag{3.10}$$

where $\boldsymbol{v}_0 = \boldsymbol{u}_s - \boldsymbol{u}$ is the velocity residual to be penalized. With the Brinkman technique λ is controlling how effectively the solid boundary condition is enforced, hence it is desirable to set it as large possible. The explicit scheme (Eq. (3.9)) is stable for $0 < \lambda \leq \frac{2}{\Delta t}$ whereas the

implicit scheme (Eq. (3.10)) is unconditionally stable and thus formally better suited for the discretization. However, Rasmussen et al. (2011) noticed that when the explicit scheme is used with $\lambda = \frac{1}{\Delta t}$ the two schemes are essentially the same and differs only in the way the mollified characteristic function of the solid blends into the fluid. We note that

$$\lim_{\lambda=\infty} \frac{\Delta t \lambda \chi}{1 + \Delta t \lambda \chi} = \chi. \tag{3.11}$$

Consequently, if the mask (χ) is a Heaviside function the implicit scheme, in the limit of $\lambda \rightarrow \infty$, is equivalent to the explicit scheme using $\lambda = \frac{1}{\Delta t}$.

When the Brinkman method is used in a discrete vorticity formulation as Eq. (3.9) or Eq. (3.10), the mesh points where penalization vorticity ($\boldsymbol{\xi}$) may be produced in a single time step depend on velocity residual within the solid ($\boldsymbol{u}_s - \boldsymbol{u}^n$) and on the geometry of the solid cf. Eq. (3.3). Hence, only if the penalization vorticity is found, while invoking the elliptic relation between vorticity and velocity cf. Eq. (2.4), a strong coupling between the two dependent variables may be enforced in the general case. To achieve this we compute the correction ($\boldsymbol{\xi}$) in a number of iterations (N_i) as Eq. (3.12) and Eq. (3.13) using an update based on a generalization of Eq. (3.9).

$$\boldsymbol{\xi}^{k+1} = \boldsymbol{\xi}^k + \eta \boldsymbol{\nabla} \times \left[\chi \left(\boldsymbol{v}_0 - \boldsymbol{u}_\xi^k \right) \right], \tag{3.12}$$

$$\boldsymbol{\nabla}^2 \boldsymbol{u}_\xi^{k+1} = -\boldsymbol{\nabla} \times \boldsymbol{\xi}^{k+1} \quad \text{for} \quad k = 1, 2, ...N_i, \tag{3.13}$$

Here η is a relaxation parameter, and the process is stable for $0 < \eta \leq 2$. The reader is referred to Hejlesen et al. (2015a) for the details on the derivation of Eq. (3.12) and Eq. (3.13).

Termination of the process we base on a criteria using the second norm of vorticity ($\mathcal{E}$) introduced between iterations as

$$\frac{|\mathcal{E}^{k+1} - \mathcal{E}^k|}{\mathcal{E}^k} < \varepsilon, \quad \mathcal{E}^k = \int \boldsymbol{\xi}^k \cdot \boldsymbol{\xi}^k \, \mathrm{d}V, \tag{3.14}$$

where ε is a specified tolerance.

The accuracy of the Brinkman method may be quantified by considering the residual velocity ($||\frac{\boldsymbol{u}_s - \boldsymbol{u}}{U}||$) within the solid. When the Brinkman method is used in the velocity-pressure formulation the L_∞-norm of the residual velocity has been related to λ as $\mathcal{O}\left(\lambda^{-0.5}\right)$ by Angot et al. (1999). This relationship does not hold in the general case as the geometry of the solid may have a significant influence as shown by Hejlesen et al. (2015a), who considered the vorticity formulation.

In the iterative process (Eq. (3.12) and Eq. (3.13)) λ has been eliminated as a free parameter and replaced it by a relaxation parameter (η) and a termination criteria governing the number of iterations (N_i). We observe from experiments that using the iterative process the residual may be reduced with the iteration number asymptotically as $\mathcal{O}\left(N_i^\beta\right)$, where $\beta \simeq -0.5$ independent of the global time step.

In the present method $\boldsymbol{\xi}$ will be non-zero only in the immediate vicinity of the solid body if a compact approximation to the curl in Eq. (3.12) is applied. In flows where the solid region is small compared to extent of the vorticity field, the computational efforts associated with solving the Poisson equation for $\boldsymbol{u}_\xi$ every iteration is reduced by computing $\boldsymbol{\xi}$ separately from $\boldsymbol{\omega}$ using a smaller sub-set of the computational mesh as indicated in Fig. 3.2.

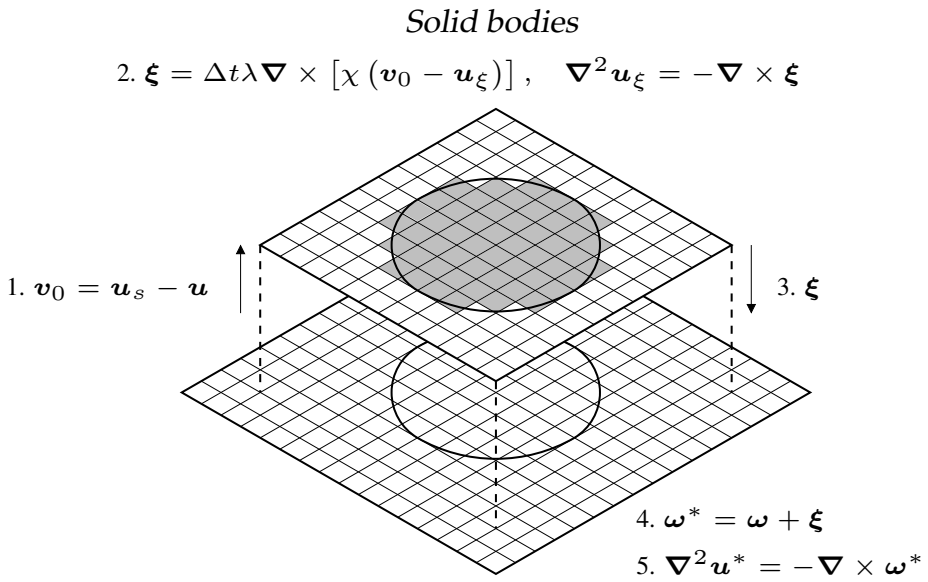

Figure 3.2: The penalization vorticity may be solved on a subdomain enclosing the solid body. The procedure is summarized in the steps 1–5.

In other implementations of the Brinkman penalization method (Rossinelli et al., 2010; Rasmussen et al., 2010; Gazzola et al., 2011b) χ have been replaced by a smooth approximation, since it is a Heaviside function, and the derivative of a Heaviside function is a singularity. In the present study we approximate the curl of the term $\chi(\boldsymbol{u}_s - \boldsymbol{u})$ (that may be discontinuous) by second order finite difference (unless otherwise specified) to avoid the dependency on an additional mollification length. The high order, regularized Poisson solver guarantees a smooth velocity field and in addition, the vorticity due to penalization is smoothed explicitly to be consistent with the regularized solution obtained with the higher order Poisson solver. This we do by linear convolution of the vorticity field with a the regularization kernel used for the Poisson equation

$$\boldsymbol{\xi}_\epsilon = \zeta * \boldsymbol{\xi}. \tag{3.15}$$

Another view on the iterative penalization method was given by Gillis et al. (2017). Here, the penalization vorticity is found by solving the linear system

$$\boldsymbol{A}\boldsymbol{\xi} = \boldsymbol{b}, \quad \boldsymbol{b} = \boldsymbol{\nabla} \times \left[\chi \boldsymbol{v}_0\right], \tag{3.16}$$

where the linear operator ($\boldsymbol{A}$) is defined as

$$\boldsymbol{A}: \quad \xi \rightarrow \boldsymbol{\nabla} \times \left[\chi \boldsymbol{u}_\xi\right], \tag{3.17}$$

Gillis et al. (2017) proposed to solve the matrix equation (Eq. (3.16)) using Krylov based iterative solvers for non-symmetric systems e.g. by *generalized minimum residual* type solvers or the *bi-conjugate-gradient-stabilized* solution technique, both which do not require the evaluation of the transpose of $\boldsymbol{A}$. Further, Gillis et al. (2017) applied solution-recycling to increase the efficiency. We, note that our approach cf. Eq. (3.12)–Eq. (3.13) corresponds to solving the matrix equation (Eq. (3.16)) using a relaxed Richardson iterative solver

$$\boldsymbol{\xi}^{k+1} = \boldsymbol{\xi}^k + \eta(\boldsymbol{b} - \boldsymbol{A}\boldsymbol{\xi}^k). \tag{3.18}$$

Further, that $\boldsymbol{A}$ involves the inverse Laplacian $(\nabla^2)^{-1}$ i.e. it requires the solution of the Poisson equation (Eq. (3.13)). In preliminary studies it was observed that by applying the more advanced iterative solvers, the solution (ξ) becomes highly oscillatory. This we relate to the low-pass filtering associated with the Poisson solver in the current method, which implies high-pass filtering in the inverse direction, hence solving Eq. (3.16) is actually discrete deconvolution. The challenges observed are analogues to those of Beale's method (Beale, 1988) (see discussion in Cottet and Koumoutsakos (2000)). In comparison the studies in Gillis et al. (2017) were carried out for singular Green's functions. We observed that with the proposed Poisson solver the use of the relaxed Richardson solver followed by a regularization step cf. Eq. (3.15), although less efficient, results in stable convergence of the residual and in non-oscillatory solutions in time.

3.3 Calculation of the aerodynamic force and moment

The total aerodynamic force ($\boldsymbol{F}$) and moment $\boldsymbol{M}_c$ acting on a solid body may be computed from the rate of change of the first and second order moment of the vorticity distribution and an inertia term cf. Wu (1978). For a rigid body moving with solid body velocity ($\tilde{\boldsymbol{u}}_s$) the force and moment in d-dimensions are given by

$$\boldsymbol{F} = -\rho\frac{1}{d-1}\frac{\mathrm{d}}{\mathrm{d}t}\int_\Omega \boldsymbol{x}\times\boldsymbol{\omega}\,\mathrm{d}V + \rho\frac{\mathrm{d}}{\mathrm{d}t}\int_\mathcal{S}\tilde{\boldsymbol{u}}_s\,\mathrm{d}V, \tag{3.19}$$

$$\boldsymbol{M}_c = -\rho\frac{1}{2}\frac{\mathrm{d}}{\mathrm{d}t}\int_\Omega |\boldsymbol{x}-\boldsymbol{x}_c|^2\boldsymbol{\omega}\,\mathrm{d}V + \rho\frac{\mathrm{d}}{\mathrm{d}t}\int_\mathcal{S}(\boldsymbol{x}-\boldsymbol{x}_c)\times\tilde{\boldsymbol{u}}_s\,\mathrm{d}V, \tag{3.20}$$

where ρ is the density of the fluid and $\boldsymbol{x}_c$ is the geometrical center of the solid. We note, that Eq. (3.19) requires an integration over the entire vorticity field extending e.g., to the far wake of the flow. In Ploumhans et al. (2002) it was noted, that this global formulation may be inaccurate when having a coarse spatial resolution in the far wake and found the local control volume approach by Noca et al. (1997, 1999) to be more accurate. In the present work it has been noticed that the global approach is also sensitive to truncation, introduced when the vorticity is advected out of the computational domain, which in practice is necessary to limit the computational effort in space-developing simulations. Instead we utilize that a change in the first moment of vorticity may only be due to non-conservative external forcing in the momentum equation (Saffman, 1992), which in the present study is due to the penalization function. Following Hejlesen et al. (2015a) we therefore exploit the vorticity decomposition Eq. (3.8) in Eq. (3.19) to obtain

$$\boldsymbol{F} = -\rho\frac{1}{d-1}\frac{\mathrm{d}}{\mathrm{d}t}\int_\Omega \boldsymbol{x}\times\boldsymbol{\xi}\,\mathrm{d}V + \rho\frac{\mathrm{d}}{\mathrm{d}t}\int_\mathcal{S}\tilde{\boldsymbol{u}}_s\,\mathrm{d}V, \tag{3.21}$$

$$\boldsymbol{M}_c = -\rho\frac{1}{2}\frac{\mathrm{d}}{\mathrm{d}t}\int_\Omega |\boldsymbol{x}-\boldsymbol{x}_c|^2\boldsymbol{\xi}\,\mathrm{d}V + \rho\frac{\mathrm{d}}{\mathrm{d}t}\int_\mathcal{S}(\boldsymbol{x}-\boldsymbol{x}_c)\times\tilde{\boldsymbol{u}}_s\,\mathrm{d}V. \tag{3.22}$$

This is a local measure and by using this for the evaluation of the total aerodynamic force and moment we avoid the aforementioned issues. The numerically evaluated total aerodynamic force by the two different expressions has been found in agreement if the rate of change of vorticity due to diffusion and stretching is integrated in time by the explicit Euler method such that it is treated consistently with the penalization term.

When computing aerodynamic force and moment it should noted that Eq. (3.19) and Eq. (3.20) are only applicable for unbounded flow. In the control volume formulation by Noca et al. (1997, 1999) the pressure is eliminated by the use of Stokes' theorem, which may only be applied if the whole body can be encompassed by a closed control surface, otherwise a modification is required (Tan et al., 2005). For the case of infinite-periodic structures, to obtain force and moment one option is to explicitly calculate the pressure. However, in that case, we propose to exploit tat the force and moment may be obtained directly by integration of the penalization term following Angot et al. (1999); Kolomenskiy and Schneider (2009) as

$$\boldsymbol{F} = \rho \lim_{\lambda\to\infty} \int_\Omega \lambda\chi(\boldsymbol{u}-\boldsymbol{u}_s)\,\mathrm{d}V + \rho\frac{\mathrm{d}}{\mathrm{d}t}\int_\mathcal{S} \tilde{\boldsymbol{u}}_s\,\mathrm{d}V, \tag{3.23}$$

$$\boldsymbol{M}_c = \rho \lim_{\lambda\to\infty} \int_\Omega \lambda\chi(\boldsymbol{x}-\boldsymbol{x}_c)\times(\boldsymbol{u}-\boldsymbol{u}_s)\,\mathrm{d}V + \rho\frac{\mathrm{d}}{\mathrm{d}t}\int_\mathcal{S} (\boldsymbol{x}-\boldsymbol{x}_c)\times\tilde{\boldsymbol{u}}_s\,\mathrm{d}V, \tag{3.24}$$

Since, the iterative sequence cf. Eqs. (3.12)–(3.13) may be viewed as a series of explicit Euler sub-steps, force and moment can be approximated as the average force and moment applied during iterations

$$\boldsymbol{F} \approx \rho\frac{\eta}{\Delta t}\sum_{k=1}^{N_i}\int_\Omega (\boldsymbol{u}^k-\boldsymbol{u}_s)\,\mathrm{d}V + \rho\frac{\mathrm{d}}{\mathrm{d}t}\int_\mathcal{S}\tilde{\boldsymbol{u}}_s\,\mathrm{d}V, \tag{3.25}$$

$$\boldsymbol{M}_c \approx \rho\frac{\eta}{\Delta t}\sum_{k=1}^{N_i}\int_\Omega (\boldsymbol{x}-\boldsymbol{x}_c)\times(\boldsymbol{u}^k-\boldsymbol{u}_s)\,\mathrm{d}V + \rho\frac{\mathrm{d}}{\mathrm{d}t}\int_\mathcal{S}(\boldsymbol{x}-\boldsymbol{x}_c)\times\tilde{\boldsymbol{u}}_s\,\mathrm{d}V. \tag{3.26}$$

3.4 Results

3.4.1 The impulsively started flow past a sphere at $\mathrm{Re}=1000$

We simulate the impulsively started flow past a stationary sphere at $\mathrm{Re}=1000$ as sketched in Fig. 3.3. The Reynolds number and dimensionless time, drag and lift coefficient are defined as respectively

$$\mathrm{Re}=\frac{UD}{\nu},\quad t^*=\frac{tU}{D},\quad C_D=\frac{F_x}{\left(\frac{1}{2}\rho U^2\right)\left(\frac{1}{4}\pi D^2\right)},\quad C_L=\frac{F_y}{\left(\frac{1}{2}\rho U^2\right)\left(\frac{1}{4}\pi D^2\right)}, \tag{3.27}$$

where D is the diameter of the sphere. We use a grid spacing of $h=128/D$ (unless otherwise stated). A second order explicit Runge-Kutta scheme is applied for the advancement of particles with time step size $\Delta t^*=0.005$. This time step has been found to give accurate results and is identical to the time step used by Ploumhans et al. (2002). The extent of the domain is updated every 50^{th} time step to prevent truncation of vortex particles that satisfy the threshold $|\boldsymbol{\omega}_p|/||\boldsymbol{\omega}_p||_\infty \geq 10^{-5}$. For the iterative scheme we employ a default convergence criteria of $\varepsilon=0.05$.

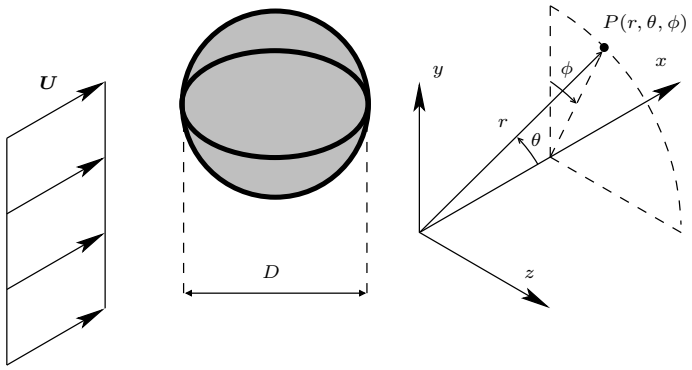

Figure 3.3: Impulsively started flow past a sphere of diameter (D). A Cartesian coordinate system (x, y, z) and a spherical coordinate system (r, θ, ϕ) have also been indicated. The origin of the coordinate systems is in the sketch displaced from their actual origin being the center of the sphere.

The potential flow solution and the axisymmetric stream function

The potential flow past a sphere may be described as a singular distribution of vorticity at the surface of the sphere. The potential flow is axisymmetric. Hence, it has zero variation with the polar angle (ϕ) in a spherical coordinate system cf. Fig. 3.3. The vortex sheet is (Batchelor, 1967)

$$\gamma = -\frac{3}{2} U \sin(\theta), \tag{3.28}$$

We compare the analytic solution (Eq. (3.28)) to our split-step result at the first time step of the impulsively started flow simulation. We refer to this as the solution at time $t^* = 0^+$. Though our simulation does not result in a singular distribution of vorticity at $t^* = 0^+$, we estimate the vortex sheet by interpolating the split-step vorticity onto a spherical grid ($N_r \times N_\theta \times N_\phi = 100 \times 50 \times 100$) and integrate in the radial direction as

$$\gamma = \int_0^\infty \omega_\phi^* \, \mathrm{d}r. \tag{3.29}$$

Fig. 3.4(a) and Fig. 3.4(b) shows that the iterative scheme using the relaxation parameter $\eta = 1$ results in a sheet that is in excellent agreement with the potential flow solution. The obtained sheet is approximately constant in the polar direction and the variations may be explained by errors due to having sampled the geometry of the sphere on a Cartesian grid when discretizing the characteristic function of Eq. (3.2).

Fig. 3.4(c) shows the vortex sheet by the iterative scheme using $\eta = 1$ compared to the vortex sheet by the non-iterative scheme for $\eta = 1$, $\eta = \frac{3}{2}$ and $\eta = 2$. The initial vortex sheet produced in a single iteration using Eq. (3.12) is $\gamma(\theta) = -\eta u_{\text{slip}}(\theta)$ when the solid is a sphere (in the absence of effects due to finite spatial resolution). The initial slip velocity is $u_{\text{slip}}(\theta) = U \sin(\theta)$, hence the potential solution is produced in a single iteration for $\eta = \frac{3}{2}$. The figure shows that the non-iterative scheme produces an almost equally well matching solution using $\eta = \frac{3}{2}$ as expected based on the aforementioned argument. Some oscillations are observed near $\theta = 0$

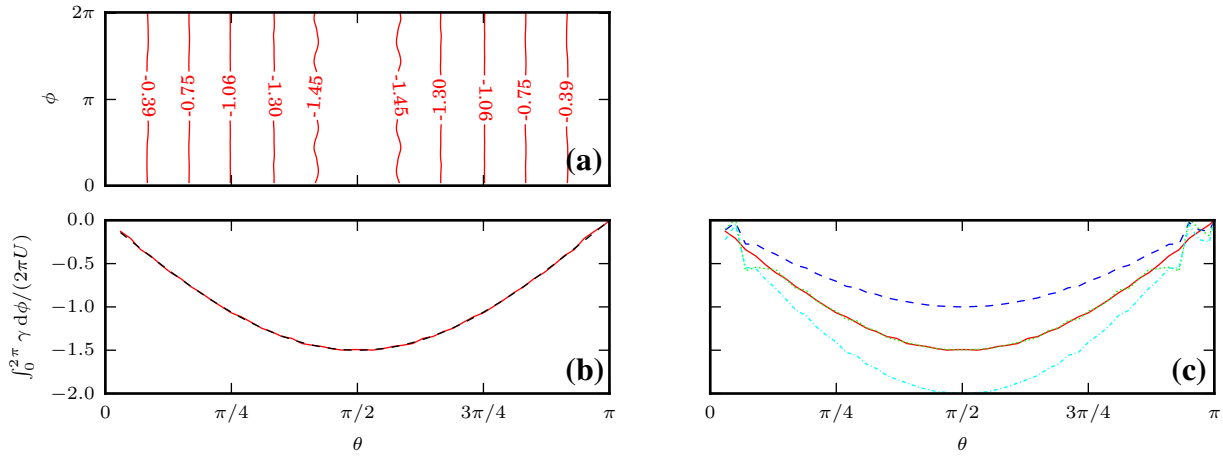

Figure 3.4: The vortex sheet at $t^* = 0^+$ by the present 3D Brinkman penalization method. (a) Isocontours of vortex sheet strength (normalized by U) obtained with the iterative scheme as function of azimuthal angle, θ and polar angle ϕ. (b) The vortex sheet strength using the iterative scheme and averaged in the polar direction (—) compared to the exact potential solution (- - -). (c) Vortex sheet strength at $t^* = 0^+$ by the iterative scheme legendredsolidnone and the non-iterative scheme using $\eta = 1$ (- - -), $\eta = \frac{3}{2}$ (·····) and $\eta = 2$ (- · -).

and $\theta = \pi$ due to finite spatial resolution. Evidently, the vortex sheet strength obtained without iterating is incorrect using other values of η

An axisymmetric stream function (φ) is computed from the simulated vector potential ($\boldsymbol{\psi}$), which is interpolated to a cylindrical grid ($N_r \times N_\phi \times N_x = 100 \times 100 \times 1.5D/h$) and averaged in the polar direction as

$$\varphi(r, x) = \frac{1}{2\pi} \int_0^{2\pi} r\boldsymbol{\psi}(r, \phi, x) \cdot \boldsymbol{e}_\phi \, \mathrm{d}\phi. \tag{3.30}$$

Isocontours of the axisymmetric stream function are shown in Fig. 3.5. The figure demonstrates that the iterative scheme is capable of accurately imposing the no-through boundary condition. The overestimation of the vortex sheet strength by using $\eta = 2$ with the non-iterative scheme causes a growth in the effective radius of the sphere and a back flow within the sphere at this time step. Setting $\eta = \frac{3}{2}$ yields a better boundary condition as compared to the two other non-iterative cases shown but is not as smooth and accurate near the surface of the sphere as obtained with the iterative scheme.

Convergence of drag coefficient at the early times of the simulation

We now consider the time interval $t^* \in [0, 1]$ and verify the consistency of the proposed method by measuring the convergence of the relative error on the drag coefficient for various spatial resolutions against the best resolved case as

$$\text{error}(t^*) = \frac{|C_D(t^*) - C_{D\,\text{best resolved}}(t^*)|}{|C_{D\,\text{best resolved}}(t^*)|}. \tag{3.31}$$

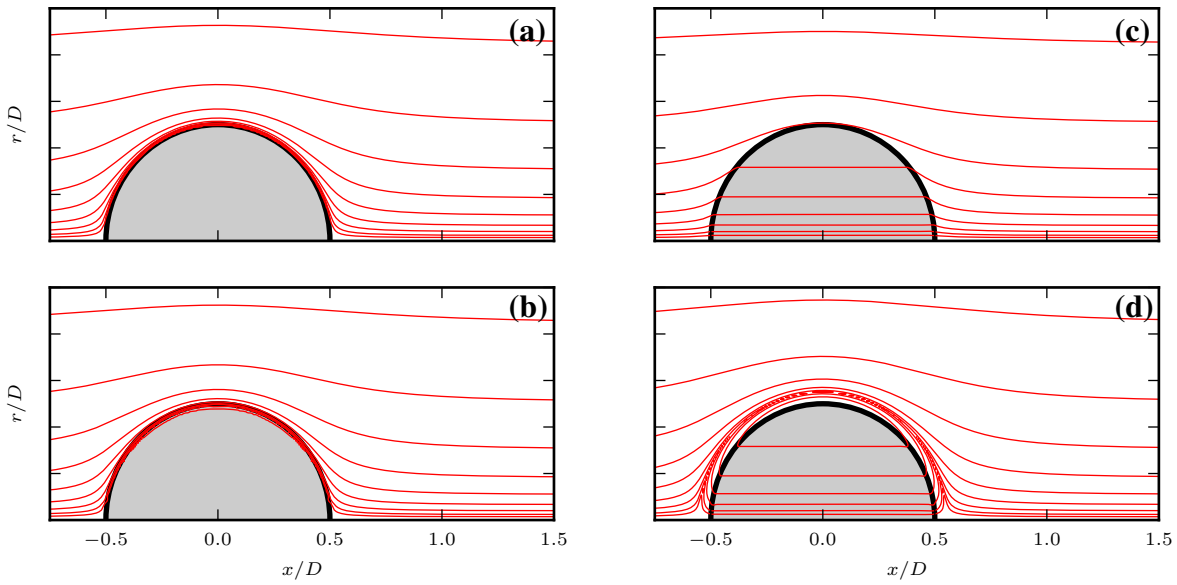

Figure 3.5: Isocontours of axisymmetric stream function in 10 logarithmically spaced levels in the interval $[-1, 1]$ at $t^* = 0^+$. (a) Solution for the iterative scheme using $\eta = 1$. (b) Solution for the non-iterative scheme using $\eta = 1$. (c) Solution for the non-iterative scheme using $\eta = \frac{3}{2}$. (d) Solution for the non-iterative scheme using $\eta = 2$.

The study is carried out for the iterative scheme using $\eta = 1$ and mesh spacings $D/h = 16$, 32, 48, 64, 96, 128 and 256. The error is shown in Fig. 3.6 and the temporal variation of the drag coefficient in the case with resolution $D/h = 128$ is shown in Fig. 3.7(a). The decay of the error-norms is approximately second order cf. Fig. 3.6. The rate of convergence is not increased by applying a fourth order finite difference scheme for computation of Eq. (3.12) rather than a second order scheme. This observation is consistent with the dependency of the maximum order of accuracy that may be achieved when solving Poisson equation as Eq. (2.4), on the number of continuous derivative of the vorticity field. In the current method the vorticity field becomes singular as we compute the rate of change of vorticity as the derivative of a Heaviside function (χ). However, the resulting velocity field is ensured to be sufficiently smooth to be used to approximate the solution to the governing equations ($\boldsymbol{u} \in \mathcal{C}^2$). We do not find that it is necessary to introduce an ad hoc mollification of χ. Instead we explicitly regularize the penalization-vorticity field by which the observed rate of convergence of the current method correspondents to that reported using a mollified χ (Gazzola et al., 2011b). The same study was also carried out using the M_6^* interpolation kernel. The results showed an insignificant improvement on the error level and the same rate of convergence as reported for M_4'. We relate this to the explicit regularization that effectively removes singularities at the solid interface before interpolation each time step.

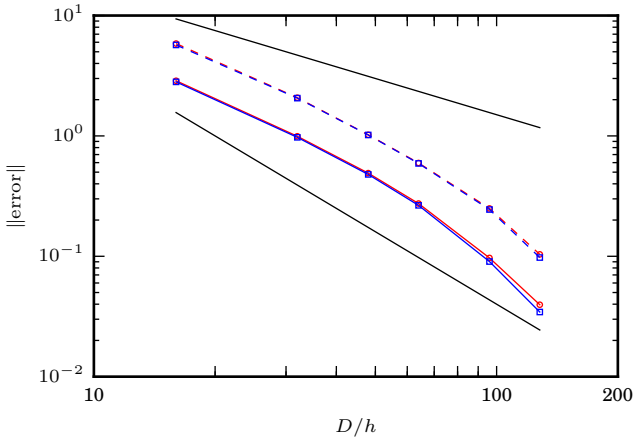

Figure 3.6: Convergence of the relative error on the drag coefficient for the impulsively started flow past a sphere at $\mathrm{Re} = 1000$ using the 3D iterative Brinkman method and a fixed time step of $\Delta t^* = 0.005$. The relative error is measured by comparing with the solution obtained using a spatial resolution of $h = D/128$ in the time interval $t^* \in [0, 5]$. L_∞-norm (—○—) and L_2-norm (- -○- -) using a second order approximation to Eq. (3.12). L_∞-norm (—□—) and L_2-norm (- -□- -) using a fourth order approximation to Eq. (3.12). Indication of respectively $\mathcal{O}(h^1)$ and $\mathcal{O}(h^2)$ convergence (——) .

Comparison of iterative and non-iterative scheme at early times

We compare the drag coefficient obtained using the iterative and the non-iterative scheme using $\eta = 1$ in Fig. 3.7(a). For the impulsively started flow past a sphere at the current Reynolds number there is no visible deviation between the two in the considered time interval.

The velocity residual at the end of the penalization step, for the iterative and the non-iterative scheme, is shown in Fig. 3.7(b). The L_2-norm of the residual obtained using the iterative scheme, requiring on average 30 iterations per time step to fulfill the convergence criteria, is approximately one order of magnitude lower than the norm obtained by the non-iterative scheme. This indicates that the iterative scheme enforces the solid boundary condition one order of magnitude more accurately than the non-iterative scheme. This is essentially the same as observed in 2D for the impulsively started flow past a cylinder at $\mathrm{Re} = 9500$ by Hejlesen et al. (2015a).

The rate at which the residual velocity within the solid at various time steps decays with the iteration number (N_i) has been plotted in Fig. 3.8. The variation has been measured for up to 1000 iterations at each of these time steps, hence exceeding the number of iterations needed to fulfill the aforementioned termination criteria. In this case, the asymptotic rate is close to -0.5 depending on which time step and norm is considered.

The additional cost of iterating the penalization vorticity relative to the cost of not iterating has been measured to be about 260 % at time $t^* = 0$. At this time the penalization subdomain constitutes about 40 % of the full domain. At time $t^* = 5.0$ the domain has expanded to encapsulate all vorticity with strength above the given threshold and consequently the penalization subdomain constitutes about 10 %. This reduces the relative additional cost of iterating to about 120 %. This indicates that for simulations with extensive wakes, where the penalization subdo-

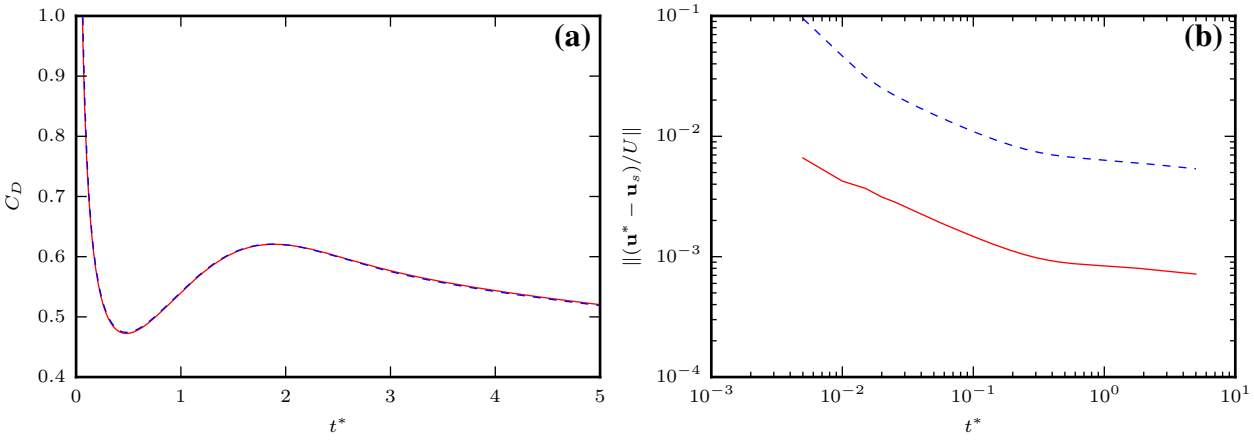

Figure 3.7: Impulsively started flow past a sphere at $\mathrm{Re} = 1000$ simulated using $h = D/128$ and $\Delta t^* = 0.005$. (a) Time variation of the drag coefficient for the iterative scheme (—) and the non-iterative scheme (- - -). (b) Time variation of the L_2-norm of the velocity residual for the iterative scheme (—) and the non-iterative scheme (- - -).

main may be small compared to the full domain, it is cheaper to reduce the velocity residual of the penalization by performing iterations rather than by reducing the global time step of the simulation.

Qualitative comparison of perturbed flow at later stages

Following Ploumhans et al. (2002) and Mimeau et al. (2016), we calculate the variation in time of the drag and lift coefficient in the interval $t^* \in [0, 20]$ having applied a perturbation to the free-stream velocity that breaks the axisymmetry

$$U_y = \begin{cases} 0.1 \sin\left(\pi(t^* - 3)\right) & \text{if } 3 < t^* < 4 \\ 0 & \text{else.} \end{cases} \tag{3.32}$$

Due to the perturbation a vortical structure is shed in the near wake from $t^* = 10$–14 forming a complex 3D wake. This shedding causes significant variations in the force coefficients as shown in Fig. 3.9(a).

The force coefficients are found in good qualitative agreement with the results of Ploumhans et al. (2002) and Mimeau et al. (2016) cf. Fig. 3.9(a). In the current simulation, the magnitudes of the obtained coefficients are slightly higher and the two extrema of the drag coefficient time history at $t^* \simeq 10.3$ and 13.3 are delayed as compared to Ploumhans et al. (2002), which is the same tendency seen in the results by Mimeau et al. (2016).

Ploumhans et al. (2002) further reported the maximum mesh Reynolds number ($\mathrm{Re}_{h\,\max} = \||\boldsymbol{\omega}|h^2/\nu\|_\infty$) as a diagnostic of the effective flow resolution in their simulation. The mesh Reynolds number in the present simulation is shown in Fig. 3.9(b). The figure shows that in present study the maximum mesh Reynolds number is at its maximum close to $t^* = 0$ due to the singularity occurring in the impulsively started flow. It rapidly decays to a value below 4 as the flow develops. Ploumhans et al. (2002) reported a maximum mesh Reynolds number increasing

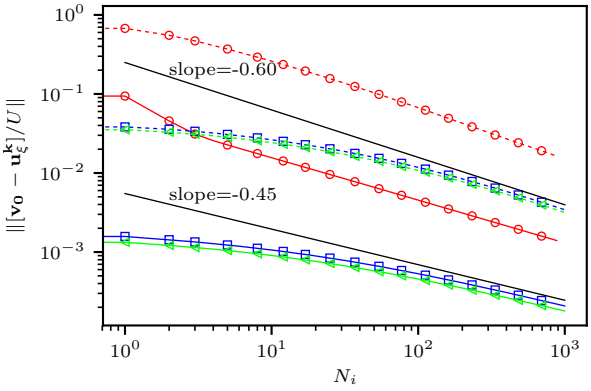

Figure 3.8: Impulsively started flow past a sphere at $\mathrm{Re} = 1000$ simulated using $h = D/128$ and $\Delta t^* = 0.005$. Decay of L_2-norm (solid lines) and L_∞-norm (dashed lines) of the velocity residual within the solid body as function of the iteration number (N_i) tested at time step 1 ($t^* = 0$) (⊖) , 200 ($t^* = 1.0$) (⊟) and 1000 ($t^* = 5.0$) (◁) .

from approximately 4 to 15–20 in their entire domain but approximately 3 in the boundary layer. The later is close to the present result since the grid resolution near the solid body is about the same.

It is reasonable to believe that the wake is better resolved in the present simulation as consequence of the uniform resolution. Ploumhans et al. (2002) used a reduced resolution in the far wake to gain computational efficiency.

The vortical structures of the flow may be identified from a rendering of the immediate vorticity magnitude at various times shown in Fig. 3.10. The structures observed at $t^* = 20$ in the present study appear more entangled than those reported by Ploumhans et al. Ploumhans et al. (2002). This may be due to a suppression of instabilities in the shed structure caused by the presumed coarser spatial resolution of the wake in that study.

The number of particles simulated increase from $\simeq 2 \times 10^6$ to $\simeq 7 \times 10^7$ in the current simulation, which is significantly more than the $\simeq 4.6 \times 10^5$ to $\simeq 2.3 \times 10^6$ particles that were used in the simulation by Ploumhans et al. (2002). The present simulation requires approximately 100 hours on 256 cores of the Intel Xeon E5640 processors.

3.4.2 Impulsively started flow normal to a disc at $\mathrm{Re} = 500$

The impulsively started flow normal to a circular disc at $\mathrm{Re} = 500$ is considered next. The setup is sketched in Fig. 3.11. The Reynolds number and non-dimensionless time, drag force we define respectively as

$$\mathrm{Re} = \frac{UD}{\nu}, \quad t^* = \frac{tU}{D}, \quad C_D = \frac{F_x}{\frac{1}{2}\rho U^2 D^2}, \tag{3.33}$$

where D is the diameter of the disc. The thickness of the disk is $B = D/16$. Again the second order explicit Runge-Kutta scheme is applied for the advancement of particles and the extent of the domain is updated as in the sphere simulation. Simulations were performed for spatial

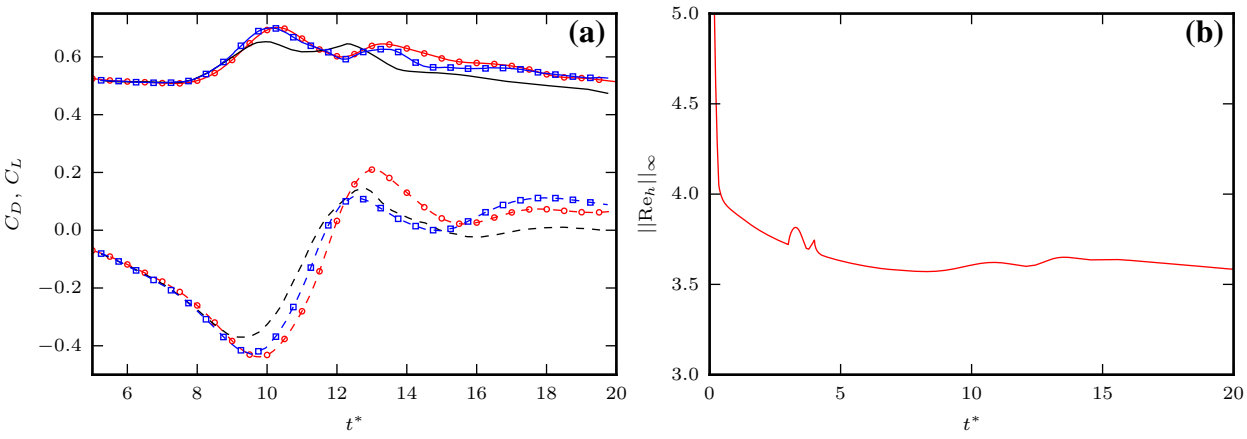

Figure 3.9: Time variation of simulations diagnostics in the impulsively started and perturbed flow past a sphere at $\mathrm{Re} = 1000$. (a): Drag coefficient (—○—) and lift coefficient (- -○- -) from present study. Drag coefficient (——) and lift coefficient (- - -) from Ploumhans et al. (2002). Drag coefficient (—□—) and lift coefficient (- -□- -) from Mimeau et al. (2016). (b) Time variation of the maximum mesh Reynolds number.

resolution $h = D/128$ and $h = D/256$ corresponding to a disc thickness of 8 cells and 16 cells respectively.

Comparison of iterative and non-iterative scheme

The drag coefficient obtained for the disc flow is, unlike the sphere flow, significantly affected by the choice of penalization scheme. The drag coefficients obtained from the iterative and the non-iterative scheme using $\eta = 1$ and $h = D/256$ are compared in Fig. 3.12(a). The figure shows that the iterative scheme match the reference well, when using a time step of $\Delta t^* = 0.001$. Using the same time step the non-iterative scheme significantly overestimates the drag coefficient for $t^* < 0.2$, since this scheme requires several time steps to impose the boundary conditions accurately on the surface of the disc. This scheme requires a time step of $\Delta t^* = 0.0001$ to match the reference solution.

As in the simulation of the flow past the sphere, the iterative method impose a visibly accurate boundary condition from the first time step depending on the spatial resolution. This may be seen from the isocontours of the axisymmetric stream function shown in Fig. 3.13. It was observed that results obtained for $h = D/256$ complied better with the reference results as compared to $h = D/128$ independent of global time step and penalization scheme. We relate this to the additional degrees of freedom within disc where the penalization vorticity may be non-zero and to the reduced smoothing of the boundary at the higher resolution.

In this case the maximum residual velocity for the non-iterative scheme is $\mathcal{O}(1)$ until $t^* = 0.1$–0.5 (not shown) whereas it is lower but still significant ($\mathcal{O}(0.1)$) for the iterative scheme (cf. Fig. 3.13) using the criteria $\varepsilon = 0.05$ which require approximately 30 iterations per time step for both spatial resolutions.

However it is noted that the L_2-norm of the residual for the iterative scheme is at any time less than 0.004 which is not the case for the non-iterative scheme until after approximately 1000

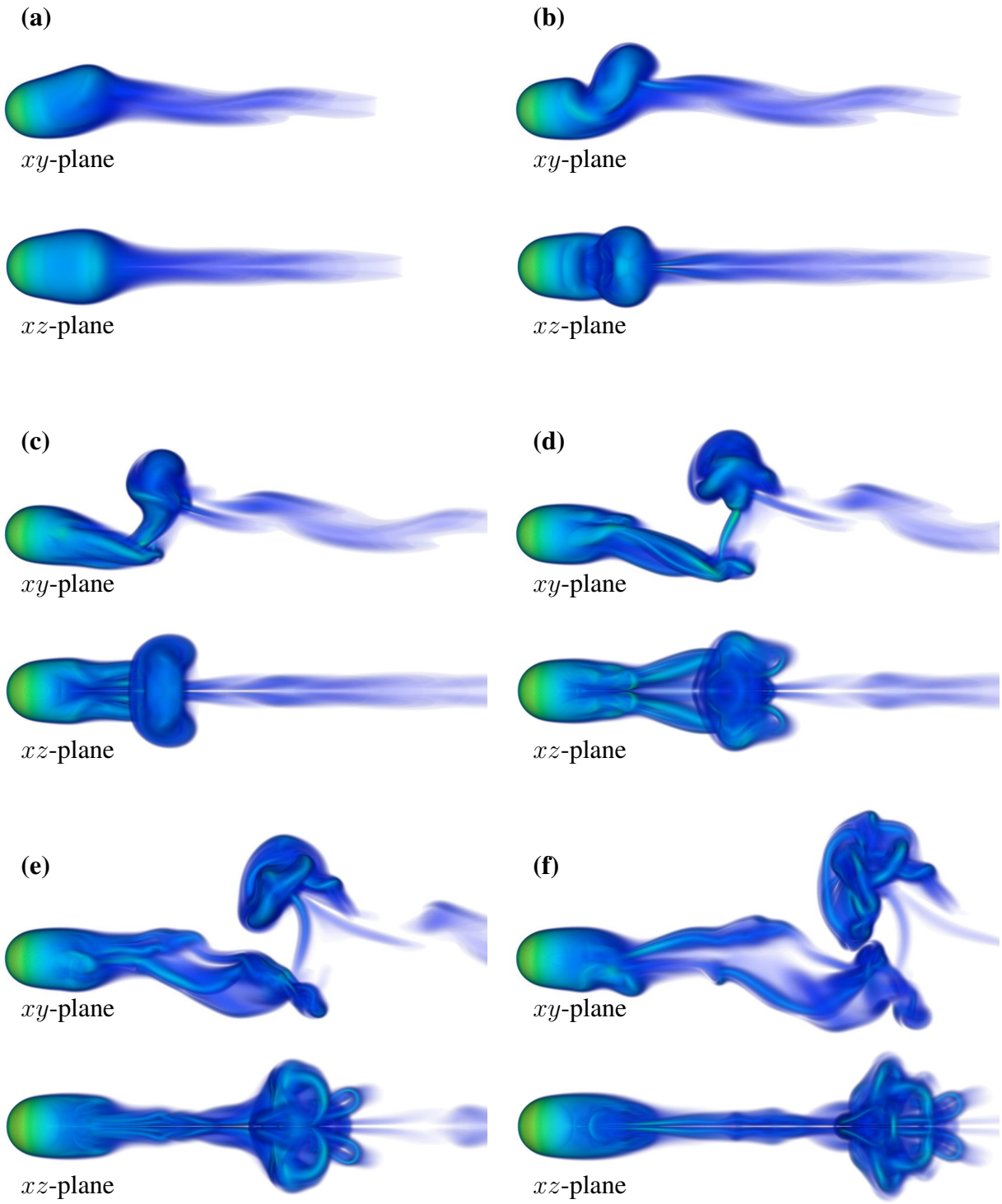

Figure 3.10: Visualization of vorticity intensity ($|\boldsymbol{\omega} D/U|$) at various times: (a) $t^* = 10$. (b) $t^* = 12$. (c) $t^* = 14$. (d) $t^* = 16$. (e) $t^* = 18$. (f) $t^* = 20$.

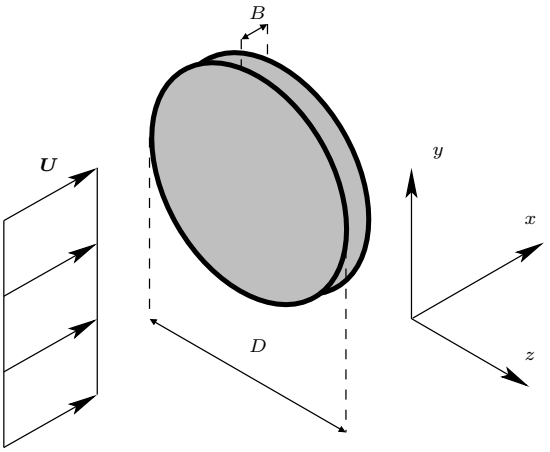

Figure 3.11: Impulsively started flow ($\boldsymbol{U}$) past a circular disc of finite thickness (B) and diameter (D). The origin of the Cartesian coordinate system is in the sketch displaced from its actual origin being at the center of the disc.

time steps at $t^* = 1$ when using a time-step of $\Delta t^* = 0.001$ as shown in Fig. 3.12(b).

It is observed that the maximum residual in the iterative scheme is located at the edges of the disc, where we see streamlines cross the solid boundary. The regularization applied when solving the Poisson equation ensures a smooth velocity field across the boundary, hence the edges of the solid is effectively rounded and one may expect a velocity residual here larger than elsewhere in the solid at any time. This area near the edge may be reduced by increasing the spatial resolution as may be seen in Fig. 3.14, which shows the isocontours of the axisymmetric stream function and the averaged velocity residual within the solid at time $t^* = 1.0$ for grid sizes $h = D/128$ and $h = D/256$.

Fig. 3.15 shows the rate at which the residual velocity within the solid decays with the iteration number (k). As for the impulsively started flow past the sphere, the asymptotic rate is around -0.5. The rate is steeper the first few iterations of the first time step because of the geometry in this case. So indeed it is possible to reduce the velocity level even further by increasing the number of iterations, but the rate at which the residual decays is slow.

3.4.3 Assessment of the need to modify the unbounded condition in truncated flow

Finally, we assess the necessity of modifying the unbounded boundary conditions for flows that are essentially not unbounded. This we do by considering a space-developing flow with wake truncation. In this case the flow with a free-stream velocity U past a sphere of diameter D and a Reynolds number of $\mathrm{Re} = 300$. It is simulated in a finite domain as sketched in Fig. 3.16 with the non-iterative penalization scheme, as the iterations cannot be performed separately in this case.

It may be argued that in order to ensure a physical behavior of the velocity field at the interface of the domain, inlet and outlet conditions are required (Cocle et al., 2008; Chatelain et al., 2013). For the bluff body flows considered in this project, the appropriate condition would be to impose the free-stream velocity U in the normal direction ($\boldsymbol{u} \cdot \boldsymbol{n} = U$, $\frac{\partial \boldsymbol{u}}{\partial n} \cdot \boldsymbol{t} = 0$)

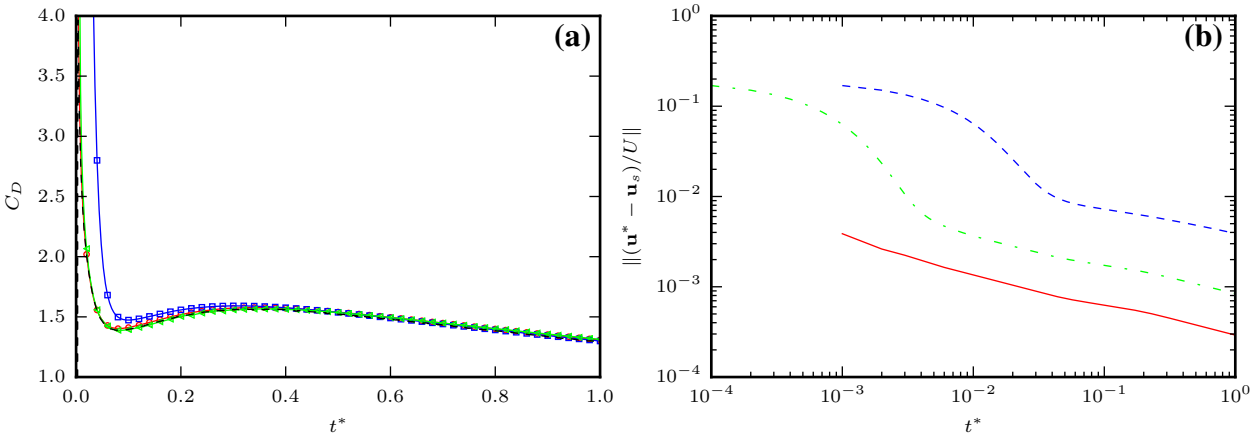

Figure 3.12: Impulsively started flow normal to disc at $\mathrm{Re} = 500$. (a) Drag coefficient obtained for the iterative scheme using $\Delta t^* = 0.001$ (—○—) . Drag coefficient obtained for the non-iterative scheme using $\Delta t^* = 0.001$ (—□—) and $\Delta t^* = 0.0001$ (—◁—) . Reference solution from a high resolution, axisymmetric simulation performed using a commercial finite-volume code (——) . (b) Time variation of the L_2-norm of the velocity residual. Iterative scheme using $\Delta t^* = 0.001$ (——) , non-iterative scheme using $\Delta t^* = 0.001$ (- - -) and $\Delta t^* = 0.0001$ (- · -) .

at the domain inlet, where vorticity is clipped e.g. in case of non-zero turbulent intensity in the oncoming flow, with a "through-flow" condition at the outlet. The later ensures that structures leave the domain in the normal direction ($\boldsymbol{u} \cdot \boldsymbol{t} = 0$, $\frac{\partial \boldsymbol{u}}{\partial n} \cdot \boldsymbol{n} = 0$).

The inlet condition is enforced by imposing the image

$$\boldsymbol{\omega}_n^- = \boldsymbol{\omega}_n^+, \quad \boldsymbol{\omega}_t^- = -\boldsymbol{\omega}_t^+. \tag{3.34}$$

Similarly the through-flow plane with zero tangential velocity is enforced by imposing the image

$$\boldsymbol{\omega}_n^- = -\boldsymbol{\omega}_n^+, \quad \boldsymbol{\omega}_t^- = \boldsymbol{\omega}_t^+. \tag{3.35}$$

As described in Sec. 1.2 the use of both an inlet and an outlet condition, implies that the Poisson equation should be solved, not only with the two images cf. Eqs. (3.34)–(3.35), but with an infinite array of images. This is efficiently computed using a periodic Green's function and a combination of DTTs for the convolution.

For various truncation lengths, solutions for entirely unbounded conditions are compared to solutions obtained with the inlet/outlet combination. A uniform mesh of spacing $h = D/64$ and a time-step adapted according to $C_{\mathrm{LCFL}} = 0.125$ is applied in all cases. With the Poisson solver a Gaussian kernel with $m = 10$ and $\alpha = 1.5$ is used. The Reynolds number and force coefficients are calculated as Eq. (3.27). Results in terms of force coefficients and Strouhal number ($\mathrm{St} = \frac{fD}{U}$) are given in Tab. 3.1. It may be seen that all results are quite similar and compares well with those found in the literature. The evolution of the force coefficients has been plotted in Fig. 3.17 for the unbounded and the bounded solution for the cases with $x_{\mathrm{outlet}} = 12D$.

The immediate vorticity every quarter period of single shedding cycle has been compared to that of Ploumhans et al. (2002) for the bounded simulation in Fig. 3.18–3.18. Also, an illustration of the 3D structures at $tU/D = 200$ is given in Fig 3.20.

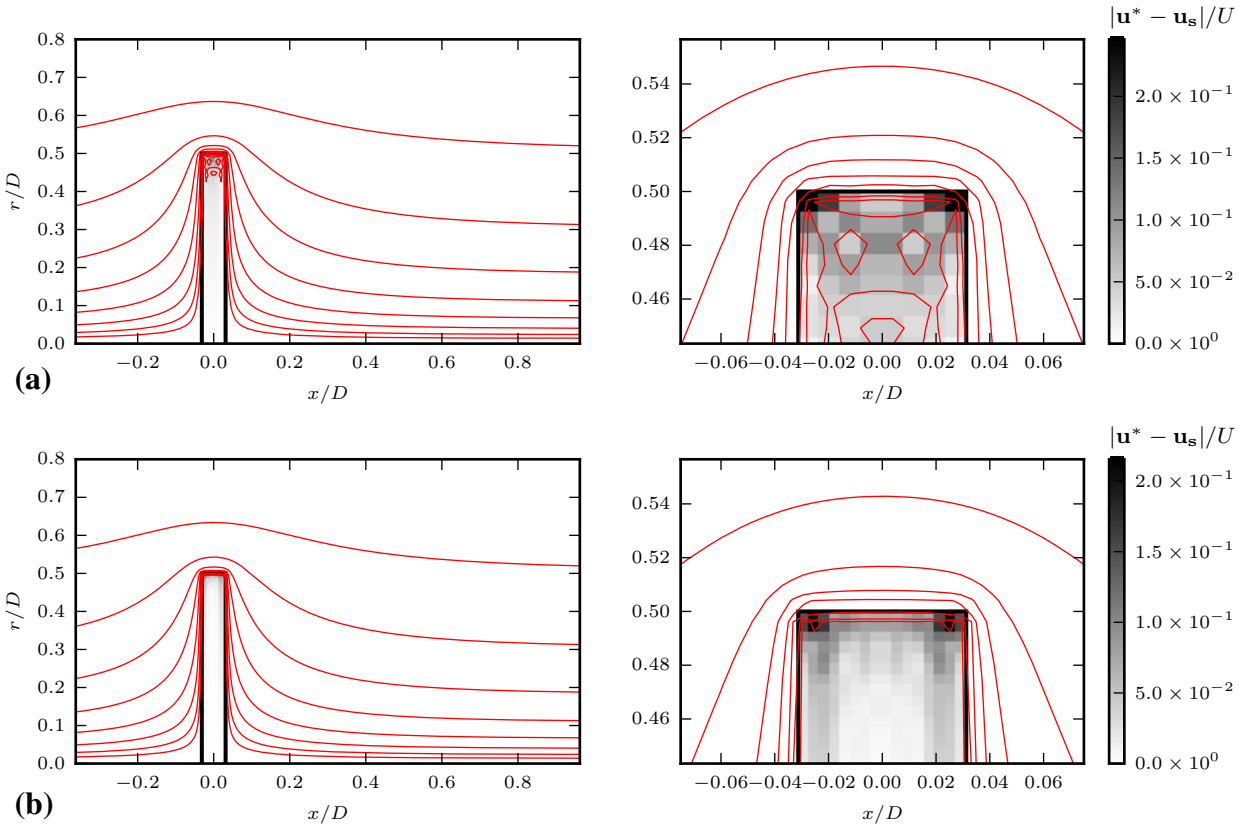

Figure 3.13: Impulsively started flow normal to disc at $\mathrm{Re} = 500$ at $t^* = 0^+$. Isocontours of the stream function in 10 logarithmically spaced levels in the interval $[-1, 1]$ (—) and indication of velocity residual within disc averaged in polar direction (grayscale). Zoom of the disc tip shows the maximum velocity residual is localized at the upstream edge, where streamlines may be seen to cross the interface. (a) Solution for spatial resolution $h = D/128$. (b) Solution for spatial resolution $h = D/256$.

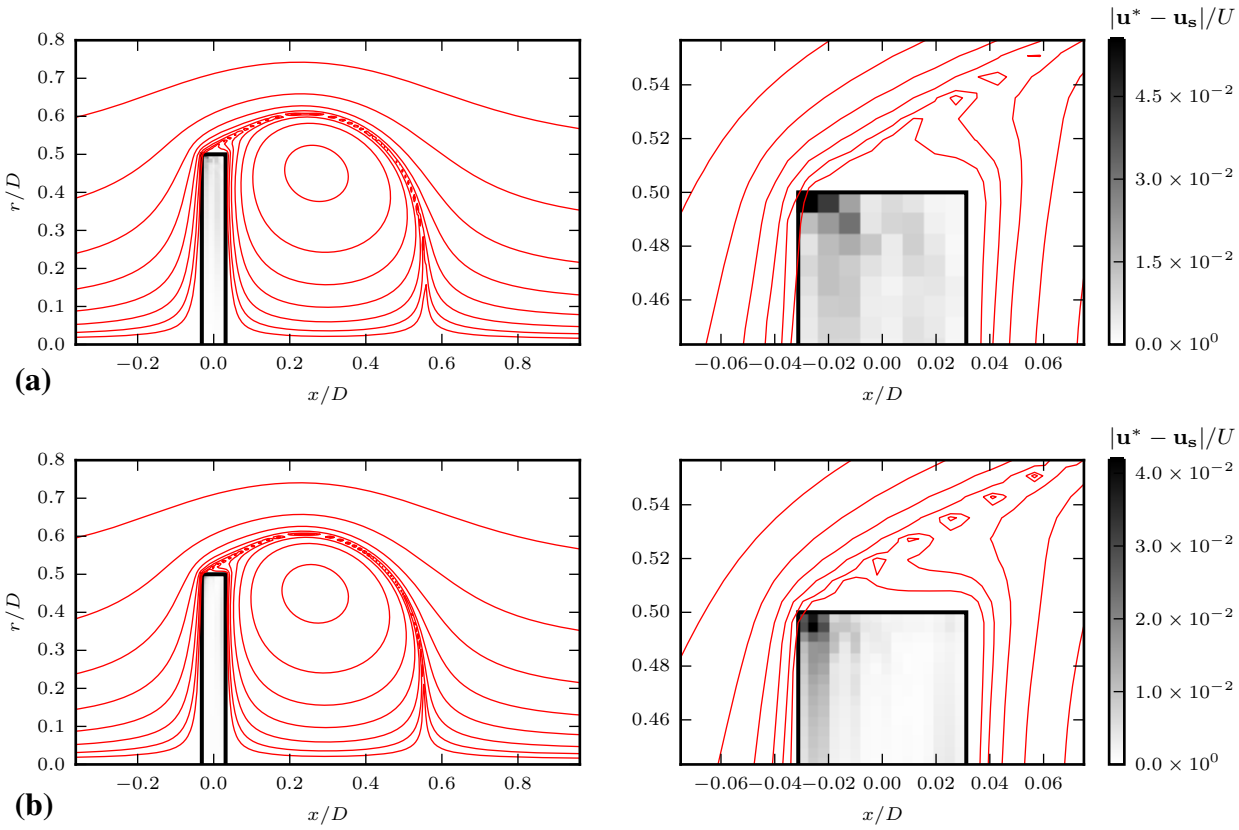

Figure 3.14: Impulsively started flow normal to disc at $\mathrm{Re} = 500$ at $t^* = 1$. Isocontours of the stream function in 10 logarithmically spaced levels in the interval $[-1, 1]$ (—) and indication of velocity residual within disc averaged in polar direction (grayscale). Zoom of the disc tip shows the maximum velocity residual is localized at the upstream edge, where streamlines may be seen to cross the interface. (a) Solution for spatial resolution $h = D/128$. (b) Solution for spatial resolution $h = D/256$.

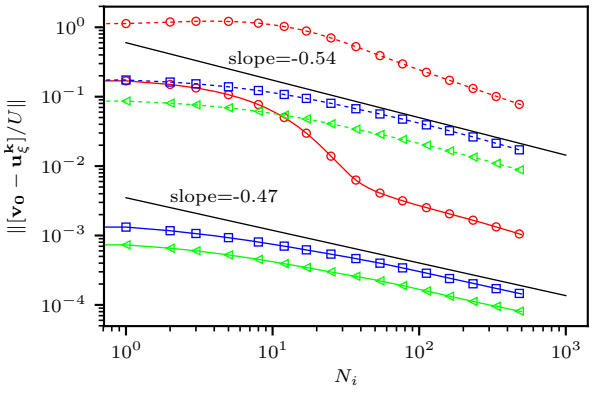

Figure 3.15: Impulsively started flow normal to a disc at $\mathrm{Re} = 500$ simulated using $h = D/256$ and $\Delta t^* = 0.001$. Decay of L_2-norm (solid lines) and L_∞-norm (dashed lines) of the velocity residual within the solid body as function of the iteration number (k) tested at time step 1 ($t^* = 0$) (—○—) 200 ($t^* = 0.2$) (—□—) and 1000 ($t^* = 1.0$) (—◁—)

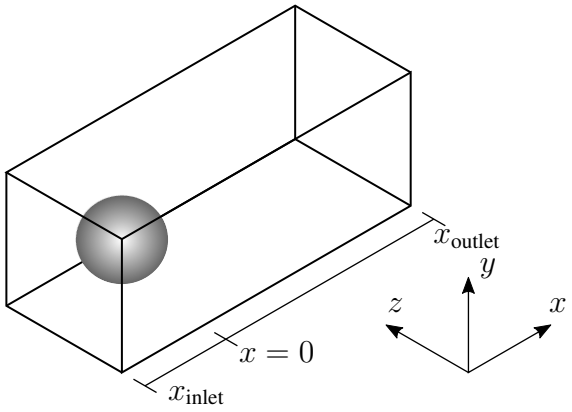

Figure 3.16: Sketch of the computational domain used to simulate the flow past a sphere at $\mathrm{Re} = 300$. The extent of the domain is fixed in the x-direction whereas it is adapted to the immediate vorticity field in the y, z-directions

The results imply that the simplified model using unbounded conditions give acceptable results for truncated bluff body flows. One explanation of this, is that the use of the regularized Green's functions ensures a smooth velocity field, even where vorticity is clipped.

Because the DTT method, which was used in this example, is not applicable to account for other images than those that are reflections of the mesh vorticity about the mesh boundaries, the vorticity splitting cf. Eq. (3.8) is not easily used with doubly bounded conditions. A doubly bounded direction used with the vorticity splitting would require constructing a doubly bounded Green's function by explicit summation (Cottet and Koumoutsakos, 2000; Hejlesen, 2016) when solving the Poisson equation on penalization subdomain. Alternatively, a contribution from a sum of shifted multipole expansions corresponding to the array of images, could be added to an unbounded solution, in a manner á la Kabadshow (2012) for the FMM method. The later would however greatly increase the complexity of the algorithm and has not been pursued.

3.5 Summary

A 3D iterative Brinkman method for accurate simulation of unsteady flows was presented. The work is based on the 2D method proposed by Hejlesen et al. (2015a).

The method was validated for the impulsively started flow past a sphere at $\mathrm{Re} = 1000$. The iterative scheme produces a vortex sheet at the first time-step of the simulation ($t^* = 0^+$) that agrees with the exact potential flow solution. At later stages the unsteady force coefficients obtained were found to be comparable to results obtained by Ploumhans et al. (2002) and Mimeau et al. (2016) using a boundary element method in a vortex particle method and vortex penalization method respectively.

The impulsively started flow normal to a circular disc of finite thickness at $\mathrm{Re} = 500$ was also considered and found to be a challenging problem for the Brinkman penalization method due to the geometry having the majority of its surface area orientated normal to the free-stream. This introduces a delay in the enforcement of the solid boundary condition for the non-iterative

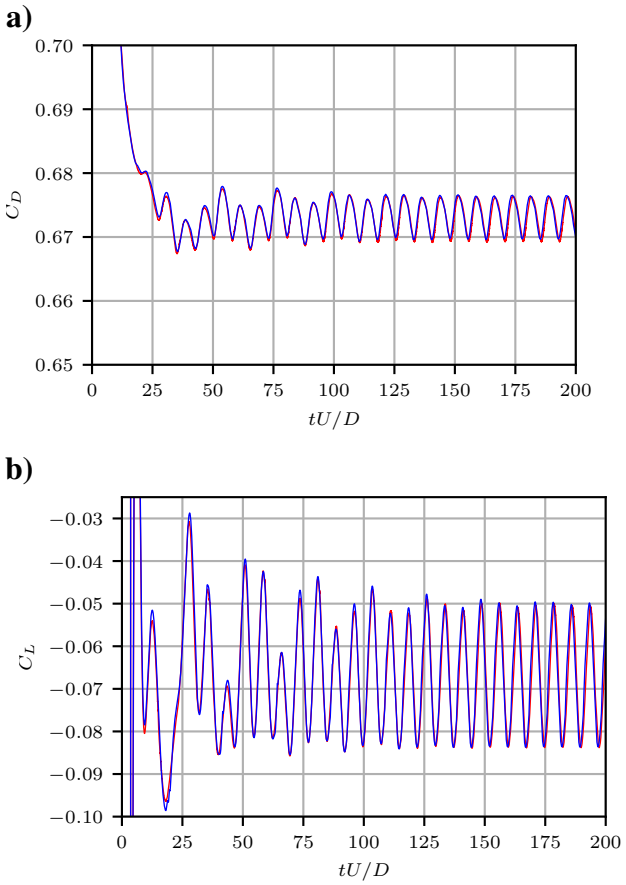

Figure 3.17: Time history of force coefficients for $x_{\text{outlet}} = 12$ with condition in x-direction as unbounded (—) inlet/outlet (—) (a) drag coefficient. (b) lift coefficient.

	x_{outlet}	$\bar{C}_D$	$\bar{C}_L$	ΔC_L	St
unbounded	$6D$	6.74×10^{-1}	-6.8×10^{-2}	1.8×10^{-2}	0.135
unbounded	$8D$	6.73×10^{-1}	-6.8×10^{-2}	1.7×10^{-2}	0.135
unbounded	$12D$	6.73×10^{-1}	-6.8×10^{-2}	1.8×10^{-2}	0.135
inlet/outlet	$6D$	6.73×10^{-1}	-6.7×10^{-2}	1.9×10^{-2}	0.135
inlet/outlet	$8D$	6.73×10^{-1}	-6.7×10^{-2}	2.0×10^{-2}	0.135
inlet/outlet	$12D$	6.73×10^{-1}	-6.7×10^{-2}	1.9×10^{-2}	0.135
Johnson and Patel (1999)	-	6.56×10^{-1}	-6.9×10^{-2}	1.6×10^{-3}	0.137
Mimeau et al. (2016)	-	6.73×10^{-1}	-6.6×10^{-2}	–	0.133
Ploumhans et al. (2002)	-	6.83×10^{-1}	-6.1×10^{-2}	1.4×10^{-2}	0.135
Tomboulides and Orszag (2000)	-	6.71×10^{-1}	–	–	0.136

Table 3.1: Results obtained for simulations with different boundary conditions in the x-direction and measured in the interval $tU/D \in [100; 200]$ in terms of mean force coefficients ($\bar{C}_D$, $\bar{C}_L$), lift coefficient oscillation amplitude ($\Delta C_L = \frac{1}{2}(C_{L\,\max} - C_{L\,\min})$) and dimensionless shedding frequency identified from the lift signal. Also results from the literature are presented.

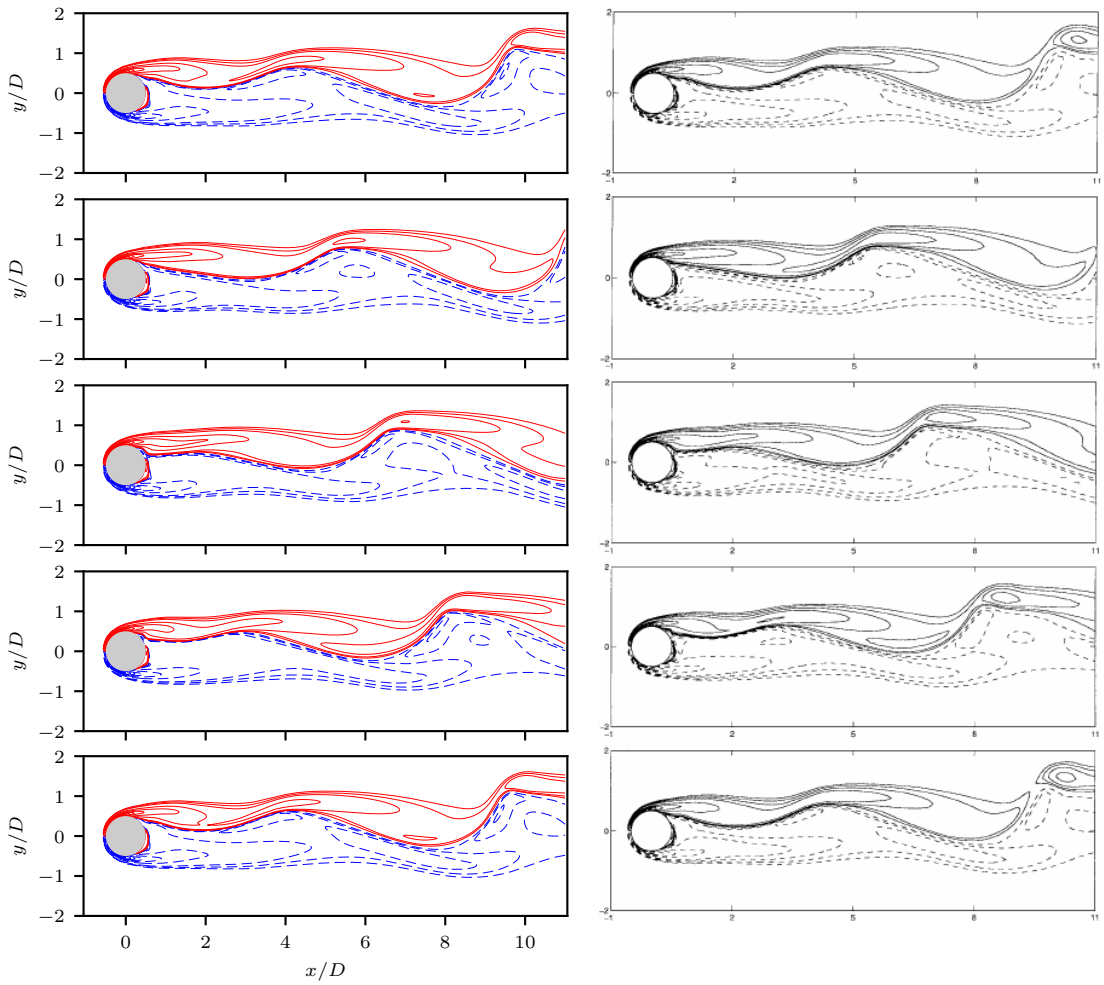

Figure 3.18: Isocontours of $\boldsymbol{\omega}_z$ in the xy-plane ($z = 0$) for the for flow past a sphere at $\mathrm{Re} = 300$ plotted every quarter period. Comparison between Ploumhans et al. (2002) (right) and present results (left). Levels are the same as in Ploumhans et al. (2002).

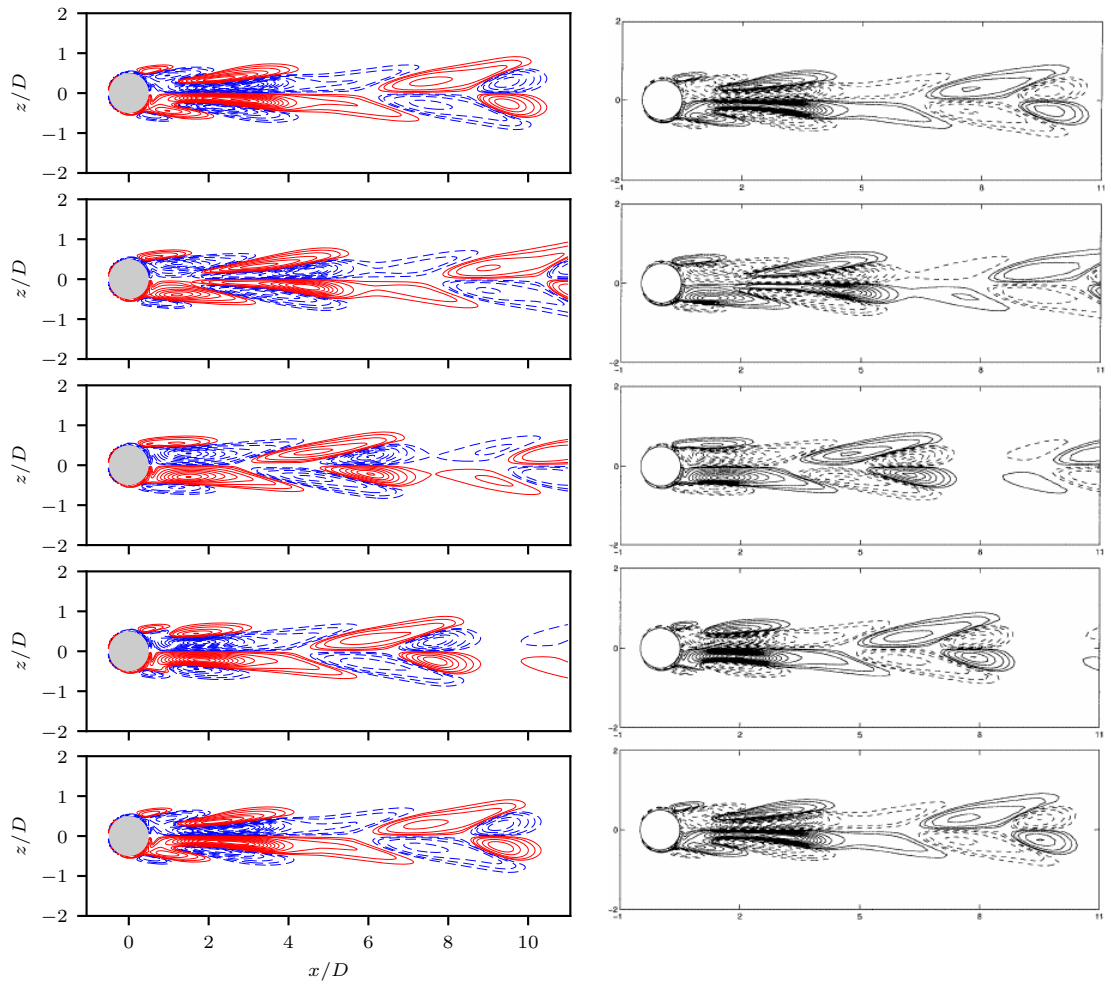

Figure 3.19: Isocontours of $\boldsymbol{\omega}_x$ in the xz-plane ($z = 0$) for the for flow past a sphere at $\mathrm{Re} = 300$ plotted every quarter period. Comparison between Ploumhans et al. (2002) (right) and present results (left). Levels are the same as in Ploumhans et al. (2002).

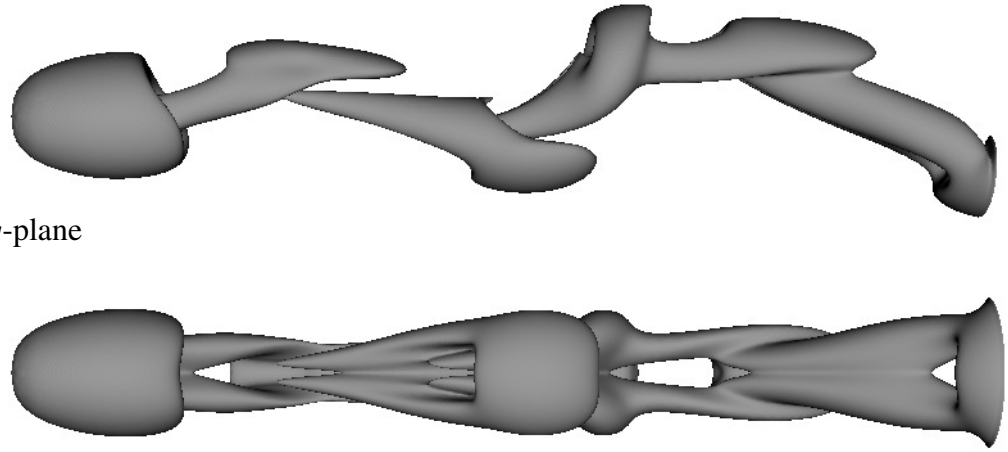

xy-plane

xz-plane

Figure 3.20: Instantaneous vorticity structures identified by the Q-criterion (Wray et al., 1988) at time $tU/D = 200$ for solution with $x_{\text{outlet}} = 12$ and inlet/outlet boundary conditions.

scheme. This is a consequence of the lack of global coupling otherwise imposed by the elliptic kinematic relation between vorticity and velocity. The iterative Brinkman method accounts for this and has been found to produce a time variation of the simulated drag coefficient in agreement with a reference solution using a time step that is five to ten times larger than what is required with the corresponding non-iterative scheme.

We note that at times away from the impulsive start the iterative and non-iterative solutions are comparable in the presented cases, thus the benefit of the iterative process on the solution is negligible at these time stages.

Chapter 4

Multiresolution

Parts of this chapter were prepared for a presentation at the ECCOMAS conference 2016 entitled "Simulation of bluff-body flows using iterative penalization in a multiresolution particle-mesh vortex method" (Spietz et al., 2016).

It is relatively simple to solve the Poisson equation (Eq. (1.1)) on a uniform grid using the Fourier based convolution approach with an appropriate Green's function and the technique by Hockney and Eastwood (1988). When the charge of the problem has a sparse spatial distribution in the computational domain, this procedure becomes expensive as all regions have to be resolved on the same uniform mesh. In this work we adopt a method based on a multilevel decomposition of the potential (or any derivative of it) using a hierarchy of nested uniform meshes to achieve local refinement.

4.1 Multilevel decomposition

A hierarchy of nested meshes is defined from a base mesh with spacing h_0, that spans the entire computational domain as sketched in Fig. 4.1. Each level (l) is associated with a set of particles and a uniform mesh with spacing

$$h_l = \frac{1}{2^l} h_0. \tag{4.1}$$

The solver is inspired by the particle-particle particle-mesh (P3M) approach by Hockney and Eastwood (1988), where the solution is separated into a short-range part computed directly from particle-particle interaction and a smooth long-range part computed on a uniform mesh using FFT. The P3M method was extended to the adaptive particle-particle particle-mesh (AP3M) by Couchman (1991). Here, the short-range part is further separated into a number of band-limited components dependent on the local resolution requirement. These are then solved for using a hierarchy of meshes to minimize the number of particles in the direct summation.

In this case a purely mesh-based computation of the potential (or any of derivative of it) is decomposed into a sum of band-pass filtered solutions, which are defined using a smoothing function (S)

$$\boldsymbol{\Psi} = \boldsymbol{\Psi}_0 + \sum_{l=1}^{l_{\max}} \boldsymbol{\Psi}'_l = \left(G_0 + \sum_{l=1}^{l_{\max}} G'_l \right) * \boldsymbol{\omega} \tag{4.2}$$

$$\text{with} \quad \widehat{G}_0 = \frac{\widehat{S}_0}{k^2} \quad \text{and} \quad \widehat{G}'_l = \frac{\widehat{S}_l - \widehat{S}_{l-1}}{k^2}. \tag{4.3}$$

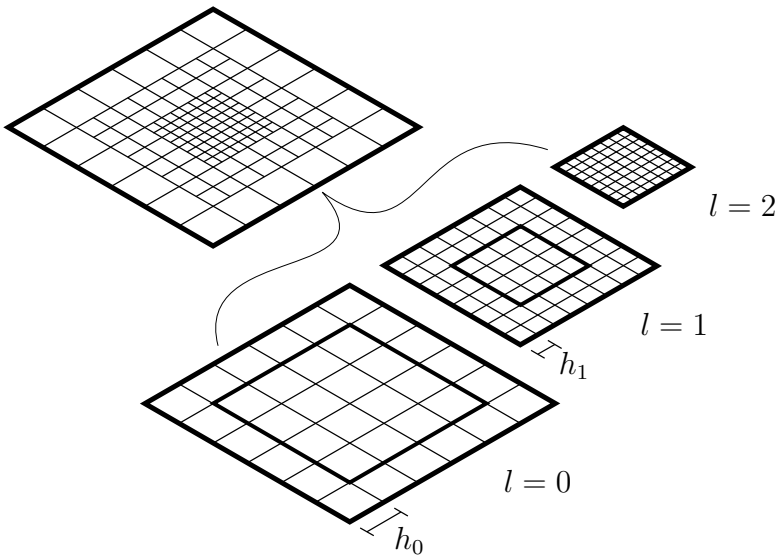

Figure 4.1: Mesh decomposition for local refinement.

G_l' is the Green's function for the band of scales between the two smoothing functions S_l and S_{l-1}. Following Hejlesen and Walther (2016) the smoothing functions are here taken as the high order, moment conserving filters (Eq. (1.23)) used to obtain regular solutions to the Poisson equation. Hence a *base level Green's function* and ($G_{0,m}$) *refinement Green's function* ($G'_{l,m}$) of order m are defined for mesh refinement by a factor of 2 as

$$\widehat{G}_{0,m} = \frac{\widehat{\zeta}_m(\sigma k)}{k^2} \quad \text{for} \quad \sigma = \alpha h_0, \tag{4.4}$$

$$\widehat{G}'_{l,m} = \frac{\widehat{\zeta}_m(\sigma k) - \widehat{\zeta}_m(2\sigma k)}{k^2} \quad \text{for} \quad \sigma = \alpha h_l. \tag{4.5}$$

Eqs. (4.4)–(4.5) may be used obtain solutions ($\mathbf{\Psi}'_l$) level-by-level from which the full solution may be reconstructed cf. Eq. (4.2). The advantages of this approach are:

1. The refinement Green's function (Eq. (4.5)) is compact, i.e. it has short-range; a point charge only induce a non-zero potential in a finite radius. This limited radius reduce the amount of zero-padding and overlap with other meshed required when obtaining a solution.

2. For the same reason far field conditions imposed by the method of images require only that the immediate neighbors are taken into consideration.

The 3D refinement Green's function for $m = 4$ and $\alpha = 1.0$ has been plotted in Fig. 4.2(a). The compactness of the refinement kernel depends on the normalization parameter α as shown in Fig. 4.2(b). A smaller α implies a faster decay of the real-space function. By choosing α too low, the real-space function may become underresolved when sampled on the mesh introducing alias errors, which are associated with a break down of the convergence rate as demonstrated in Hejlesen et al. (2015b). The optimal α is a compromise between accuracy and efficiency.

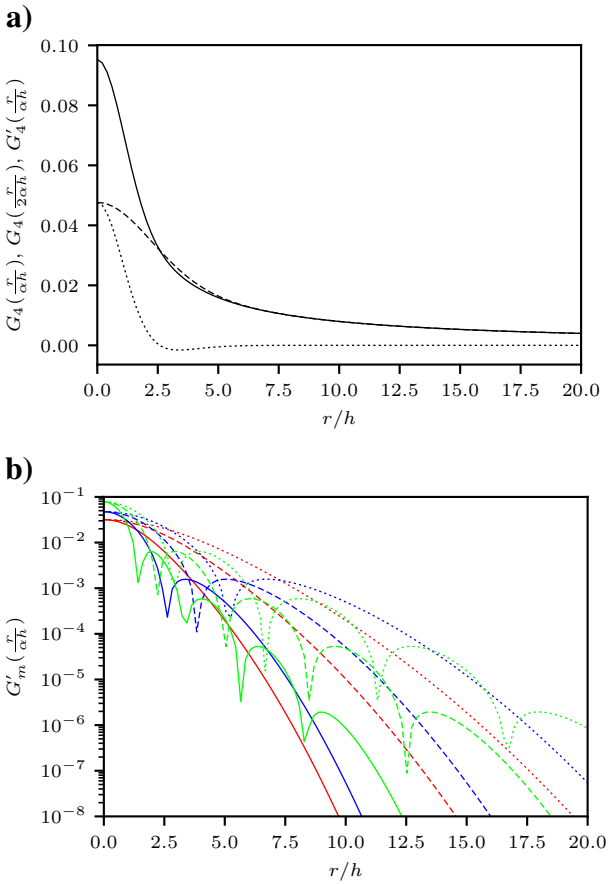

Figure 4.2: (a) Regularized free-space Green's functions for $m = 4$ and $\alpha = 1.0$: Regularization as $\sigma = \alpha h$ (—) , regularization as parent level $\sigma = 2\alpha h$ (- -) and the difference the two corresponding to the refinement Green's function (·····) . (b) Decay of various refinement functions $m = 2$ (—) , $m = 4$ (—) and $m = 10$ (—) for $\alpha = 1.0$ (—) , $\alpha = 1.5$ (- -) and $\alpha = 2.0$ (·····) .

4.2 Mesh-to-mesh interpolation between levels

The approach in practice implies that additional operators must be defined, to transfer data up and down in the mesh hierarchy. These add algorithmic complexity to the method and the properties of these operators affect the global accuracy of the method not only in transition regions between different meshes, but also in the interior regions.

A coarsening operator ($\mathcal{D}$) is required

$$\boldsymbol{\omega}_{l-1} \approx \mathcal{D}_{l\to l-1}\left\{\boldsymbol{\omega}_l\right\}, \tag{4.6}$$

to take a mesh field (the right-hand-side of the Poisson equation i.e. the vorticity) from level l to $l-1$ as the vorticity will be evolved on the finest mesh available at any given spatial location but is needed also on the lower levels, when solving the Poisson equation.

Similarly, when reconstructing the full (regularized) potential at level $l > 0$ cf. Eq. (4.2) a lifting operator ($\mathcal{U}$) is required

$$\boldsymbol{\Psi}_l = \boldsymbol{\Psi}_0 + \sum_{i=1}^{l} \boldsymbol{\Psi}'_i \approx \mathcal{U}_{l\to l+1}\left\{\boldsymbol{\Psi}_{l-1}\right\} + \boldsymbol{\Psi}'_l. \tag{4.7}$$

The process of mesh field coarsening is a two step operation consisting of (1) low-pass filtering the input sequence and (2) down-sampling the filtered sequence at a reduced rate. Low-pass filtering before sample rate reduction is required to suppress aliasing (Crochiere and Rabiner, 1981). Similarly, when up-sampling a sequence, images of the Fourier coefficients due to the periodicity of these, will be present in the output sequence (Crochiere and Rabiner, 1981). Subsequent, low-pass-filtering is required to supress imaging.

The ideal discrete low-pass filter is not compact in real-space and hence impractical to use to achieve local refinement. In stead the interpolation filters also used for particle-mesh interpolation (Eqs. (2.10)–(2.12)) are considered in the current work. These are compact (in real-space) approximations to the ideal discrete low-pass filter with spectra shown in Fig. (2.2)(b). The degree of smoothness i.e. the number of continuous derivatives of the real-space function determines how fast the Fourier coefficients decay. The lack of flatness of the Fourier coefficients within the band-pass region can be amended for by including the additional smoothing in the refinement operator using the Fourier transform of the discrete interpolation functions as

$$\widehat{G}'_{l,m} = \frac{\widehat{\zeta}_m(\sigma k) - \sum_{\boldsymbol{n}} \widehat{W}(2\boldsymbol{k}_{\boldsymbol{n}})^2 \widehat{\zeta}_m(2\sigma k)}{k^2} \tag{4.8}$$

$$\text{for} \quad \sigma = \alpha h_l, \quad \boldsymbol{k}_{\boldsymbol{n}} = \boldsymbol{k} + \boldsymbol{n} 2\pi / h_l, \quad \boldsymbol{n} \in \mathbb{Z}^3. \tag{4.9}$$

Although the modal-coupling imposed by down-sampling and up-sampling (aliasing and imaging) does not imply a loss of information, it is not simple to amend for these errors e.g. by modifying G'. For the summation in Eq. (4.8) only indices $\boldsymbol{n} = [-1, 0, 1]^3$ are included as the imaging and aliasing error were observed to dominate for high order interpolation.

4.3 Convergence test of the multilevel Poisson solver in 1D

Using $m = 4$ and $\alpha = 1.0$ for the Gaussian functions cf. Eq. (1.23) in Eq. (4.8) for multilevel decomposition and 6 ghost cells, the unbounded Poisson equation is solved for the right hand

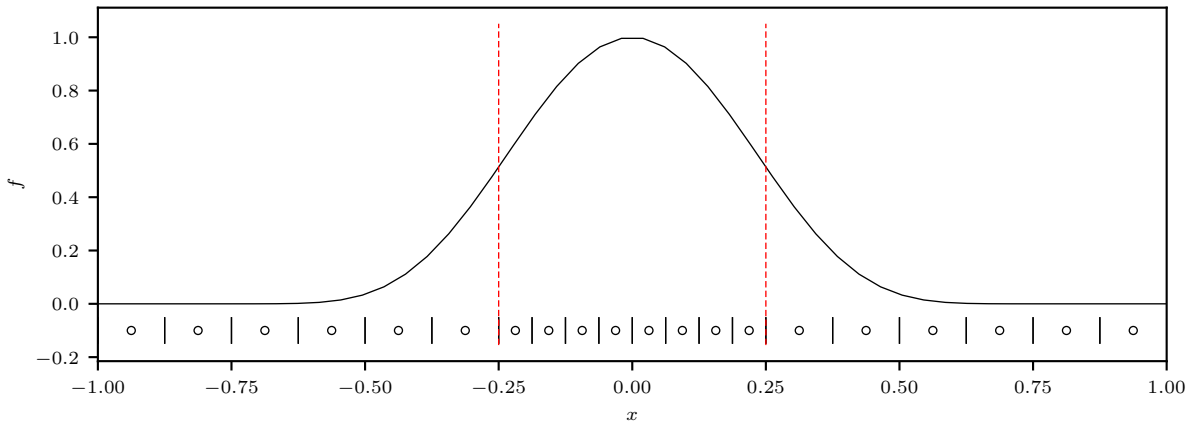

Figure 4.3: Setup for convergence test in 1D: The test function f (—) and also indication of a multiresolution mesh with cell centers (○) . Vertical lines (- - -) indicate the interface between mesh levels.

side constructed from the test function

$$u_{\text{ana}}(x) = \begin{cases} \exp\left(c\left[1 - \frac{1}{1-x^2}\right]\right) & \text{for} \quad |x| < 1 \\ \\ 0 & \text{for} \quad |x| \geq 1. \end{cases} \tag{4.10}$$

as $f = -\nabla^2 u_{\text{ana}}$. The right-hand-side has been plotted in Fig. 4.3 with an indication of a multiresolution mesh. The L_2-norm of the error

$$\text{error}(x) = u(x) - u_{\text{ana}}(x) \tag{4.11}$$

is plotted in Fig. 4.4. The convergence of the error is restricted to $\mathcal{O}(h^2)$, $\mathcal{O}(h^3)$, $\mathcal{O}(h^4)$ for interpolation by M_2, M_4' and M_6^* respectively. The distribution of the error for the coarsest mesh considered has been plotted in Fig. 4.5 for interpolation using the three different functions. It is notable to observe that the error does not go to zero away from the center of the f distribution, which is significant for the lower order interpolation. This is because the zero moment is not exactly conserved, when re-sampling f by down-sampling. This is also discussed in the next section. For M_2 this error dominates, whereas for M_4' a smooth oscillating error in the coarse regions is also significant, which is related to the regularization. A high frequency error is observed in the refinement region due to mesh-to-mesh interpolation. If the M_6^* function is used the high frequency error from aliasing and imaging decay with the same rate as the filter function ($m = 4$), and is not dominating.

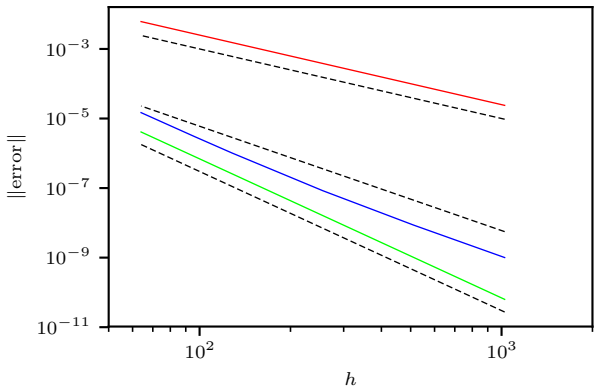

Figure 4.4: L_2-norm of error for the multilevel poisson solver with $m = 4$ and $\alpha = 1.0$ and M_2 interpolation (—) M_4' interpolation (—) M_6^* interpolation (—) . Also indicated order of convergence from top to bottom: $\mathcal{O}(h^2)$, $\mathcal{O}(h^3)$, $\mathcal{O}(h^4)$ (- - -)

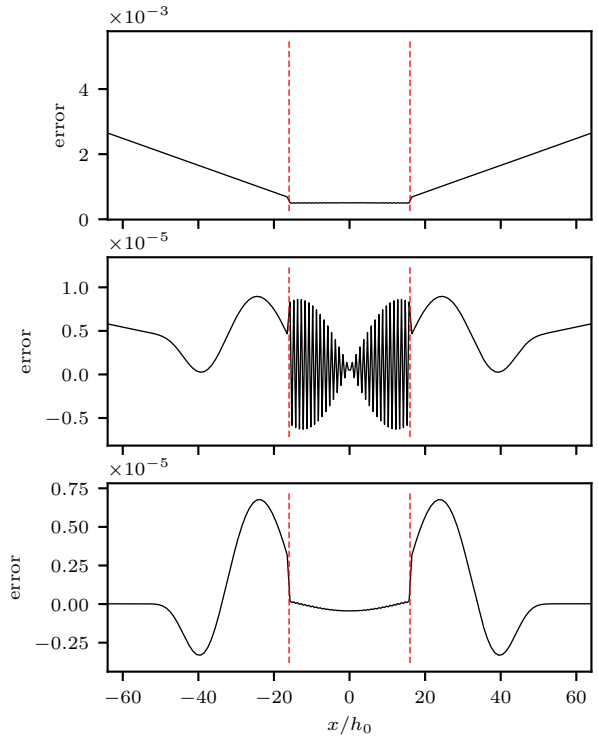

Figure 4.5: Multilevel poisson solver for $m = 4$ and $\alpha = 1.0$ and mesh-to-mesh interpolation with M_2 (top), M_4' (middle), M_6^* (bottom). Vertical lines indicate the interface between mesh levels.

4.4 Multilevel particle-strength redistribution

A multiresolution particle-method also requires a particle-strength redistribution scheme, which is explained using the same two level example as for the Poisson convergence test. A combined set of particles representing the two mesh levels has been illustrated in Fig. 4.6(a). Redistribution of the particle-strength onto the non-uniform grid is done in two steps:

1. Level wise, the strength of particles and ghosts particles whose volume correspond to the cell volume on the mesh at the current level, is redistributed onto interior- and ghost cells using classic particle-mesh interpolation with the M_4' kernel, as illustrated in Fig. 4.6(b).

2. The ghost layers are populated by mesh-to-mesh interpolation by coarsening and lifting of the vorticity at higher- and lower levels respectively as illustrated in Fig. 4.6(c). Ghost particles are created by re-meshing the ghost regions at the first stage of every time step, for consistent particle-mesh interpolation at the subsequent stages and at the first stage of the following time-step. In order to transfer correctly a particle from one level to another, the ghost region must have a certain width relative to size of the time-step, which impose a CFL like condition (we refer readers to Rasmussen et al. (2011) for further details).

It should be noted that this redistribution scheme favors smoothness of the interpolated fields over exact moment-conservation as the overlapping interpolation is not conservative at the interfaces. This could be improved by correcting the stencil of the discrete interpolation operator near the interface as done by Rossinelli et al. (2011) for average interpolation wavelets. However, the operators considered here are wider than those used with wavelet adapted multiresolution, which makes the correction quite complex. This has not been studied further, as exact momentum-conservation would also involve the correction of vorticity-fluxes.

We test the error on the redistribution of the particle set and on the derivatives of the redistributed variables approximated with fourth order centered finite-differences. The particles-strengths are obtained from the test function Eq. (4.10). The error on the mesh field and its two first derivatives with respect two the analytic solution have been plotted on Fig. 4.6. It may be seen that the mesh-to-mesh interpolation scheme produce an additional error in the ghost regions. This error may be reduced by applying a scheme based on mesh-to-mesh interpolation with M_6^* when using M_4' for particle-mesh interpolation on the individual levels, but this has small effect on the error of the derivatives. It is observed that the error on the derivatives computed from the redistributed field converge with mesh refinement, but at a reduced rate as compared to $\mathcal{O}(h^3)$. As seen in Fig. 4.8 for this problem the rate is $\mathcal{O}(h^{2.5})$ and $\mathcal{O}(h^{1.5})$ for the first and second derivative respectively when using mesh-to-mesh interpolation with M_4' and M_6^* and $\mathcal{O}(h^{1.5})$ and $\mathcal{O}(h^{0.5})$ when using mesh-to-mesh interpolation with M_2. Redistribution is in the following carried out using M_4' for both particle-mesh interpolation and mesh-mesh interpolation.

4.5 Remarks on the implementation

The proposed method is implemented for predefined local refinement and time marching is done using a global time-step for simplicity.

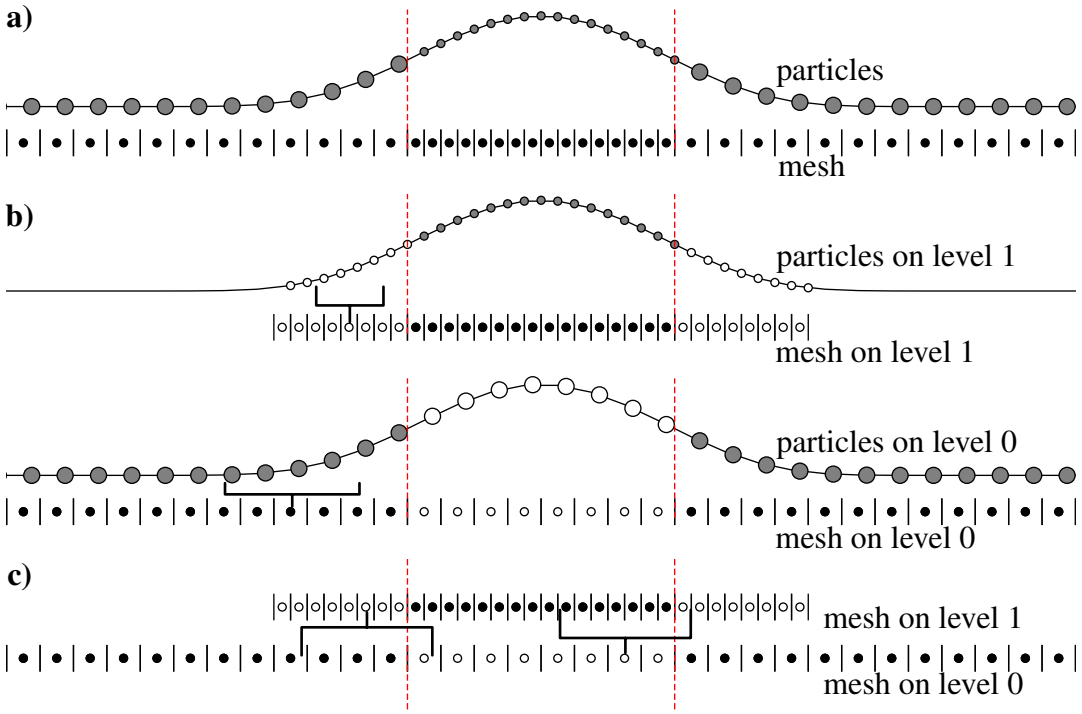

Figure 4.6: Redistribution of particle strength onto a mesh with a single refinement region. The unfilled markers represent ghost particles or ghost mesh points. (a) The combined mesh and set of particles for both levels (excluding ghost particles and ghost cells). (b) Level wise particle redistribution on meshes. (c) Mesh-to-mesh interpolation to populate mesh points in ghost regions. Ghost particles are subsequently created by re-meshing of the ghost regions.

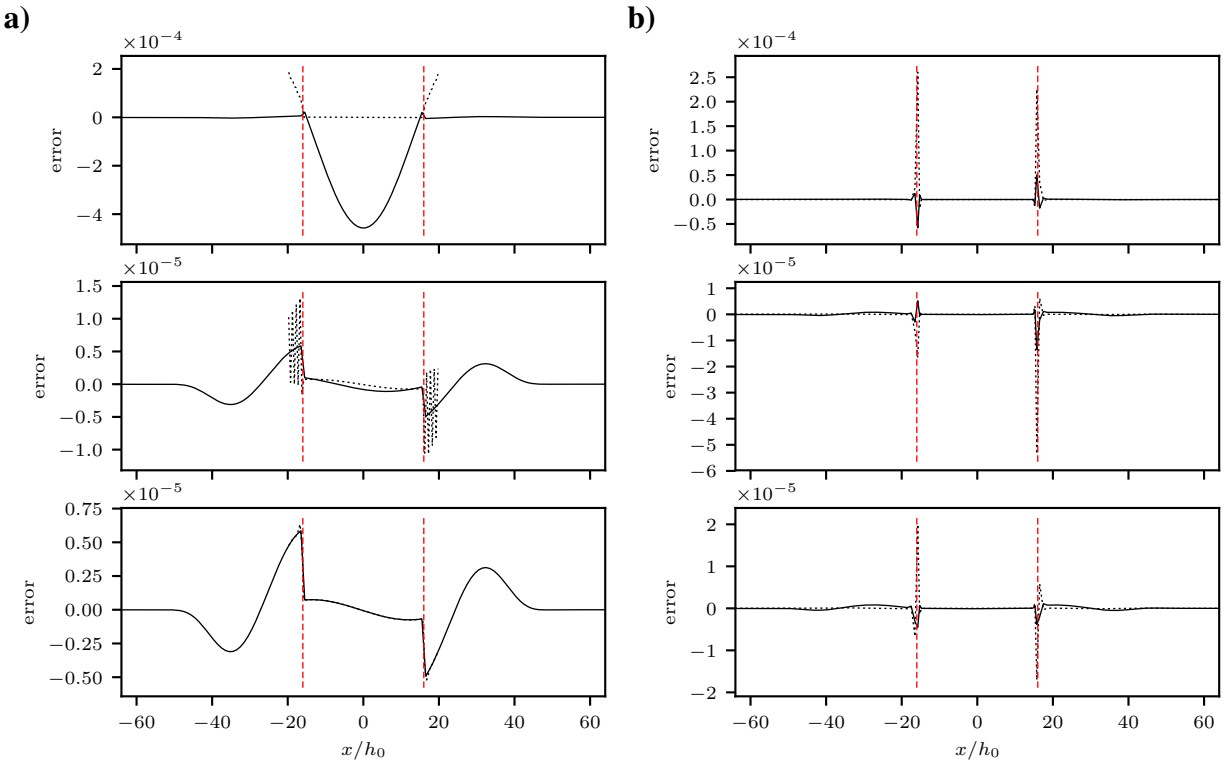

Figure 4.7: (a) Redistribution error, $\text{error} = u - u_{\text{ana}}$ on mesh (interior and ghosts cells): $l = 0$ (—) $l = 1$ (·····) . (b) Error on derivatives on mesh (interior only): $\text{error} = \left(\frac{\mathrm{d}u}{dx} - \frac{\mathrm{d}u}{dx}|_{\text{ana}}\right) h$ (—) and $\text{error} = \left(\frac{\mathrm{d}^2u}{dx^2} - \frac{\mathrm{d}^2u}{dx^2}|_{\text{ana}}\right) h^2$ (·····) From top to bottom mesh-to-mesh interpolation by M_2, M_4' and M_6^*. Vertical lines indicate the interface between mesh levels.

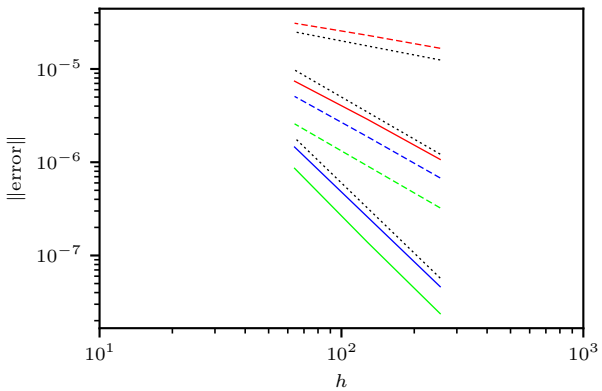

Figure 4.8: L_2-norm of the error on multilevel redistribution with M_4^* used for particle to mesh interpolation and mesh-to-mesh interpolation by M_2 (—), M_4' (—) M_6^* (—). Line types indicate: Error on first order derivative (—), error on the second order derivative (- -) and order of convergence from top to bottom as $\mathcal{O}(h^{0.5})$, $\mathcal{O}(h^{1.5})$, $\mathcal{O}(h^{2.5})$ (·····) .

The procedure is implemented by level wise applying the single level parallel solution procedure; all processes contain a single subdomain of each mesh on every level (a patch). Subdomains belonging to a single processor are not neccesarily overlapping. This hinters patches from being arbitrarily small and sparsely distributed over the computational domain. Further, the communication overhead when interpolating mesh fields between levels may be high for this reason. An efficient parallel decomposition as a block-structured multilevel mesh layout, as commonly used with adaptive mesh refinement (AMR) (Berger and Colella, 1989), would be an obvious improvement of the method. This would allow local adaptivity, as smaller mesh-blocks can dynamically be selected for refinement or coarsening. Further, it would allow preservation of the data for interpolation on the same processor, thereby minimizing inter-processor communication. By taking advantage of the compactness of the refinement kernel, the Poisson equation may further be solved sequentially for each subdomain on levels $l > 0$. This is practical if the overlap can be kept at 4-6 cells, especially when taken into consideration, that the global data mapping associated with the FFT convolution will no longer be required. We note that such parallel implementations for particle dynamics already exist e.g. ENZO by Bryan and et. al (2014). An adaptation of the current method into such framework would indeed be possible (see a similar solver for cosmology simulations by Passy and Bryan (2014)).

4.6 Verification of the combined procedure

To test the combined procedure of multilevel Poisson solver and multilevel redistribution of particle vorticity we consider the Taylor-Green Vortex in a triple-periodic cuboid domain of side length L with initial condition as

$$\omega_x = -\frac{2\pi}{L} U \cos\left(\frac{2\pi}{L}x\right) \sin\left(\frac{2\pi}{L}y\right) \sin\left(\frac{2\pi}{L}z\right) \tag{4.12}$$

$$\omega_y = -\frac{2\pi}{L} U \sin\left(\frac{2\pi}{L}x\right) \cos\left(\frac{2\pi}{L}y\right) \sin\left(\frac{2\pi}{L}z\right) \tag{4.13}$$

$$\omega_z = \frac{4\pi}{L} U \sin\left(\frac{2\pi}{L}x\right) \sin\left(\frac{2\pi}{L}y\right) \cos\left(\frac{2\pi}{L}z\right). \tag{4.14}$$

We use length scale $\frac{L}{2\pi}$ and velocity scale U to define a Reynolds number as

$$\mathrm{Re} = \frac{U\frac{L}{2\pi}}{\nu}. \tag{4.15}$$

The evolution of the initial condition cf. Eq. (4.12) is simulated for $\mathrm{Re} = 200$ in a single resolution setup with mesh spacing $h/L = 96$ and a setup with single refinement level such that $h_0/L = 96$, $h_1/L = 192$, where the refinement is located as indicated Fig. 4.9. For comparison both simulations are performed using Gaussian regularization functions for $m = 4$ and $\alpha = 1.0$ with the Poisson solver and third order Runge-Kutta time-step scheme with time-step size adapted with $C_{\mathrm{LCFL}} = 0.125$. The overlap region on the refinement patch is 6 cells wide, which has been found sufficient in 3D.

The large scale initial condition develops into smaller scales localized on two parallel planes (see Fig. 4.9). The evolution is associated with an increase in the enstrophy (not shown) and an

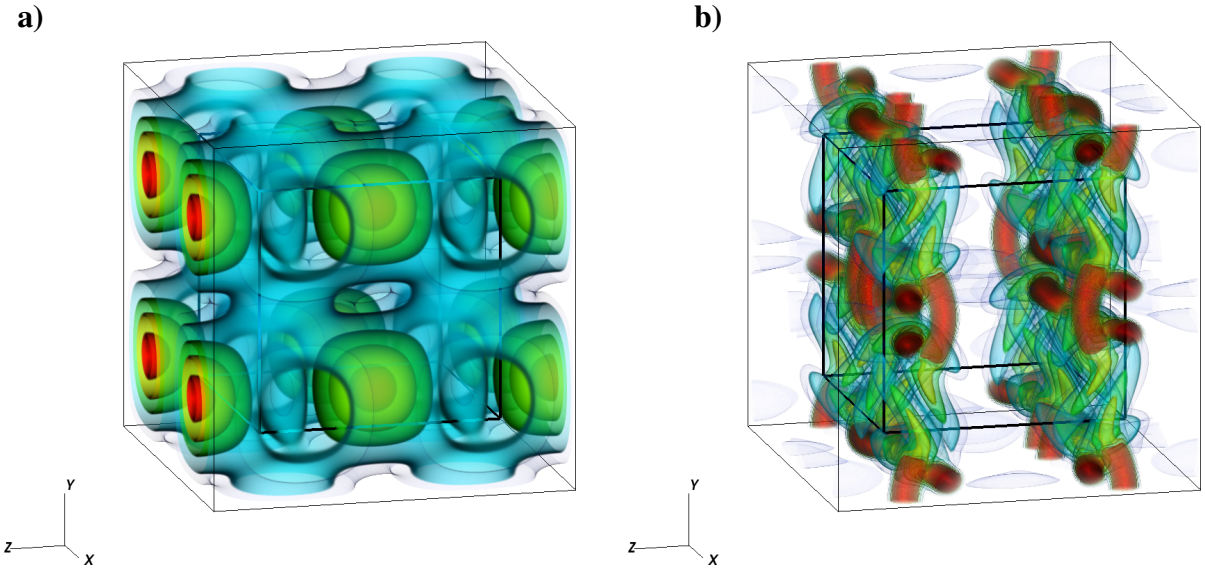

Figure 4.9: Instantaneous vorticity magnitude obtain from multiresolution simulation of Taylor Green Vortex at $\mathrm{Re} = 200$ with refinement region indicated as the box in the center of the domain. (a) $|\boldsymbol{\omega}|U/L \in [2; 12]$ (from blue to red) at $tU/L = 0.0$ (b) $|\boldsymbol{\omega}|U/L \in [8; 32]$ (from blue to red) at $tU/L = 6.3$

increased rate of dissipation of kinetic energy (E). The two shear layers intersect the refinement region, hence the simulation should be sensitive to errors on the interfaces. It is seen from Fig. 4.10(a) that the multiresolution simulation produces a solution that compares equally well with the reference solution by Brachet et al. (1983) as the single resolution does in terms of rate of change of the kinetic energy.

A measure of numerical dissipation may be obtained by comparing the theoretical viscosity to the mean simulated viscosity defined as (Saffman, 1992)

$$\nu_{\text{eff}} = -\frac{1}{\mathcal{E}}\frac{dE}{dt}, \tag{4.16}$$

where Ω is the enstrophy ($\mathcal{E} = \int \boldsymbol{\omega} \times \boldsymbol{\omega}\, \mathrm{d}V$).

From Fig. 4.10(b) it is seen that the multiresolution setup results in numerical dissipation that is slightly higher but around the same magnitude (0–1%) as for a single resolution level.

Note that vorticity is re-projected onto a divergence-free field every 5$^{\text{th}}$ time-step which is reflected as an oscillating behavior of the simulation diagnostics, especially the effective viscosity. Also, the numerical dissipation is at times negative, which may be related to the energy being computed from filtered velocities and therefore it is underestimated relative to the enstrophy.

4.7 Multiresolution simulation of the flow past a circular cylinder at $\mathrm{Re} = 400$

The circular cylinder is a challenging flow to simulate even at relatively low Reynolds numbers with a VPM method. An accurate prediction of the separation point requires a well resolved interface, especially using the Brinkman penalization technique because of the mollification ef-

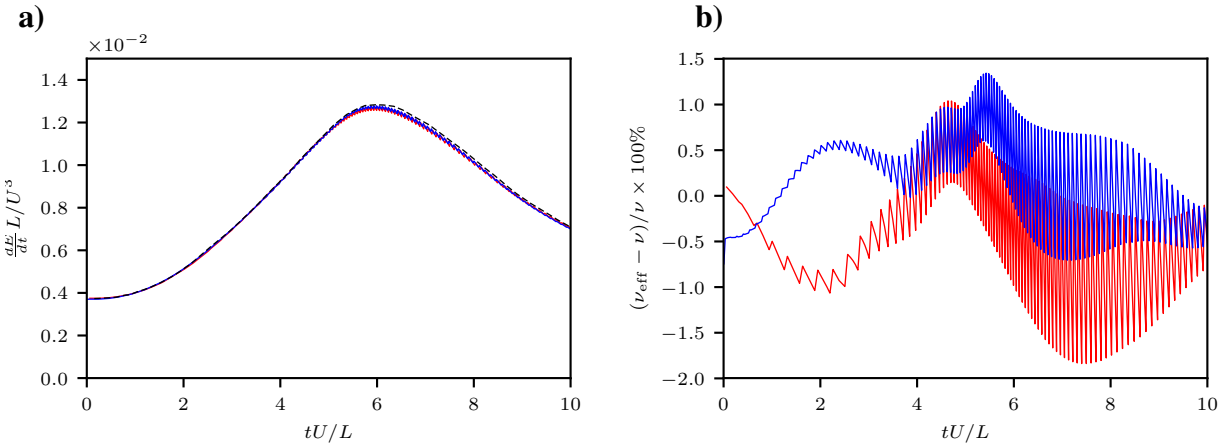

Figure 4.10: Comparison of diagnostics obtained from single- and multiresolution simulation of Taylor Green Vortex at $\mathrm{Re} = 200$. (a) Rate of change kinetic energy from simulation with uniform resolution ($h/L = 96$) (—) , simulation with the same base resolution ($h_0/L = 96$) using a single level of refinement (—) and simulation from Brachet et al. (1983) (- -) . (b) Relative error on effective viscosity from simulation with uniform resolution ($h/L = 96$) (—) and simulation with the same base resolution ($h_0/L = 96$) using a single level of refinement (—) .

fect of this. Consequently a much finer mesh must be used near the interface, than is required in the wake, thus the flow is well suited for multiresolution simulation. Moreover, it is evident from experiments that the wake behind a circular cylinder becomes 3D as early as at $Re \geq 190$ (Leweke and Williamson, 1998). This transition affects the measured lift- and drag force significantly. Hence, we consider a 3D finite periodic section of the geometry.

The 3D flow has also been simulated with a vortex-particle method by Cottet and Poncet (2003); Poncet (2004) at $\mathrm{Re} = 300$ and 400, who applied a Poisson solver with Dirichlet conditions on a body-fitted O-grid, coupled with a panel-diffusion approach to the cancel slip velocity at the interface. The impact of truncating the wake at a fixed outer radius, where the free-stream velocity is enforced, was rigorously clarified by Cottet and Poncet (2003) for the 2D flow. Homogeneous convergence of force coefficients and Strouhal number was observed, and a domain truncation about 6 diameters downstream the cylinder was found to be sufficient for acceptable results.

4.7.1 Setup

A section of the cylinder with length $L_z = 4.125D$ is simulated in the current using the multiresolution approach with mixed periodic and free-space conditions. L_z corresponds to about 5 times the principal wave length (λ_z) of the principal mode associated with the transition to 3D flow at this Re. The wave length was reported in Barkley and Henderson (1996) as $\lambda_z/D = 0.82$ and Poncet (2004) as $\lambda_z/D = 0.79$. In the stream wise direction (x) the computational domain extends $8D$ downstream from the cylinder. The height of the domain (y-direction) is adapted to the immediate vorticity field every 25 time step. 2 nested refinement patches are applied to have

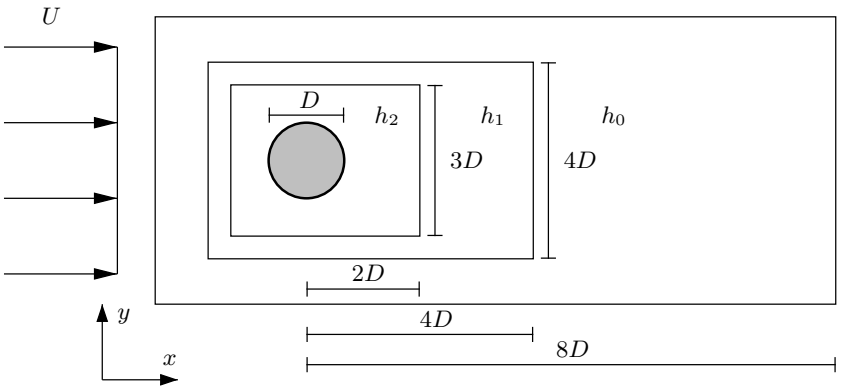

Figure 4.11: Multi resolution setup for simulation of flow past a circular cylinder with $h_0 = D/32$, $h_1 = D/64$ and $h_2 = D/128$. The domain length in the transverse direction is $L_z = 4.125D$.

sufficient resolution of the solid interface. In this case we found from a prior 2D studies that a mesh resolution of $h = D/128$ resulted in converged results in terms of the force coefficients and Strouhal number (not presented). The mesh resolution is gradually decreased downstream the cylinder using the patch configuration sketched in Fig. 4.11. Moreover, the Reynolds number based on the free stream velocity is $\mathrm{Re} = UD/\nu = 400$, corresponding to that of Poncet (2004).

For the advancement of particles a second order Runge-Kutta scheme with constant time-step $\Delta tU/D = 0.005$, to satisfy the constraint due to diffusion cf. Eq. (2.18). The Poisson solver used is for $m = 10$ and $\alpha = 1.5$, hence to be conservative a large buffer region of 16 cells was used for the refinement patches.

The vortex shedding is initialized artificially by ramping the direction of the free stream, with respect to horizontal, from 45° to 0° within the first 2 time units of the simulation.

4.7.2 Results

The dimensionless force coefficients are defined as

$$C_D = \frac{F_x}{\frac{1}{2}\rho U^2 D L_z}, \qquad C_L = \frac{F_y}{\frac{1}{2}\rho U^2 D L_z}. \tag{4.17}$$

The forces obtained with Eq. (3.21), Eq. (3.25) and the *momentum equation* from Noca et al. (1999) in a 2D study, are compared in Fig. 4.12. It may be seen that the forces obtained with Eq. (3.21) and Eq. (3.25) cannot be distinguished from each other, whereas the drag force obtained with the control volume formulation deviates slightly. This is likely since it involves the partial derivatives of the velocity field calculated by finite difference approximations. The deviation between the three expressions is insignificant and it may be concluded that Eq. (3.25) is able to give just as reliable an estimate as the two other formulations. Furthermore, it is valid in 3D and is thus used in the following. The force obtained in the 3D simulation has been plotted in Fig.4.13(a). At about $tU/D = 40$ a harmonic signal is observed which is associated with the 2D oscillatory flow. The flow transitions into the 3D at about $tU/D = 100$ as seen

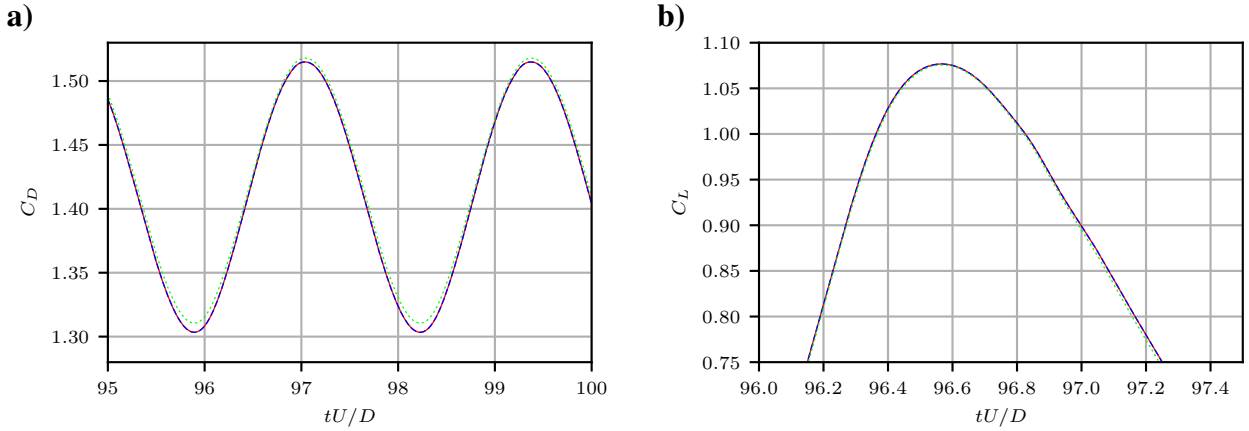

Figure 4.12: Drag and lift coefficient obtained with Eq. (3.21) (—) , Eq. (3.25) (- - -) and the *momentum equation* from Noca et al. (1999) (·····) in 2D simulation of flow past a circular cylinder at $\mathrm{Re} = 400$: (a) Drag. (b) Lift.

	2D		3D	
	$\bar{C}_D$	St	$\bar{C}_D$	St
Current study	1.414	0.22 ± 0.01	1.199	0.20 ± 0.02
Henderson (1995)	1.414	0.2198	–	–
Cottet and Poncet (2003)	1.408	0.2237	1.198	0.210

Table 4.1: Mean values of force coefficients and Strouhal number for flow past a circular cylinder at $\mathrm{Re} = 400$.

from the signals and stabilizes around $tU/D = 125$ as also seen from the immediate vorticity field at various times plotted in Fig. 4.14. Mean values and Strouhal numbers ($\mathrm{St} = fD/U$) for the two distinctive phases are given in Tab. 4.1. The currently obtained mean drag coefficient deviates by less than 0.5% from the results of Henderson (1995) and Cottet and Poncet (2003) and the deviation of the Strouhal number may be larger (0–6% in 2D and 0–24% in 3D) because of the uncertainty of this estimate due to a finite number of shedding cycles sampled.

The degree of three-dimensionality of the flow is quantified using the *transverse enstrophy* defined as

$$\mathcal{E}^{\perp} = \frac{1}{2} \int (\omega_x^2 + \omega_y^2) \, \mathrm{d}V. \tag{4.18}$$

As seen Fig. 4.13(b) the transverse enstrophy grows exponentially before saturation is reached at about $tU/D = 110$. The growth rate $1/b$ obtained from regression with the expression $a \exp\left(\frac{tU}{bD}\right)$ to the exponential region is $b = 1.51$. This is only 4% higher than the value ($b = 1.45$) observed by Poncet (2004). The main growth mode is identified from the peak in axial energy spectrum plotted in Fig. 4.13(c). The wave length of the mode is seen to be $\lambda_z/D = 0.825$ which deviates also about 4% from $\lambda_z/D = 0.79$ reported in Poncet (2004). The minor deviation is likely a consequence of the different span wise domain sizes ($L_z = 6.28D$ in Poncet (2004)). The profile of the transitional mode has been compared to that obtained by Poncet (2004) in Fig. 4.15. The two profiles are also very similar. For this simulation on average 20

iterations were used per time step and the number of particles varied from an average of 60×10^6 during the 2D stages to about 90×10^6 during the 3D stages.

4.8 Summary

A multiresolution vortex-particle mesh method based on a multilevel decomposition of the potential has been introduced and its consistency verified.

The refinement Green's functions used, with the multiresolution Poisson solver, are compact. By choosing α sufficiently small the method may be used with an overlap region small enough for practical applications. Moreover, it was demonstrated that the multiresolution approach could be combined with the iterative penalization technique to simulate bluff body flow. This was done for the circular cylinder at $\mathrm{Re} = 300$ and a combination of free-space and periodic boundary conditions. Reliable results were obtained hereby, both in terms of force coefficients and in terms of the topological structure of the vortex wake and growth-rate of the primary mode of the transition. The main challenge of the multiresolution method is the use of multilevel reconstruction by interpolation, which impose an additional restriction on the accuracy of the regularized Poisson solver. The smoothing error associated with interpolation is explicitly accounted for using the modification Eq. (4.8), but aliasing and imaging artifacts prevail. Further, work would consist of identifying more optimal interpolation schemes that suppress aliasing and imaging more than the particle-mesh interpolation functions are able to.

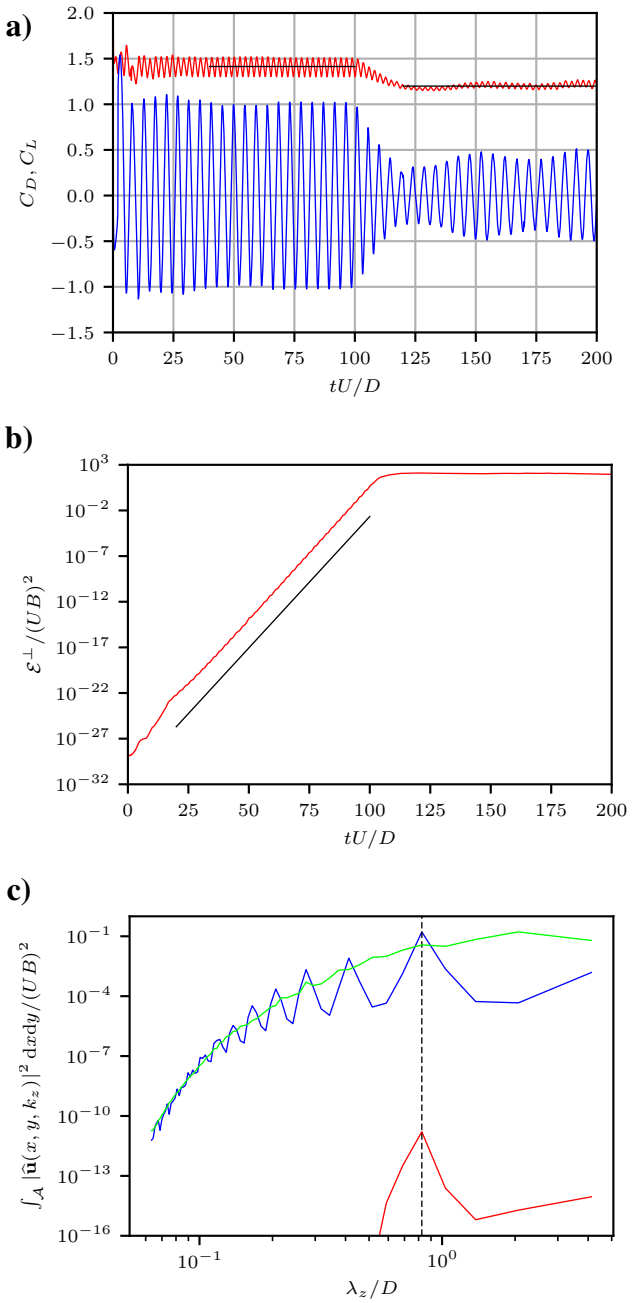

Figure 4.13: Flow past a circular cylinder at $\mathrm{Re} = 400$: (a) Evolution of drag coefficient (—), and lift coefficient (—) also indication of mean drag in 2D and 3D phase of the flow (—). (b) Evolution of transverse enstrophy (—) and $a \exp\left(\frac{tU}{bD}\right)$ with $b = 1.51$ (—). (c) Spectrum of transverse energy at $tU/D = 70$ (—), $tU/D = 110$ (—), $tU/D = 180$ (—) and indication of $\lambda_z/D = 0.825$ (- -).

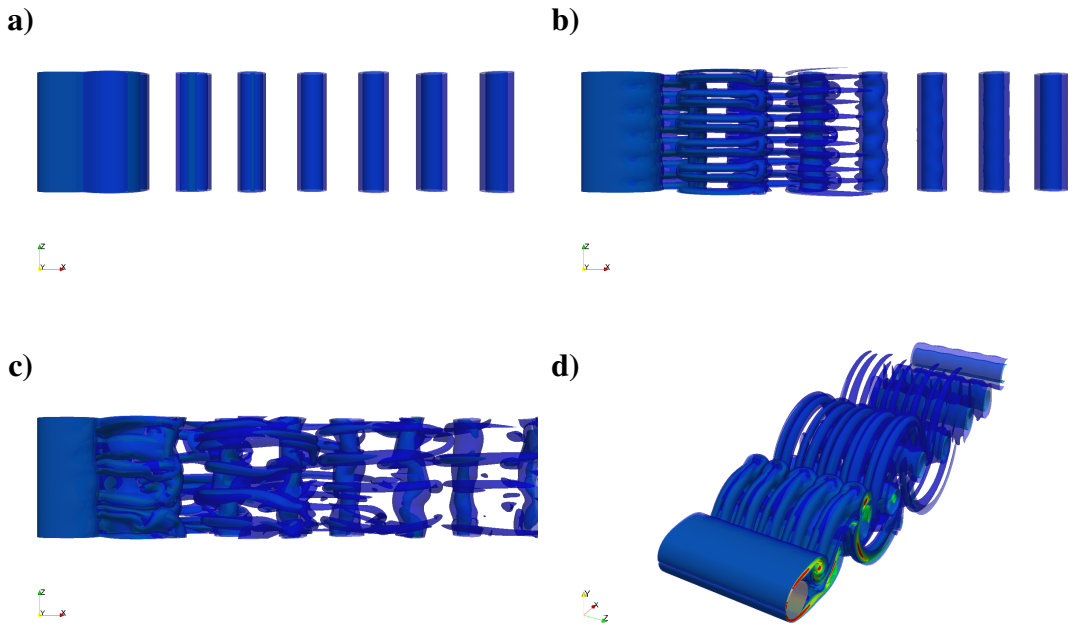

Figure 4.14: Isocontours of the immediate vorticity magnitude from blue to red $|\boldsymbol{\omega}|D/U = [2, 4, 6, 8]$ at various times: (a) $tU/D = 70$ (top-view). (b) $tU/D = 110$ (top-view). (c) $tU/D = 180$ (top-view). (d) $tU/D = 110$ (side-view).

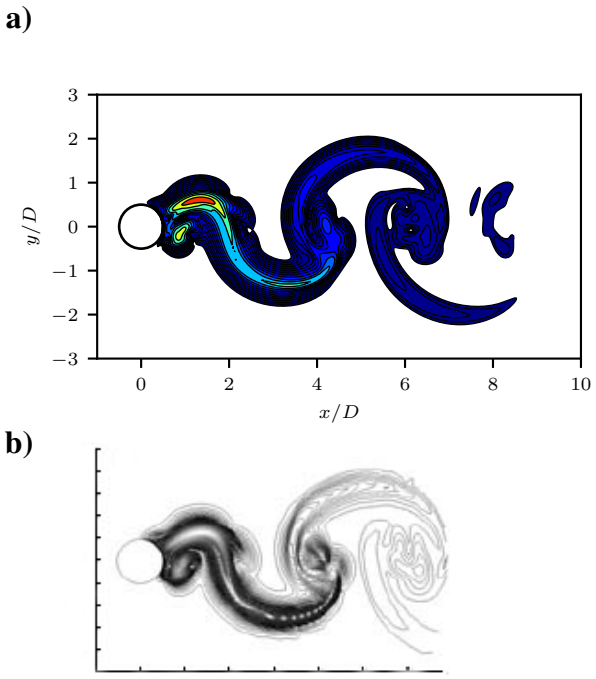

Figure 4.15: Isocontours of the spectral profile, $|\widehat{\boldsymbol{u}}(x, y, k_z)|^2$: (a) current study for $\lambda_z/D = 0.825$. (b) Poncet (2004) for $\lambda_z/D = 0.79$.

Chapter 5

Large eddy simulation

Parts of this chapter were prepared for a presentation at the APS conference 2017 entitled "A regularized vortex-particle mesh method for large eddy simulation" (Spietz et al., 2017b).

5.1 Modeling

A large eddy simulation approximates a solution to a spatially low-pass filtered variant of the governing equations. The solution is expressed in terms of the filtered variables. By denoting a filtered dependent variable (f) the result of a convolution with the filter kernel ζ of width Δ

$$\bar{f}(x,\Delta,t) = f * \zeta = \int_{-\infty}^{\infty} \zeta(x-x',\Delta) f(x',t)\, dx'. \tag{5.1}$$

and assuming commutation of the filter and the derivative operator, applying the filter to the momentum equation of the Navier-Stokes equation yields

$$\frac{\partial \bar{u}_i}{\partial t} + \frac{\partial \overline{u_i u_j}}{\partial x_j} = -\frac{\partial \bar{p}}{\partial x_i} + \nu \frac{\partial^2 \bar{u}_i}{\partial x_j^2}. \tag{5.2}$$

Eq. (5.2) may be rewritten in terms of scales that are conserved by the filter (resolved scales) and a tensor (τ_{ij}) that depends also on scales removed by the filter (unresolved scales)

$$\frac{\partial \bar{u}_i}{\partial t} + \frac{\partial \bar{u}_i \bar{u}_j}{\partial x_j} = -\frac{\partial \bar{p}}{\partial x_i} + \nu \frac{\partial^2 \bar{u}_i}{\partial x_j^2} - \frac{\partial \tau_{ij}}{\partial x_j} \tag{5.3}$$

$$\tau_{ij} = \overline{u_i u_j} - \bar{u}_i \bar{u}_j. \tag{5.4}$$

To close the system Eq. (5.3) we require a *subgrid-scale* (sgs) stress model that approximates the interaction of the unresolved scales with the resolved scales based on resolved quantities only.

Frequently used models are based on an eddy-viscosity (ν_{sgs}) approach to approximate τ_{ij}, i.e. assuming that the interaction between subgrid scales and resolved scales works in a manner similar to molecular diffusion

$$\tau_{ij} - \frac{1}{3}\delta_{ij}\tau_{kk} = -2\nu_{\text{sgs}}\bar{S}_{ij}, \quad \bar{S}_{ij} = \frac{1}{2}\left(\frac{\partial u_i}{\partial x_j} + \frac{\partial u_j}{\partial x_i}\right). \tag{5.5}$$

Since the trace of S_{ij} is zero, $\tau_{kk}\delta_{ij}$ is not modeled. The gradient of $\tau_{kk}\delta_{ij}$ may in stead be incorporated into a modified pressure, and is thus not important for the dynamics of incompressible flow.

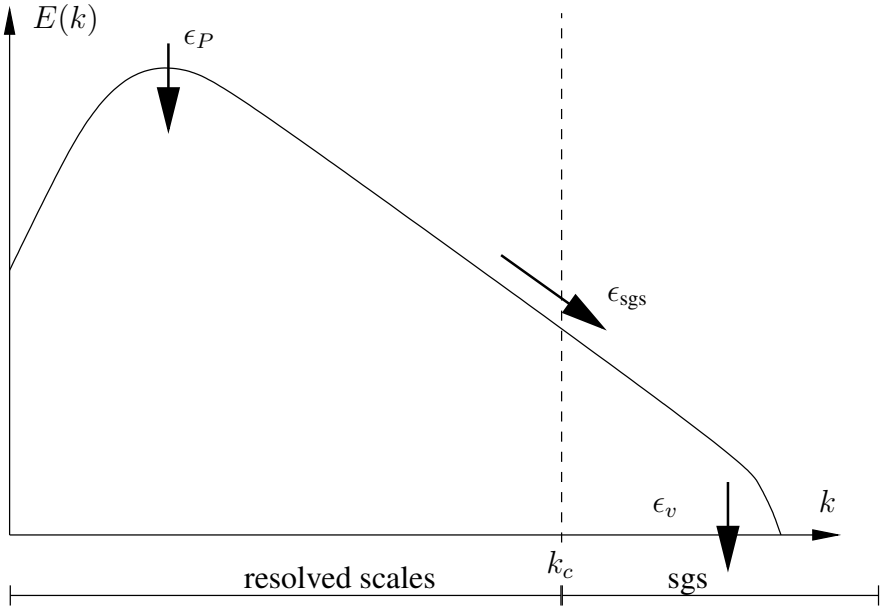

Figure 5.1: The Smagorinsky model is based on the assumption that the production of energy at large scales (ϵ_P), the energy transport through the filter cut-off (ϵ_{sgs}) and the energy dissipation of subgrid-scale energy near the Kolmogorov scale (ϵ_v) are in equilibrium. Indication of a filter cut-off at k_c

The eddy-viscosity is commonly used with the single coefficient Smagorinsky model (Smagorinsky, 1963)

$$\nu_{\text{sgs}} = (c_s\Delta)^2|\bar{S}|, \quad |\bar{S}| = \sqrt{2\bar{S}_{ij}\bar{S}_{ij}}. \tag{5.6}$$

5.1.1 Theoretical foundation

This model is based on the hypothesis that the energy spectrum in the range of the subgrid scales is in equilibrium; the average energy flux through the cut-off ($\langle\epsilon_{\text{sgs}}\rangle = \langle\tau_{ij}S_{ij}\rangle$) equals the average rate of viscous dissipation over the range spanned by the subgrid scales ($\langle\epsilon_v\rangle$) as sketched in Fig. 5.1 (see e.g. Sagaut (1998))

$$-\langle\tau_{ij}\bar{S}_{ij}\rangle = \langle\epsilon_v\rangle. \tag{5.7}$$

Based on dimensional analysis the eddy-viscosity should be modeled as $\nu_{\text{sgs}} \propto l_0^2 t_0^{-1}$, where l_0 and t_0 are respectively a characteristic length and time scale. Similarly the rate of viscous dissipation must be modeled $\epsilon_v \propto l_0^2/t_0^3$. The relation Eq. (5.6) is obtained for $l_0 = \Delta$ and $t_0 = |\bar{S}|^{-1}$.

Inserting Eq. (5.5) with the ansatz Eq. (5.6) into Eq. (5.7) gives the relation

$$\langle\epsilon_v\rangle = \langle\nu_{\text{sgs}}|\bar{S}|^2\rangle \simeq \langle\nu_{\text{sgs}}\rangle\langle|\bar{S}|^2\rangle \tag{5.8}$$

where $\langle|\bar{S}|^2\rangle = \langle\bar{\boldsymbol{\omega}}\cdot\bar{\boldsymbol{\omega}}\rangle$ is the average resolved enstrophy density per unit volume, which may

be determined under the assumption of isotropy

$$\langle|\bar{S}|^2\rangle = \int_0^{k_c} 2k^2 E(k)\,\mathrm{d}k. \tag{5.9}$$

Following Lilly (1967) the inertial spectrum $E(k) = K_0\langle\epsilon\rangle^{2/3}k^{-5/3}$ may be used to obtain an equation for the rate of total energy dissipation ($\langle\epsilon\rangle \simeq \langle\epsilon_v\rangle$) in terms of Δ, $\langle|\bar{S}|^2\rangle$ and the Kolmogorov constant ($K_0 \approx 1.5$)

$$\langle\epsilon\rangle = \left(\frac{\Delta}{\pi}\right)^2 \left(\frac{3}{2}K_0\right)^{-3/2} \langle|\bar{S}|^2\rangle^{3/2}. \tag{5.10}$$

Combining Eqs. (5.6), (5.8) and (5.10) the model coefficient c_s may be estimated as

$$c_s = \frac{1}{\pi}\left(\frac{3}{2}K_0\right)^{-3/4} \approx 0.17. \tag{5.11}$$

Using this coefficient, the model is a good approximation, when the flow has an equilibrium range and the kinetic energy spectrum is well described by the inertial spectrum such as in the case of isotropic decaying turbulence. In statistically unsteady or in-homogeneous flow a method using a constant model coefficient in the entire domain may not be appropriate. From the identity $\langle|\bar{S}|^2\rangle = \langle\bar{\boldsymbol{\omega}}\cdot\bar{\boldsymbol{\omega}}\rangle$ its is evident that the Smagorinsky model leads to non-zero turbulent-viscosity, whenever vorticity is non-zero. Hence, the model will also be active in laminar flow. Thus it does not display a physical near-wall behavior or can be used to simulate transitional flows accurately.

5.1.2 Dynamic variation

Variations of the Smagorinsky model have been proposed to improve its erroneous behavior. Germano et al. (1991) proposed to determine the coefficient adaptively by relating modeled stresses obtained at two separate filter scales. Such a dynamic approach has the advantage that a prior knowledge the model coefficient is not required. However the dynamic approach involve some kind of regularization to ensure numerical stability (Ghosal et al. (1995)). This has traditionally been averaging in one ore more homogeneous directions. This is possible e.g. in turbulent flows with one or more homogeneous directions such as a channel flow. If the problem has a higher degree of heterogeneity a local spatial averaging or an averaging along fluid trajectories may formally be better suited. These approached however introduce a dependency on the extent of the averaging region or a time span of the motion along trajectories considered.

The model coefficients of any sgs stress model may be determined dynamically. For simplicity we consider only an eddy viscosity model based on the Smagorinsky ansatz. The model parameter is adapted by relating sgs stresses T_{ij} and τ_{ij} obtained using two separate filters of width Δ ($\bar{}$) and $\gamma\Delta$ ($\widehat{}$), which is expressed using the Germano identity

$$L_{ij} = T_{ij} - \widehat{\tau}_{ij}, \tag{5.12}$$

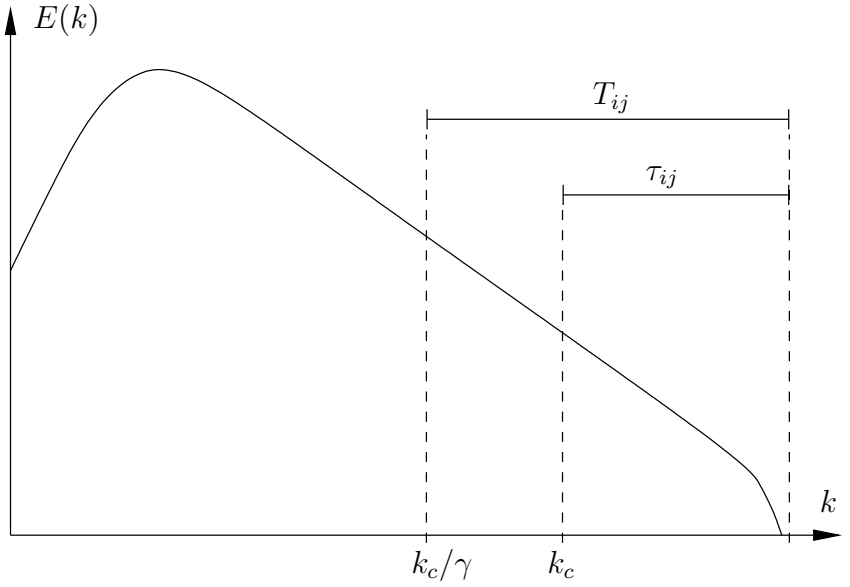

Figure 5.2: Indication of a primary filter (assuming spectrally sharp cut-off) of width Δ with spectral cut-off at $k_c = \frac{\pi}{\Delta}$ and test filter of width $\gamma\Delta$, $\gamma > 1.0$ with cut-off $k_c = \frac{\pi}{\gamma\Delta}$ utilized in dynamic procedure to estimate model coefficient, c_s^2. The sgs stress to model for the primary filter is τ_{ij} and the T_{ij} for test filter.

where L_{ij} is the resolved sgs stress associated with the test filter

$$L_{ij} = \widehat{\bar{u}_i\bar{u}_j} - \widehat{\bar{u}}_i\widehat{\bar{u}}_j, \quad T_{ij} = \widehat{\overline{u_iu_j}} - \widehat{\bar{u}}_i\widehat{\bar{u}}_j, \quad \widehat{\tau}_{ij} = \widehat{\overline{u_iu_j}} - \widehat{\bar{u}_i\bar{u}_j}. \tag{5.13}$$

These stresses may be approximated by applying Smagorinsky model to both filtered fields

$$\tau_{ij} = -2c_s^2(\Delta)^2|\bar{S}|\bar{S}_{ij}, \tag{5.14}$$

$$T_{ij} = -2c_s^2(\gamma\Delta)^2\Delta^2|\widehat{\bar{S}}|\widehat{\bar{S}}_{ij}. \tag{5.15}$$

By inserting Eq. (5.14)-(5.15) into Eq. (5.12) and assuming that c_s^2 has a weak spatial variation over the width of the filters it may be removed from the filter operation in Eq. (5.16)

$$e_{ij} = L_{ij} - 2c_s^2(\Delta)M_{ij} \quad \text{where} \tag{5.16}$$

$$M_{ij} = \Delta^2\left[\widehat{|\bar{S}|\bar{S}_{ij}} - \beta\gamma^2|\widehat{\bar{S}}|\widehat{\bar{S}}_{ij}\right] \quad \text{with} \quad \beta = \frac{c_s^2(\gamma\Delta)}{c_s^2(\Delta)}. \tag{5.17}$$

The standard dynamic model of Germano et al. (1991) uses only a single test filter and assumes that c_s^2 is the same at two cut-off scales, which implies that $\beta = 1$ in Eq. (5.16). With this assumption the minimizer of (5.16) in the least square sense is

$$c_s^2(\Delta) = \frac{L_{ij}M_{ij}}{M_{ij}M_{ij}}. \tag{5.18}$$

This expression may be singular, hence instead a minimizer for an averaged error $\langle e_{ij}\rangle$ is sought

$$c_s^2(\Delta) = \frac{\langle L_{ij}M_{ij}\rangle}{\langle M_{ij}M_{ij}\rangle}. \tag{5.19}$$

Scale-similarity ($\beta = 1$) may not be a good assumption, when the filters cuts the spectrum outside an inertial range. Either when the simulation approaches a DNS, such that the cut-off filter falls close to the Kolmogorov scale or if the filter cut-off approaches the integral scale in an underresolved or locally underresolved simulation. (Porte-Agel et al., 2000) formulated a scale-dependent dynamic model by assuming a power-law relation of the model coefficient which relies on an additional test filter and thereby increased computational overhead.

5.1.3 Lagrangian averaging

In the present work averaging along particle trajectories as proposed by Meneveau et al. (1996) is applied. The average of the fields along particle trajectories may be written as the integrals

$$\mathcal{I}_{LM}(\boldsymbol{x},t) = \int_{-\infty}^{t} L_{ij}M_{ij}(\boldsymbol{z}(t'),t')W(t-t')\,dt' \tag{5.20}$$

$$\mathcal{I}_{MM}(\boldsymbol{x},t) = \int_{-\infty}^{t} M_{ij}M_{ij}(\boldsymbol{z}(t'),t')W(t-t')\,dt', \tag{5.21}$$

where $\boldsymbol{z}(t)$ is the particle position on the trajectory. By choosing the weighting function $W(t-t')$ as

$$W(t-t') = \frac{1}{T}e^{\frac{-(t-t')}{T}} \tag{5.22}$$

a control of the temporal averaging length along trajectories through a parameter (T) is ensured and further Eqs. (5.20)–(5.21) become solutions to the transport equations

$$\frac{D\mathcal{I}_{LM}}{Dt} = \frac{1}{T}(\mathcal{L}_{ij}\mathcal{M}_{ij} - \mathcal{I}_{LM}) \tag{5.23}$$

$$\frac{D\mathcal{I}_{MM}}{Dt} = \frac{1}{T}(\mathcal{M}_{ij}\mathcal{M}_{ij} - \mathcal{I}_{MM}). \tag{5.24}$$

To prevent one of the averaged quantities from becoming negative, which may render a numerical method unstable, we use an averaging time as

$$T = \theta\Delta(\mathcal{I}_{LM}\mathcal{I}_{MM})^{-1/8}, \tag{5.25}$$

where a constant value $\theta = 1.5$ is based on correlations obtained from DNS of homogeneous isotropic decaying turbulence (Meneveau et al., 1996). Eq. (5.25) is not a universal relation. It may be argued that in flows with higher degree of heterogeneity a shorter time scale would be more appropriate see e.g. Murakami et al. (1999). Verma and Mahesh (2012) even proposed to solve an additional transport equation for the averaging time, but noted that for moderate Reynolds flow past a circular cylinder the results agree reasonably well those obtained from Eq. (5.25) with $\theta = 3$.

5.2 Implementation in vortex-particle mesh method

The sgs stress is introduced into the vorticity transport equation (Eq. (2.2)) as a vortex force ($\boldsymbol{g}_{\text{sgs}}$)

$$\frac{D\bar{\boldsymbol{\omega}}}{Dt} = (\bar{\boldsymbol{\omega}} \cdot \boldsymbol{\nabla})\bar{\boldsymbol{u}} + \nu\boldsymbol{\nabla}^2\bar{\boldsymbol{\omega}} + \boldsymbol{g}_{\text{sgs}}, \tag{5.26}$$

where $\boldsymbol{g}_{\text{sgs}}$ may be expanded as

$$\boldsymbol{g}_{\text{sgs}} = \boldsymbol{\nabla} \times (\boldsymbol{\nabla}\nu_{\text{sgs}} \cdot \left[\nabla\bar{\boldsymbol{u}} + (\nabla\bar{\boldsymbol{u}})^T\right] + \nu_{\text{sgs}}\boldsymbol{\nabla}^2\bar{\boldsymbol{u}}). \tag{5.27}$$

We use a simplified expression corresponding to that of Mansfield et al. (1998) and compute the vortex force from the divergence-free expression

$$\boldsymbol{g}_{\text{sgs}} \approx \boldsymbol{\nabla} \cdot \left(\nu_{\text{sgs}} \left[\boldsymbol{\nabla}\bar{\boldsymbol{\omega}} - (\boldsymbol{\nabla}\bar{\boldsymbol{\omega}})^T\right]\right). \tag{5.28}$$

Eq. (5.23), Eq. (5.24) and Eq. (5.26) are discretized using the VPM method of Chap. 2; the two averaged quantities are similarly to the vorticity field also carried by the vortex-particles. However due to the requirement of positivity of the averaged quantities to preserve numerical stability, particle-mesh interpolation of these is carried out using linear interpolation, which preserves the sign of the interpolated quantities. The discrete approximation is evolved in the Lagrangian frame of reference as

$$\frac{\mathrm{d}\boldsymbol{x}_p}{\mathrm{d}t} = \bar{\boldsymbol{u}}(\boldsymbol{x}_p, t) \tag{5.29}$$

$$\frac{\mathrm{d}\bar{\boldsymbol{\omega}}_p}{\mathrm{d}t} = \left[(\bar{\boldsymbol{\omega}} \cdot \boldsymbol{\nabla})\bar{\boldsymbol{u}} + \nu\boldsymbol{\nabla}^2\bar{\boldsymbol{\omega}} + \boldsymbol{\nabla} \cdot \left(\nu_{\text{sgs}} \left[\boldsymbol{\nabla}\bar{\boldsymbol{\omega}} - (\boldsymbol{\nabla}\bar{\boldsymbol{\omega}})^T\right]\right)\right]_p \tag{5.30}$$

$$\frac{\mathrm{d}\mathcal{I}_{LM\,p}}{\mathrm{d}t} = \left[\frac{1}{T}(\mathcal{L}_{ij}\mathcal{M}_{ij} - \mathcal{I}_{LM})\right]_p \tag{5.31}$$

$$\frac{\mathrm{d}\mathcal{I}_{MM\,p}}{\mathrm{d}t} = \left[\frac{1}{T}(\mathcal{M}_{ij}\mathcal{M}_{ij} - \mathcal{I}_{MM})\right]_p. \tag{5.32}$$

Second or third order Runge-Kutta schemes are used to advance particle-vorticity and particle-position but explicit Euler for the particle-averages. This is done as it was observed by Meneveau et al. (1996) that a high accuracy on the estimates of the average quantities is not necessary. For simplicity we use the same time-step size for all quantities. The Eqs. (5.23)–(5.24) contain non-linear terms of up to fourth order hence the solution may be highly fluctuating. Vasilyev et al. (2008) proposed to by-pass this problem introducing a diffusive term in the transport equation for the averaged quantities. We have observed that these fluctuations are satisfactorily smoothed from re-meshing with linear interpolation.

The computation of the right hand side of Eqs. (5.31)–(5.31) requires the test filtering of the three velocity components ($\bar{u}_i$) which is done while solving the Poisson equation. Additionally the computation requires test filtering of two symmetric second order tensors ($\bar{u}_i\bar{u}_j$ and $|\bar{S}_{ij}|\bar{S}_{ij}$) with 12 unique components in total, which are computed in real-space from $\bar{u}_i$ and subsequently filtered in Fourier-space. Because these tensor fields may be less compact than the vorticity, even-symmetry is assumed at free-space boundaries and the filtering is therefore carried out using real-to-real fast DCT transforms without zero-padding, which makes filtering less expensive than obtaining a solution to the Poisson equation.

5.3 Verification

5.3.1 Homogeneous isotropic turbulence

A velocity field with properties of isotropic turbulence is synthesized using the procedure by Rogallo and Moin (1984) by generating a distribution of random Fourier coefficients matching a radial target spectrum ($E(|\boldsymbol{k}|)$). This is useful for the generation of initial conditions in simple problems of homogeneous turbulence to study the consistency and accuracy of the sgs model proposed and may be used in a vortex formulation by computing the corresponding vorticity field.

For each wave number a pair of complex random numbers are generated

$$a = \sqrt{E(|\boldsymbol{k}|)/\left(2\pi|\boldsymbol{k}|^2\right)}\exp\left(i\theta_1\right)\,\cos\left(\phi\right) \tag{5.33}$$

$$b = \sqrt{E(|\boldsymbol{k}|)/\left(2\pi|\boldsymbol{k}|^2\right)}\exp\left(i\theta_2\right)\,\sin\left(\phi\right), \tag{5.34}$$

where the complex phases $\theta_1, \theta_2, \phi \in [0, 2\pi]$ are drawn from a uniform distribution. The random complex numbers are then used to construct the Fourier coefficients of the velocity field which by construction is divergence free as the coefficient vector ($\widehat{\boldsymbol{u}}$) is parallel to the wave number vector $\boldsymbol{k}$

$$\widehat{\boldsymbol{u}}_1 = \frac{a|\boldsymbol{k}|k_2 + bk_1k_3}{|\boldsymbol{k}|\sqrt{k_1^2+k_2^2}} \tag{5.35}$$

$$\widehat{\boldsymbol{u}}_2 = \frac{bk_2k_3 - a|\boldsymbol{k}|k_1}{|\boldsymbol{k}|\sqrt{k_1^2+k_2^2}} \tag{5.36}$$

$$\widehat{\boldsymbol{u}}_3 = \frac{-b\sqrt{k_1^2+k_2^2}}{|\boldsymbol{k}|}. \tag{5.37}$$

Finally the vorticity field is approximated by spectral differentiation. Hermitian symmetry of the Fourier coefficients ensures a zero imaginary part in real space and is required to generate physically meaningful fields and must be enforced explicitly.

5.3.2 Forced isotropic turbulence

As a first experiment we test the performance of the model to predict a decay of modal energy as $E(k) \propto k^{-5/3}$ in correspondence with the Kolmogorov law. To do this an initial condition is generated with the outlined procedure matching a $E(k) \propto k^{-5/3}$ radial spectrum. Then an external force ($\boldsymbol{f}$) is applied to the system as proposed by Ghosal et al. (1995) that injects energy into the largest scales at a constant rate

$$\widehat{\boldsymbol{f}} = \begin{cases} \epsilon\dfrac{\widehat{\boldsymbol{u}}}{N_k|\widehat{\boldsymbol{u}}|^2} & \text{for} \quad |\boldsymbol{k}| < 2 \\ 0 & \text{for} \quad |\boldsymbol{k}| \geq 2, \end{cases} \tag{5.38}$$

where N_k is the number of Fourier coefficients within the shell $|k| < 2$. By applying Parseval's theorem it is seen that the rate of change of energy in the system due to the force is

$$\frac{\int_V \boldsymbol{f}\cdot\boldsymbol{u}\;d\boldsymbol{x}}{V} = \frac{1}{2}\sum(\widehat{\boldsymbol{f}}^*\cdot\widehat{\boldsymbol{u}} + \widehat{\boldsymbol{f}}\cdot\widehat{\boldsymbol{u}}^*) = \epsilon. \tag{5.39}$$

The corresponding vortex force as applied within a vorticity-velocity formulation $\boldsymbol{g} = \nabla \times \boldsymbol{f}$ has the Fourier coefficients

$$\widehat{\boldsymbol{g}} = \begin{cases} \epsilon \dfrac{\widehat{\boldsymbol{\omega}}}{N_k |\widehat{\boldsymbol{u}}|^2} & \text{for} \quad |\boldsymbol{k}| < 2 \\ 0 & \text{for} \quad |\boldsymbol{k}| \geq 2. \end{cases} \tag{5.40}$$

In the algorithm the force is applied directly in Fourier space in an Euler time-split-step as

$$\widehat{\boldsymbol{\omega}}^* = \widehat{\boldsymbol{\omega}}^n + \Delta t \widehat{\boldsymbol{g}}^n. \tag{5.41}$$

We run simulations assuming the explicit filter is one out of two different filters: the first the smooth Gaussian ($m = 10$) with $\Delta = \alpha h$ and $\alpha = 1.5$ and the second a Fourier cut-off filter. For test filtering $\gamma = 2$ is used. The outlined LES method was derived assuming a well known filter. However, a numerical approximation implies truncation errors. The effect of the approximation is commonly denoted the *mesh filter*, which is in general not known. LES is commonly carried out assuming a shape of this filter. Alternatively, for methods that do not have spectral accuracy, one may seek to minimize the effect of numerical errors besides the projection, by explicitly applying a filter, for which the sgs stress may then be recovered using variations of the approximate deconvolution model (ADM) (Stolz and Adams, 1999; Stolz et al., 2001). Although appealing, explicit filtering cannot directly, be used in a Lagrangian formulation due to the implicit treatment of the convective term. Replacing the vorticity field by its filtered version every time step ensures a limited frequency content in the solution, but the cumulative effect of multiple filter operations is harmful if

$$\zeta \neq \zeta * \zeta * ..., \tag{5.42}$$

as emphasized by Lund (2003). In stead the model is tested in the naive way; only the velocity is explicitly filtered regularly as a consequence of using a regularized Poisson solver. We assume that the mesh filter is that used for regularizing the Poisson equation. A filtered velocity is sufficient to approximate the eddy-viscosity with the Smagorinsky model, when formulated solely in terms of velocity. In case of a sharp Fourier cut-off filter both velocity and vorticity are filtered every time step for consistency, since in that case

$$\zeta = \zeta * \zeta * .... \tag{5.43}$$

Fig. 5.3 and shows the results obtained using respectively the two filters at resolution $h = L/48$. The presented energy spectra are averages of samples taken every time step over 8 integral large-scale turnover times discarding 2 turnover times before approximate steady state was observed. The spectra are close in the medium wave number range $k/k_{\max} = 0.1 - 0.7$ and only a slight variation is observed in the high wave number range. When the spectrum is pre-multiplied by $k^{5/3}$ it is seen that there exist only a short range $k/k_{\max} = 0.2 - 0.3$ where the gradient is close to zero indicating the inertial subrange. From experiments the Kolmogorov value have been reported to take a value in the range $1.3 - 2.1$ (Chasnov, 1991). We expect the pre-multiplied spectrum fall within this range for high wave numbers too since the Kolmogorov scale is infinitely small in this case of vanishing viscosity. However the results are observed to be out of range for $k > 0.4k_{\max}$, which is expected for the smooth filter. For the sharp filter

we can relate this to numerical dissipation associated with numerical approximations used with the particle method, especially re-meshing of particle-vorticity. The volume averaged model coefficient, which was initially set to $c_s = 0.17$ according to the theoretical value, levels out in the range $0.17 - 0.18$ corresponding to a slight overshoot as compared to the expected value for the smooth filter indicating that the effective width of the filter is $\Delta > \alpha h$ because of smooth cut-off.

5.3.3 Decaying isotropic turbulence

As a second case we test the ability of the model to reproduce the decay of energy in a turbulent flow from an initial radial spectrum measured in a wind tunnel by Comte-Bellot and Corrsin (1971). In the experiment turbulence was generated by leading the flow through a grid of spacing $M = 5.08\,\mathrm{cm}$. Energy spectra were measured at three locations downstream where the Reynolds number based on Taylor's micro scale was measured within $Re_\lambda = 71.6 - 60.0$. The locations were converted to times assuming that all fluid traveled with the mean cross sectional wind speed, which was measured as a function of downstream distance. Furthermore a wind speed prior to the grid $U_0 = 10\,\mathrm{m/s}$ was reported for the experiment. The simulations are performed in a triple periodic box of side length $L = 10.8M$. The turbulence is initialized through an initial vorticity field using the spectrum obtained at first location in the experiment corresponding to the time $tU_0/M = 42$ filtered according to the filter used with the LES formulation. The viscosity was adapted so that initially the Reynolds number matched the experiment.

The simulated energy spectrum at the three different times are plotted for various grid resolutions in Fig. 5.4(a) and Fig. 5.5(a). There is a notable difference between results using the two different filter types. The smooth filter results in a smooth decay near the cut-off, but also pile-up in the mid wavenumber range. This indicate that the model is too dissipative in the high wavenumber range, which partly obstructs the turbulent cascade. In both cases the total resolved energy compares equally well with the experiments as other studies using the Lagrangian dynamic model (Meneveau et al., 1996; Anderson and Meneveau, 1999) as shown in Fig. 5.4(b) and Fig. 5.5(b). Probability density functions of c_s^2 plotted in Fig. 5.4(c) and Fig. 5.5(c) show that in both cases the initial $c_s = 0.17$ develops into smooth distributions with mean value $c_s \approx 0.18 - 0.20$. Clipping of the averaged quantities was found necessary in order to preserve the stability of the Lagrangian averaging procedure, which impose a minimum constrain on the model coefficient as $c_s^2 \approx 1 \times 10^{-5}$. This is reflected in the distributions as the peaks observed close to $c_s = 0$. The clipping occur for 3–5% of the field when using the sharp cut-off filter and 1–2% of the field when using the smooth filter. The flow is simulated for different mesh resolutions, using a fixed filter width. The results in Fig. 5.4 and Fig. 5.5 demonstrate approximate mesh convergence, although only explicitly filtered in case of the sharp filter. This indicates that the results observed are consequences of the sgs stress model and not errors due to approximation of partial derivatives and interpolation. The distribution of model coefficient, however is seen to shifted toward higher c_s for the coarser resolutions, which could be a consequence of the low order interpolation used with the averaged quantities.

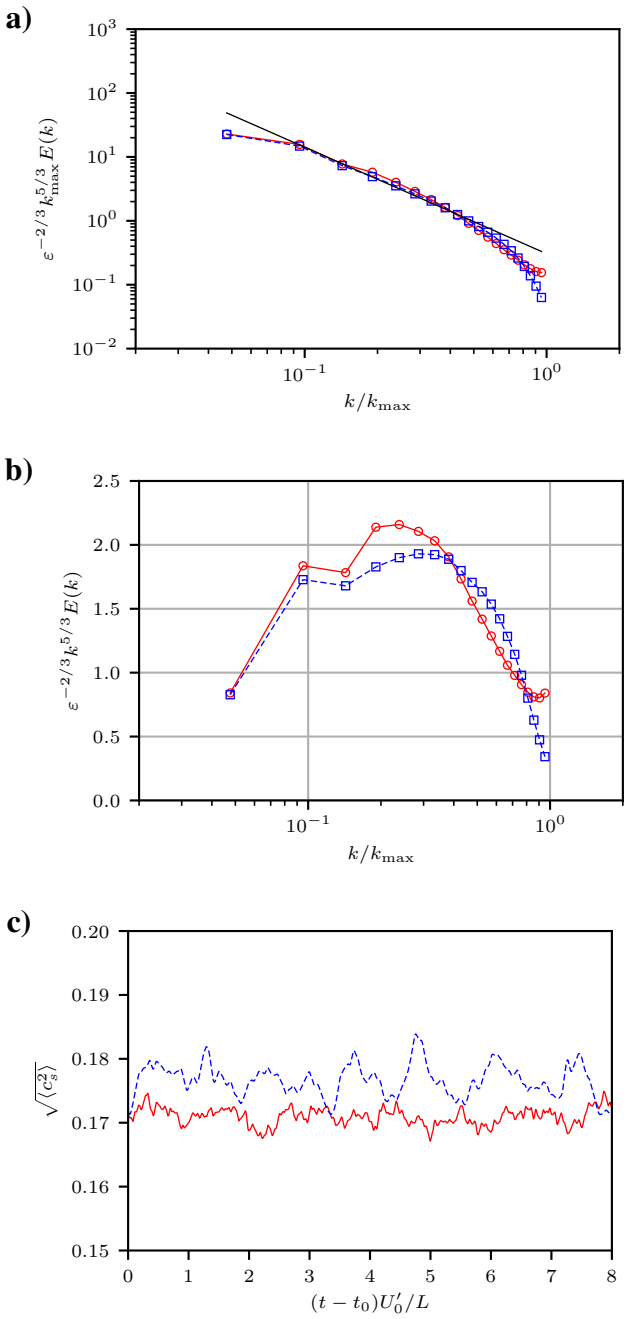

Figure 5.3: LES simulations of forced isotropic turbulence: (a) Averaged energy spectrum for sharp Fourier cut-off filter ($k_c = \pi/(\alpha h)$, $\alpha = 1.5$) (—○—) , for Gaussian filter ($m = 10$, $\alpha = 1.5$) (—□—) and slope of -5/3 (—) . (b) Averaged energy spectrum pre-multiplied $k^{5/3}$ for sharp Fourier cut-off filter ($k_c = \pi/(\alpha h)$, $\alpha = 1.5$) (—○—) and for Gaussian filter ($m = 10$, $\alpha = 1.5$) (—□—) , (c) Time history of model coefficient for sharp Fourier cut-off filter ($k_c = \pi/(\alpha h)$, $\alpha = 1.5$) (—○—) and for Gaussian filter ($m = 10$, $\alpha = 1.5$) (—□—) .

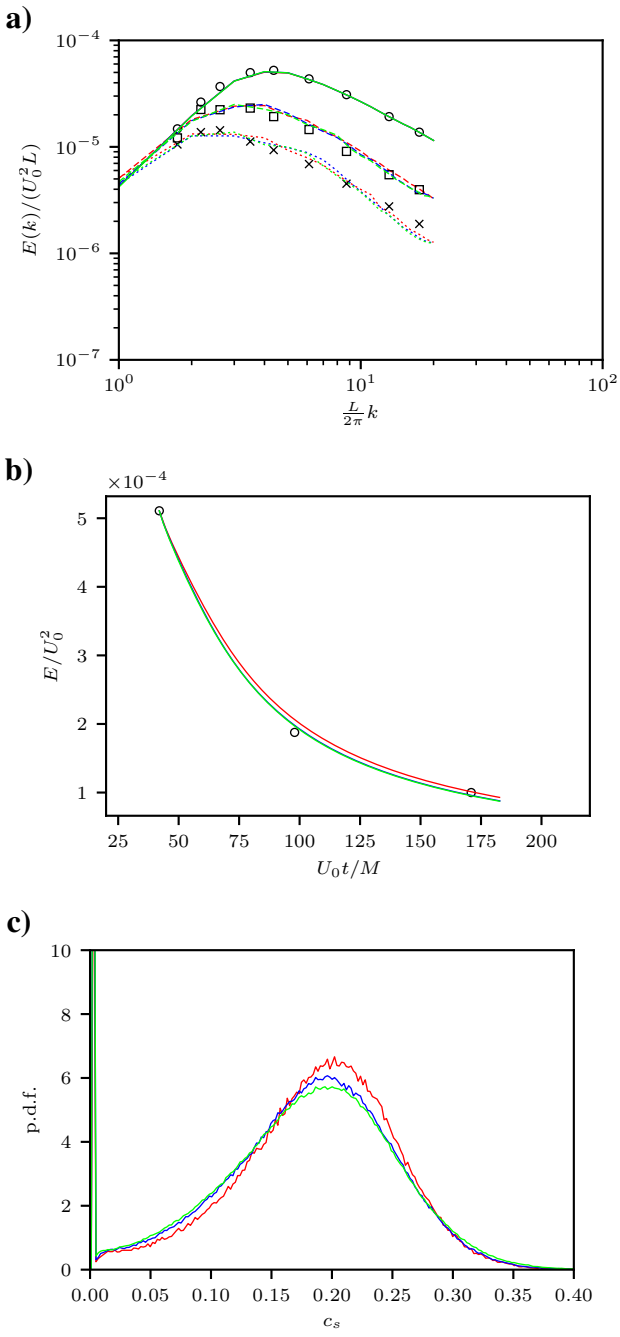

Figure 5.4: LES simulations of decaying isotropic turbulence using spectral velocity kernel and sharp cut-off filter: (a) Spectrum of resolved energy from simulation and (filtered) experiment by Comte-Bellot and Corrsin (1971) at times $tU_0/M = 42$, 98 and 171 as (○) , (□) and (×) . (b) Time variation of resolved energy from compared to (filtered) experiment by Comte-Bellot and Corrsin (1971) (○) . (c) Distribution of model coefficient at time 171. Line colors indicate different mesh resolutions and filter cut-off as $L/h = 64$ and $k_s = \pi/(1.5h)$ (—) , $L/h = 96$ and $k_s = \pi/(2.25h)$ (—) , $L/h = 128$ and $k_s = \pi/(3.0h)$ (—) .

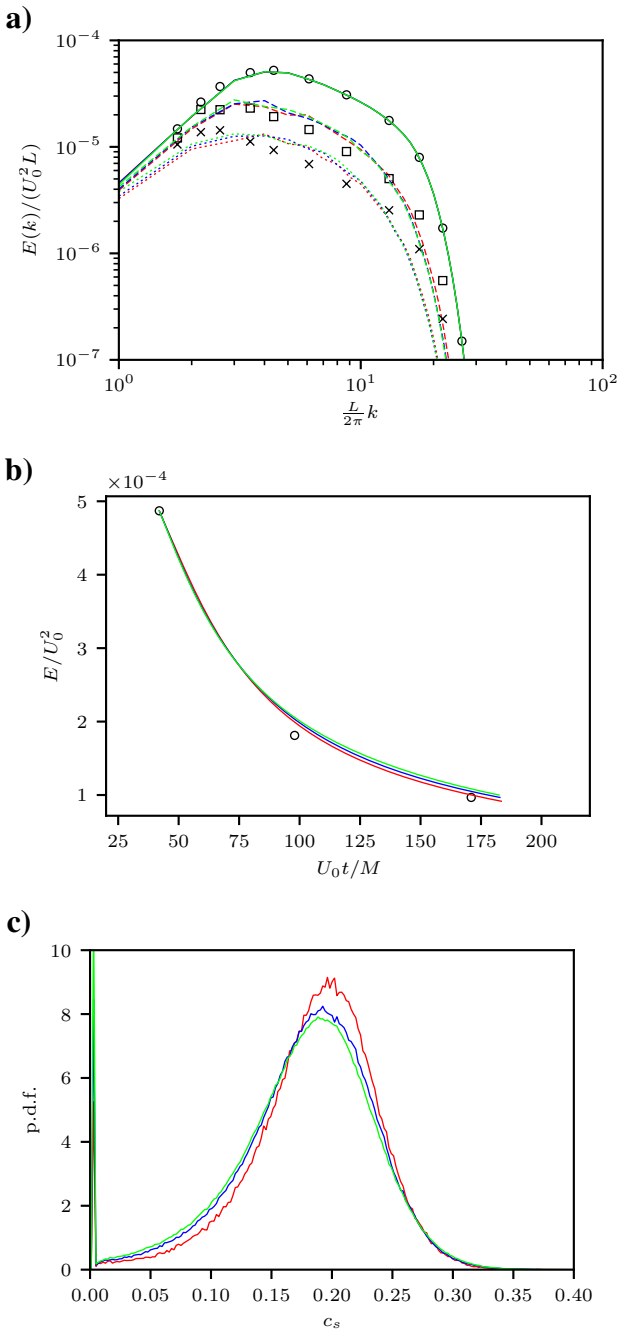

Figure 5.5: LES simulations of decaying isotropic turbulence using spectral velocity kernel and Gaussian filter ($m = 10$): (a) Spectrum of resolved energy from simulation and (filtered) experiment by Comte-Bellot and Corrsin (1971) at times $tU_0/M = 42$, 98 and 171 as (○) , (□) and (×) . (b) Time variation of resolved energy from compared to (filtered) experiment by Comte-Bellot and Corrsin (1971) (○) . (c) Distribution of model coefficient at time 171. Line colors indicate different mesh resolutions and filter cut-off as $L/h = 64$ and $\alpha = 1.5$ (—) , $L/h = 96$ and $\alpha = 2.25$ (—) , $L/h = 128$ and $\alpha = 3.0$ (—) .

5.4 Breakdown of counter rotating vortex pairs

We revisit the counter rotating vortex pairs simulated in Sec. 2.4. In case of vanishing viscosity, the instability of the flow results in rapid transition from a 2D state in into a complex turbulent state. It serves as a test of the sgs models performance in a transitional flow. This was also studied by Cocle et al. (2007), who simulated inviscid vortex pair using both a pseudo-spectral method and VPM method and compared various sgs models.

The simulation setup is the same as was used in Sec. 2.4 for mesh resolution is $h/L_z = 128$ and the Gaussian velocity kernel ($m = 10$, $\alpha = 1.5$). The evolution of the total energy and the mean transverse energy are plotted in Fig. 5.6. It may be seen that around time $t/T = 0.6$ the mean and total energy diverge, indicating that the flow becomes 3D, which is also seen from the immediate vortex structures in Fig. 5.7. The ideal simulation would not have dissipation until this point as viscosity is zero and the flow is laminar. This is also obtained using a pseudo-spectral method and high order hyper-viscosity sgs model from Cocle et al. (2007), which dissipates energy only in the high wavenumber range. Clearly the Smagorinsky models do not conserve energy before transition. The dynamic model, for which $c_s = 0$ at $t/T = 0$ is however less dissipative and it may be concluded that the dynamic model is an improvement as compared to the simple model. It still does not compare as well as the multiscale models reported in that study (not shown), which indicate that the Smagorinsky model, even if dynamic, might not be the optimal choice for vortex flow simulation. The transverse energy spectrum has been plotted in Fig. 5.6 for the two models at the final time of the simulation, which both displays an inertial range and significant decay due to the filter for $\frac{L_z}{2\pi}k_z > 10$. The spectrum obtained with the dynamic model has slightly more energy at high wave numbers.

5.5 Flow past a square cylinder at $\mathrm{Re} = 2.2 \times 10^4$

5.5.1 Setup

A challenging case for turbulent bluff body flow simulation using the VPM method is the case of the flow past a square cylinder at a moderate Reynolds number of $Re = UD/\nu = 2.2 \times 10^4$. The case has been thoroughly studied in the literature both experimentally e.g. by Lyn et al. (1995) and numerically using various LES models e.g. by Rodi et al. (1997); Sohankar et al. (2000) and by direct numerical simulation (DNS) by Trias et al. (2015). Here the performance of both the simple Smagorinsky model (SSM) and the dynamic Smagorinsky model (DSM) used with the VPM method is compared to these benchmarks.

The flow is simulated for $C_{\mathrm{LCFL}} = 0.125$ using a third-order Runge-Kutta time-step scheme. The axial extent of the domain is $L_z = 4D$, which has been found sufficient for various simulation configurations by Rodi et al. (1997).

The sharp edges of the body ensure that the points where the boundary layers separates are fixed to the upstream corners of the cylinder, which relaxes the requirement of well-resolved boundary layers in order to capture qualitatively well the large scale dynamics of the flow. This is convenient as the current method does not support anisotropic grids to resolve steep gradients in the wall normal direction. Using a multiresolution setup with a two level refinement region close to the cylinder as sketched in Fig. 5.8, the size of the first cell next to the wall corresponds

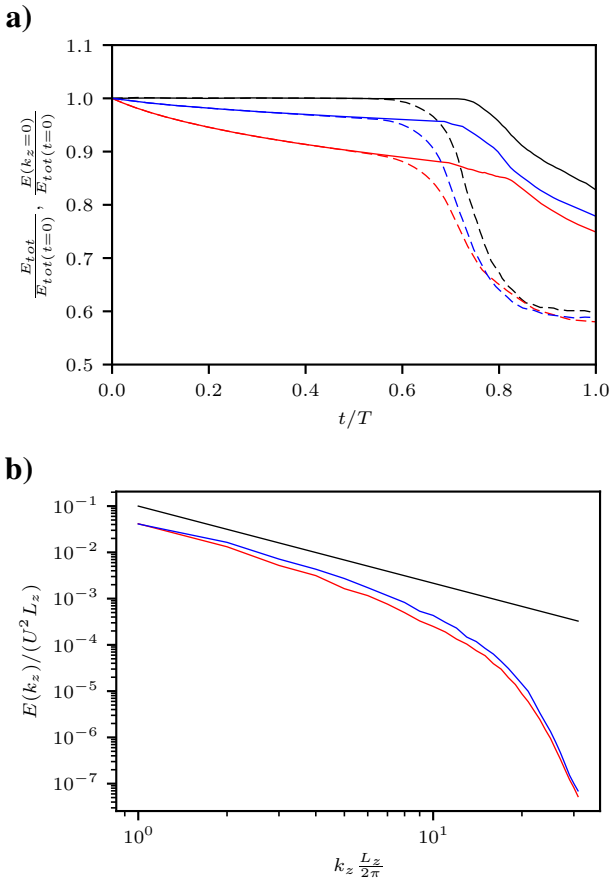

Figure 5.6: LES of inviscid break down of counter rotation vortex pairs. (a) The total resolved energy from pseudo-spectral simulation with high order hyper-viscosity sgs model from Cocle et al. (2007) (—) , dynamic Smagorinsky model (—) and standard Smagorinsky (—) . The resolved energy corresponding to $k_z = 0$ from Cocle et al. (2007) (- -) , dynamic Smagorinsky model (- -) and simple Smagorinsky (- -) . (b) Resolved energy spectrum at time $t/T = 2.0$ for dynamic Smagorinsky model (—) , simple Smagorinsky (—) , and -5/3 slope (—) .

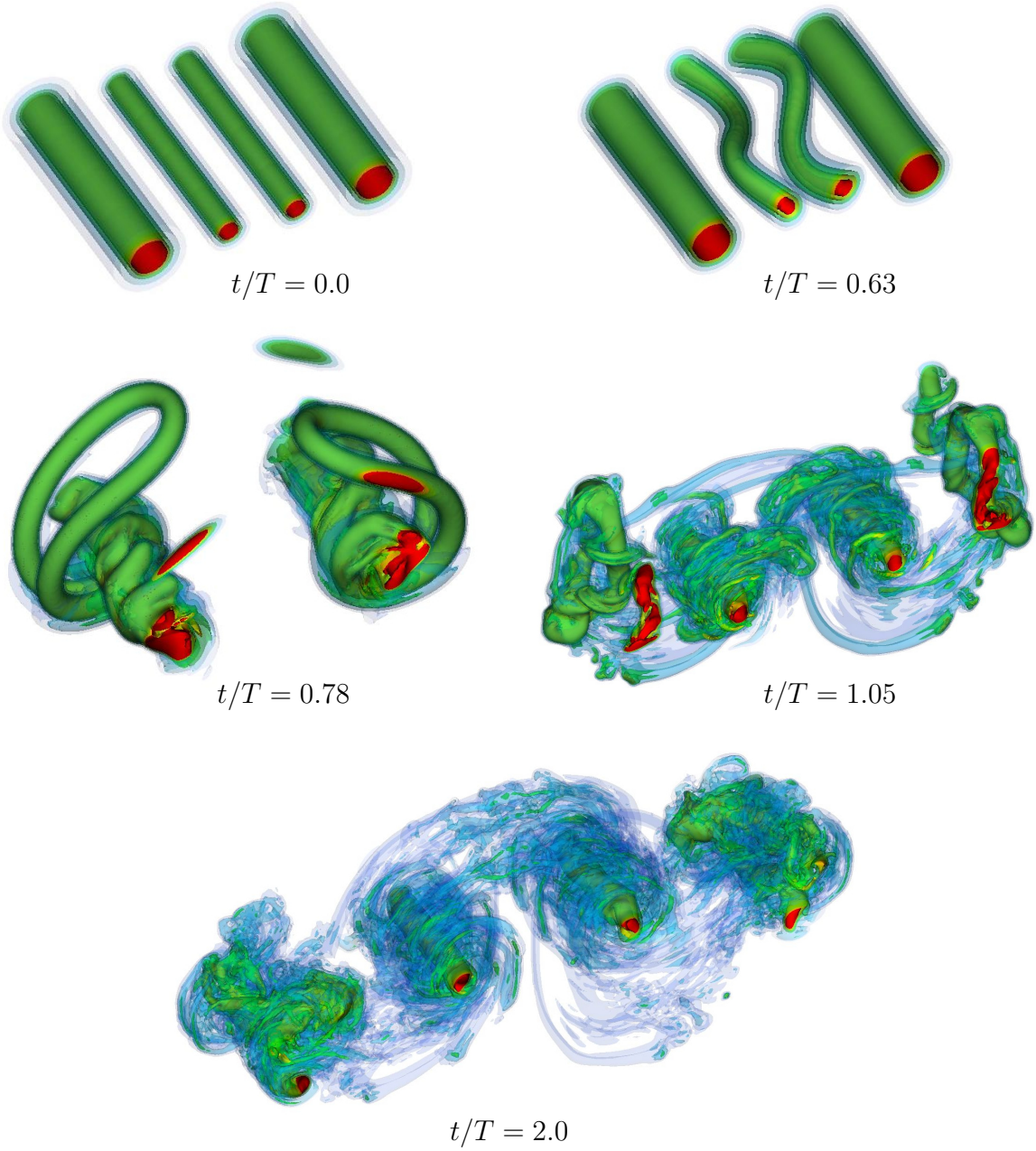

Figure 5.7: Isocontours of the vorticity magnitude from blue to red $|\boldsymbol{\omega} b_1^2/\Gamma_0| = [4, 16, 24, 32]$ at various times.

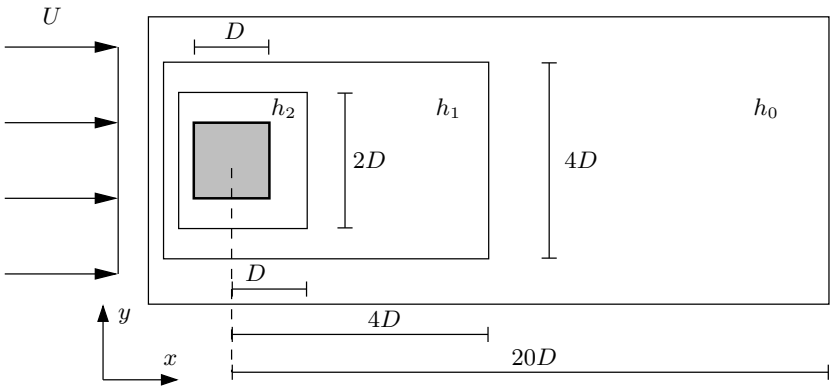

Figure 5.8: Sketch of the computational domain used to simulate the flow past a square cylinder at $\mathrm{Re} = 2.2 \times 10^4$. The extent of the domain is fixed in the x, z-direction whereas it is adapted to the immediate vorticity field in the y-direction. Resolutions are $h_0 = D/32$, $h_1 = D/64$ and $h_2 = D/128$. The domain length in the transverse direction is $L_z = 4D$. The coordinate system is showed shifted from its origin at the center of the square.

to approximately $\Delta y^+ = 5$ to 10 viscous wall units (Choi and Moin, 2012). The number of cells for the resulting mesh is approximately 7×10^7, for which half belongs to the mesh on the finest patch. Achieving $\Delta y^+ < 1$, which is the typical requirement for DNS or wall-resolved LES using refinement regions is therefore not realistic (Chapman (1978); Choi and Moin (2012) suggest $\Delta y^+ = 3$ to 10 but typically $\Delta y^+ < 1$ is used in practice, see e.g. Cao and Tamura (2016); Trias et al. (2015)). Near-wall modeling, based on the Reynolds-averaged Navier-Stokes equations (RANS) is typically used with $\Delta y^+ = 10$–100, which is more realistic with the current method. However to this authors knowledge, none has yet been tested for vortex methods. Further, such modeling would involve manipulation of the velocity (and vorticity) in the wall-normal directions, which is not in line with the penalization approach.

About 165 dimensionless time units was been resolved in both cases. On 192 cores of Intel E5-2650 v4 (2.20GHz) a single time unit required about 1 hour. About 20 penalization iterations were performed every time step.

5.5.2 Results

For $tU/D > 50$ the shedding is considered to have developed fully to a steady state, which is used to the compute statistics presented in the following. This interval corresponds to about 15 shedding cycles. The force coefficients cf. Eq. 4.17, have been plotted in Fig. 5.9. Mean values, root-mean-square (RMS) values and Strouhal numbers ($\mathrm{St} = fD/U$) for the two models are given in Tab. 5.1. The results are compared to what may be found in the literature.

Both models captures the shedding frequency; a value of $mathrmSt = 0.134$–0.136 is well within the range of the experiments and LES results and it compares excellently to that obtained from the DNS simulation. In general it seems as if the simple Smagorinsky model performs better than the dynamic model. The dynamic model under-predicts the mean drag and root-mean-square values by 8%–50% as compared to the DNS data. One explanation of this may be that the dynamic procedure is sensitive to distortion at the grid interfaces, which

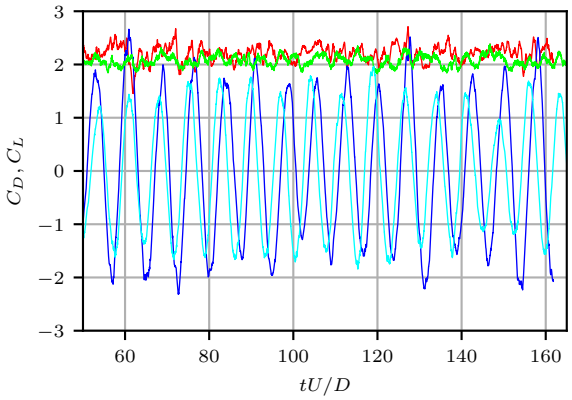

Figure 5.9: Evolution of drag and lift coefficients during approximately 15 shedding cycles in the time interval $tUD \in [50; 165]$ which has been considered as a steady harmonic state: C_D from SSM simulation (—) , C_L from SSM simulation (—) , C_D from DSM simulation (—) and C_L from DSM simulation (—) .

	$\bar{C}_D$	C'_D	C'_L	St
Current SSM	2.2	0.15	1.3	0.134
Current DSM	2.0	0.10	1.1	0.136
Experiments	2.05–2.16	0.22	1.2	0.12-0.14
DNS	2.18	0.21	1.7	0.132
LES	2.02–2.77	0.14–0.27	1.2–1.8	0.09–0.15

Table 5.1: Results for flow past a square cylinder at $\mathrm{Re} = 2.2 \times 10^4$ compared to literature. Experiments are reported for turbulence intensity in the inflow of up to 2%. The reference data has been taken from Lee (1975); Norberg (1993); Lyn and Rodi (1994); Atsushi (1982) (experiments), Trias et al. (2015) (DNS) and Sohankar et al. (2000); Rodi et al. (1997); Rodi (1997) (LES).

disturbs the formation of the vortices forming behind the cylinder.

Streamlines of the time-averaged field have been plotted in Fig. 5.10 for the two models and for DNS results by Trias et al. (2015). It may be seen that both models result in one large recirculation region behind the cylinder and a significant secondary region in agreement with the DNS profile. However, the elongation of the main recirculation region is for the current simulations over-predicted by a factor of 1.5 for SSM and 1.7 for DSM. The formation of a tertiary recirculation region near the leading edge, as may be observed from the DNS simulation, is most significant for the DSM simulation. It may also be noticed that in the current simulations, the streamlines penetrate the corners of the square cylinder, which are effectively rounded as a consequence of the penalization method used. Rounded corners are known to be associated with a decay in the mean and root-mean-square force coefficients and an increase in Strouhal number obtained. Tamura and Miyagi (1999) observed that for $\mathrm{Re} = 3 \times 10^4$ the mean drag coefficient decrease by 50% and the Strouhal number increase by 15% for rounded corners and a large rounding radius of $r/B = 1/6$, but reported nothing on the change in wake characteristics hereby.

The time-averaged velocity profiles in the boundary layer compares well to the experiments by Lyn et al. (1995) as shown in Fig. 5.11. From the profiles the inexact boundary condition is also apparent especially at the leading and trailing edges, where a slip-velocity is observed.

The difference between the simulation with the two different sgs stress models obtained is also clear from the phase averaged transverse vorticity plotted in Fig. 5.12. The SSM model results in phase averaged shear layers on both sides of the cylinder which appear thin and coherent, indicating a later break-up into a very turbulent wake as compared to the DSM results. This indicates that the DSM model is not dissipative enough in this region or that artificial disturbances are introduced with the dynamic formulation.

The time-average velocity and the velocity fluctuations along the centerline have been plotted in Fig. 5.13. Compared to experimental, LES and DNS data it may be seen that the time-averaged stream wise velocity on the centerline falls well within the range of the data, but that for both models, agreement is better with the experimental results. The velocity-fluctuations peak for $x/D \in [1; 3]$ as the references. The peak value for the stream wise fluctuations with the current SSM simulation is close to SSM simulation by Sohankar et al. (2000), whereas it is significantly under-predicted with the DSM model. This may be related to a less coherent near wake of the resolved field obtained with the current DSM formulation. In both cases the intensity of the fluctuations fails to decay in the far wake. One explanation of this behavior could be that numerical dissipation, e.g. from mesh level interfaces, obstructs the turbulent cascade independent of the sgs stress model and prevents break-down into small-scale motion. A visualization of the immediate vorticity field for a simulation with the simple Smagorinsky model is given in Fig. 5.14.

5.6 Summary

In this chapter LES with sgs stress models based on the Smagorinsky eddy viscosity ansatz were introduced and implemented in the VPM solver. A dynamic model with Lagrangian averaging, which is formally more accurate than a fixed coefficient model, was verified for problems of homogeneous turbulence. Here, the dynamic model was found to produce results in

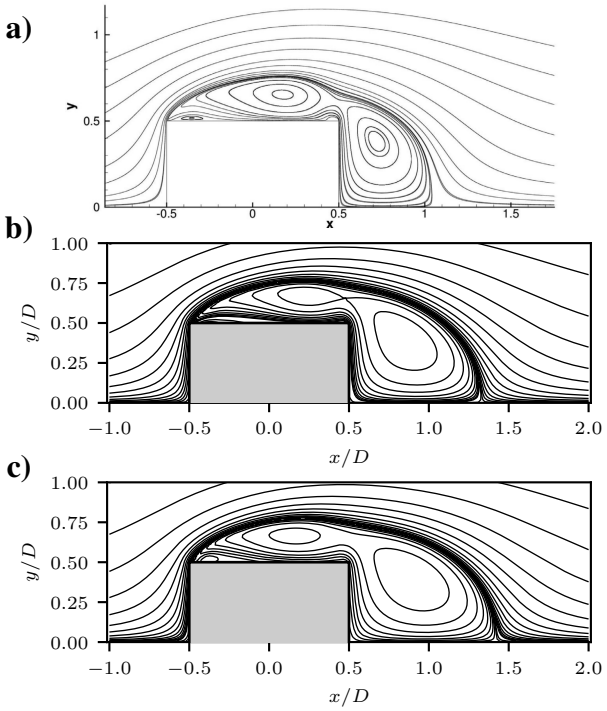

Figure 5.10: Time averaged streamlines: (a) DNS by Trias et al. (2015). (b) Current SSM simulation. (c) Current DSM simulation.

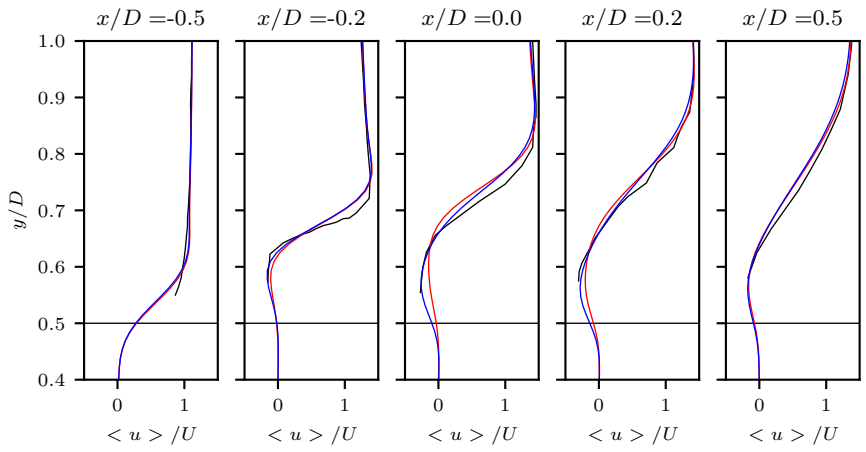

Figure 5.11: Mean streamwise velocity profiles in the boundary layer at various positions for the flow past a square cylinder at $\mathrm{Re} = 2.2 \times 10^4$: Experiment by Lyn et al. (1995) (—) , current SSM simulation (—) and current DSM simulation (—) .

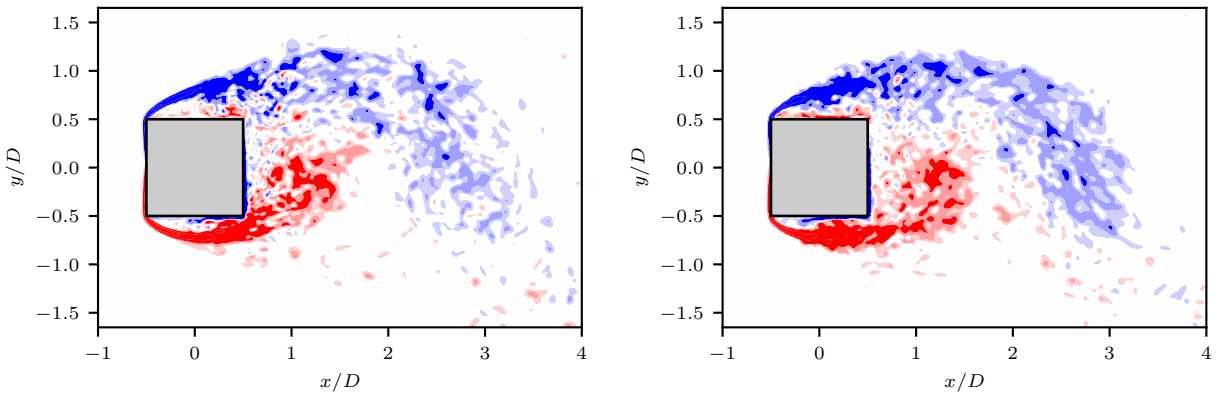

Figure 5.12: Transverse vorticity phase averaged over 15 cycles plotted in saturated colors from blue to red for $-8 < \langle \omega_z \rangle_p D/U < 8$

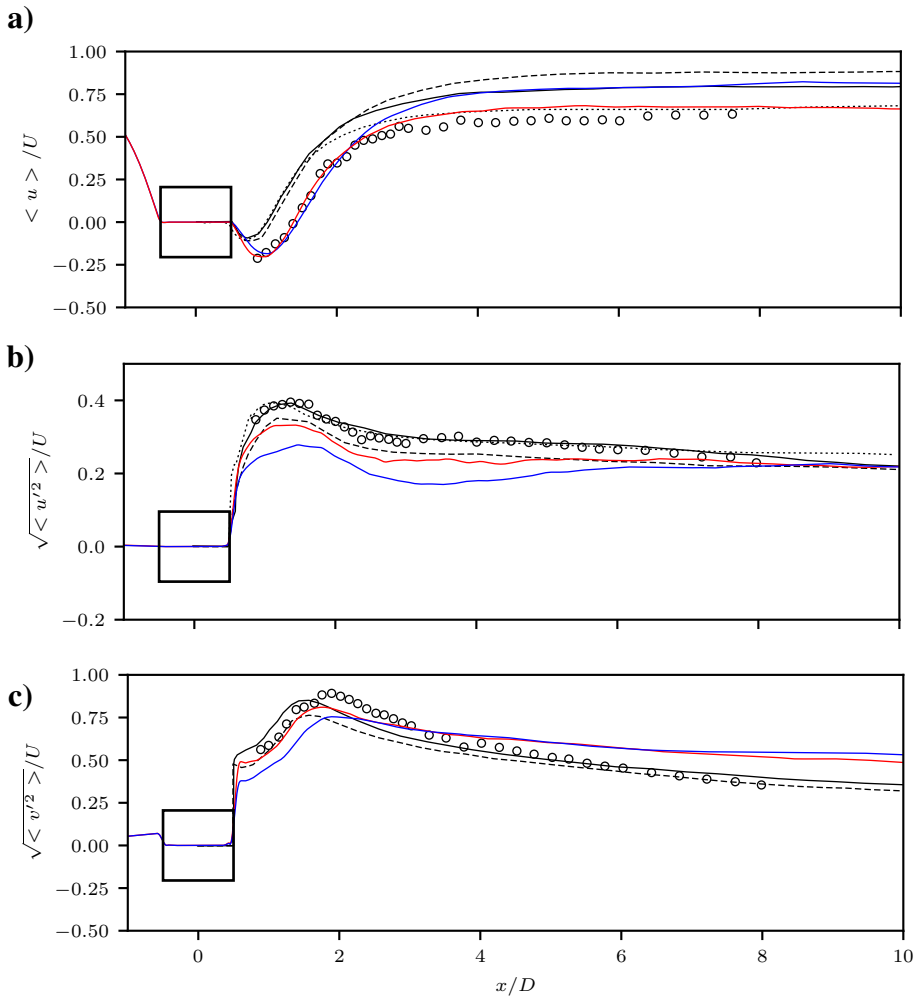

Figure 5.13: Velocity profiles along the wake center line for the flow past a square cylinder at $\mathrm{Re} = 2.2^4$: (a) Mean velocity. (b) Streamwise fluctuations. (c) Vertical fluctuations. Lines indicate results from SSM simulation by Sohankar et al. (2000) (—) , SSM simulation by Sohankar et al. (2000) (- - -) , DNS simulation by Trias et al. (2015) (·····) , experiment by Lyn et al. (1995) (○) , current SSM simulation (—) and current DSM simulation (—) .

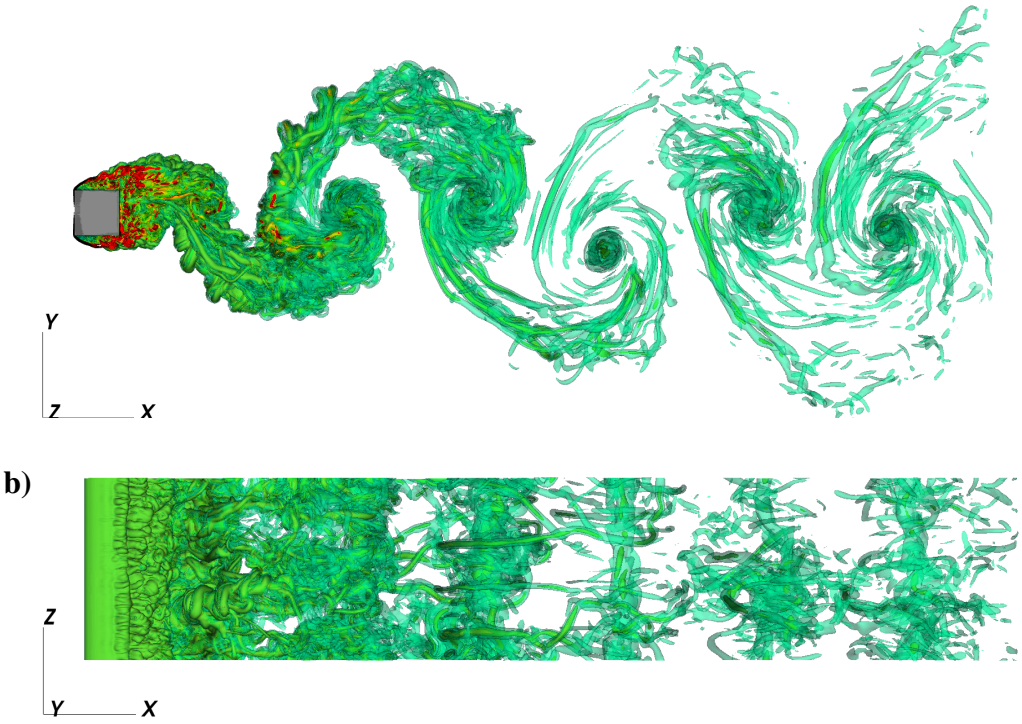

Figure 5.14: Isocontours of $|\boldsymbol{\omega}|D/U = [4, 8, 12, 16]$ from blue to red from SSM simulation at time $tU/D = 64.0$ at $\mathrm{Re} = 2.2^4$ (a) xy-view. (b) xz-view.

good agreement with theory and experiments. However, for bluff body flow simulation with the multiresolution formulation, the simple Smagorinsky model was seen to provide better results than the dynamic when compared to results from the literature. This is believed to be caused by artifacts from transitions between resolution levels and averaging of quantities along particle trajectories across these. However, also the simple model displayed vertical velocity fluctuations on the centerline in the far wake with a larger amplitude than reported in the references, which may indicate that the mesh level transitions disrupt the energy cascade to some degree here.

Chapter 6

Application of the method for prediction of aerodynamic flutter

Flutter is a type of aerodynamic instability which may be responsible for the structural failure of large scale structures subject wind loads if not suppressed. Flutter may be characterized as either one degree-of-freedom (1-DOF) torsional flutter and two degree-of-freedom (2-DOF) flutter. The later involves a coupling between the vertical and torsional motions. 1-DOF flutter results in a diverging torsional motion, which may be explained by unsteady separation of shear layers at the leading edge of the structure, which causes vortex motion along the length of the structure. For sufficiently high oncoming velocity, the oscillating moment induced by the detached vortices acts as a negative torsional damping of the dynamic system with cause diverging structural response. A condition for 2-DOF flutter is that the frequencies of the torsional and vertical motion of the dynamically loaded system become aligned. This is typically seen for slender smooth sections that are not unstable to 1-DOF flutter and may be accessed using inviscid theory by Theodorsen (1935) for the flat plate.

For a flexibly supported structure (with two degrees of freedom) subjected to oncoming flow cf. Fig. 6.1, the aerodynamic loading expressed in terms of force and moment coefficients

$$C_L = \frac{L}{\frac{1}{2}\rho U^2 B}, \qquad C_M = \frac{M}{\frac{1}{2}\rho U^2 B^2}, \tag{6.1}$$

is sometimes parameterized using a linear expression (Simiu and Scanlan, 1986)

$$C_L = 2\left[KH_1^*\frac{\dot{h}}{U} + KH_2^*\frac{B\dot{\theta}}{U} + K^2H_3^*\theta + K^2H_4^*\frac{h}{B}\right], \tag{6.2}$$

$$C_M = 2\left[KA_1^*\frac{\dot{h}}{U} + KA_2^*\frac{B\dot{\theta}}{U} + K^2A_3^*\theta + K^2A_4^*\frac{h}{B}\right]. \tag{6.3}$$

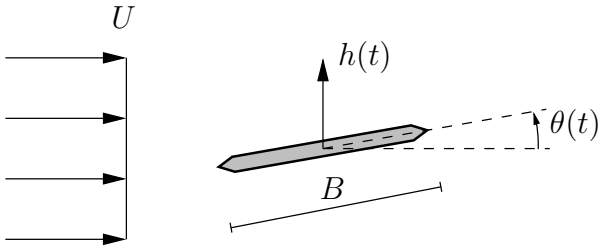

Figure 6.1: The cross section of an infinite period structure oscillating in heave $h(t)$ and $\theta(t)$ pitch motion.

Here, h is the vertical motion (heave), θ is the torsional motion about the center of mass (pitch) and $K = 2\pi\frac{fB}{U}$ is circular reduced frequency, with f being the frequency of the oscillation. The coefficients in the expressions cf. Eq. (6.2)–(6.3) are denoted the *aerodynamic derivatives* and depend only on the reduced velocity $U_r = U/fB$ and the shape of the structure. With Eqs.(6.2)–(6.3) it is possible to establish whether a structure is stable under a given loading from the equation of motion of a 2-DOF system using standard vibration analysis techniques. One way to extract the aerodynamic derivatives is by experimentally or numerically measuring force and moment coefficients when subjecting the structure to forced oscillations. Alternatively, the flutter onset velocity may be found by traversing the reduced velocity for the flexibly supported system. To be able to study flutter instability, rigid body motion is implemented into the present solver. This is done without projecting the translated and rotated characteristic function of the solid explicitly onto a mesh every time-step, which would require explicit smoothing of this. In stead rigid body motion is achieved by translating and rotating the penalization submesh (Fig. 3.2) relative to the background mesh. Fields are then transferred back and forth by interpolation using M_4' consistent with the particle-mesh interpolation.

6.1 Extraction of aerodynamic derivatives for a flat plate

A plate with sharpened edges and a length (B) to height (H) ratio of $B/H = 51.2$ is considered in a stationary configuration and in forced oscillations. This is done to establish the ability of the VPM penalization method to (1) simulate a laminar boundary layer (2) to verify the support of rigid body motion by comparison of extracted aerodynamic derivatives to those obtained with the inviscid theory of Theodorsen (1935). For this a computational setup as sketched in Fig. 6.2 is used. The resulting mesh consists of 10 cells across the height of the plate. Simulations are carried for adaptive time-stepping by third-order Runge-Kutta according to the Lagrangian time-step criterion with $C_{\text{LCFL}} = 0.125$. Further, to study whether 3D structures are able to develop in the boundary layer, fluctuations in the free-stream velocity are introduced by seeding vortex particles at the inlet corresponding to a turbulent intensity of 2%. The simple Smagorinsky sgs stress model is used to preserve stability in the wake at the moderate Reynolds numbers considered here. A re-projection of vorticity onto a divergence-free field is done every time-step.

6.1.1 Boundary layer of the flat plate

The flow past an infinitely thin stationary flat plate at moderate Reynolds number is characterized by a non-separated laminar boundary layer. In case of no perturbations such as surface roughness or noise in the free stream, the flow typically transitions to turbulence at $Re_x = Ux/\nu \approx 1 \times 10^6$, where x is the distance from the upstream edge of the plate. The natural transition occurs through 2D Tollmien-Slichting waves, which develops three dimensionality in terms of hairpin vortices that break down into fully developed turbulent boundary layer (Kundu et al., 2012; White, 2011). For so-called *by-pass transition* due to perturbations, such as fluctuations in oncoming free stream, the transition may occur already at $Re_x \approx 10^5$ (e.g. see numerical experiments by Zaki (2013)).

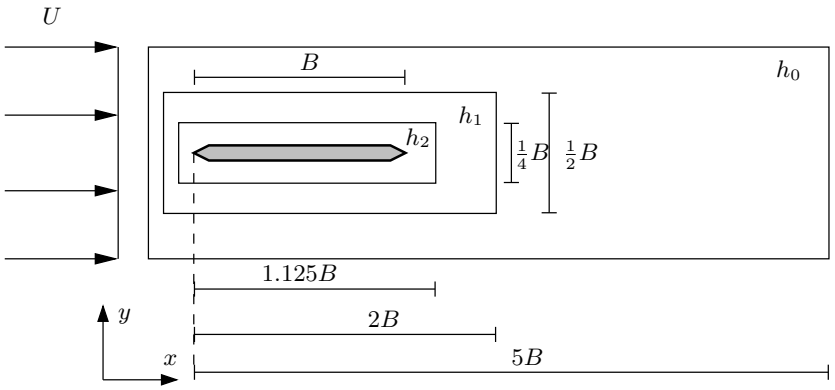

Figure 6.2: Sketch of the computational domain used to simulate the flow past plate of finite thickness. The extent of the domain is fixed in the x, z-direction whereas it is adapted to the immediate vorticity field in the y-direction. Resolutions are $h_0 = B/128$, $h_1 = B/256$ and $h_2 = B/512$. The domain length in the transverse direction is $L_z = 0.5D$. The coordinate system is shown shifted from its origin at the leading edge of the plate.

The laminar boundary layer solution was given by Blassius (see e.g. White (2011)) as a self similar velocity profile from which we can compare computed boundary layer thickness $\delta_{99\%}$ (defined as the thickness where the velocity reaches 99% of the free-stream), displacement thickness δ_1 and momentum thickness δ_2

$$\delta_{99\%}(x) = 5\sqrt{\frac{\nu x}{U}}, \tag{6.4}$$

$$\delta_1(x) = \int_0^\infty \left(1 - \frac{u(x)}{U}\right) \mathrm{d}y = 1.7208\sqrt{\frac{\nu x}{U}}, \tag{6.5}$$

$$\delta_2(x) = \int_0^\infty \frac{u(x)}{U}\left(1 - \frac{u(x)}{U}\right) \mathrm{d}y = 0.664\sqrt{\frac{\nu x}{U}}. \tag{6.6}$$

The flow is simulated for two Reynolds numbers $\mathrm{Re} = 10^4$ and $\mathrm{Re} = 10^5$. Six dimensionless time units are resolved and the first two are discarded before computing time averaged velocity profiles in the boundary layer. Visualizations of the immediate vorticity fields at $tU/B = 6$ are given in Fig. 6.3 for the final time. It may be seen that the imposed perturbations of the free-stream by a turbulent inlet intensity of 2% are insufficient to tricker a turbulent transition in the boundary layers in both cases and the boundary layer remain primarily 2D except for the presence of a 3D vortex wake forming behind the trailing edge. The boundary layer compares well to that of Blassius in case of $\mathrm{Re} = 10^4$ as seen in Fig. 6.4, whereas for $\mathrm{Re} = 10^5$ the thickness is highly over-predicted implying significant numerical diffusion (see Fig. 6.5). For the case $\mathrm{Re} = 10^4$ the boundary layer thickness at $x/B = 1$ is $20h_2$ and will thus be reasonably resolved at this point. For $\mathrm{Re} = 10^5$ it is only $x/B = 1$ is $8h_2$, implying that the mesh would need to be refined one or two times more for a good resolution, especially at upstream positions. The lack of resolution may also explain why significant 3D structures do not develop in the boundary layer as the effective viscosity is increased due to numerical diffusion.

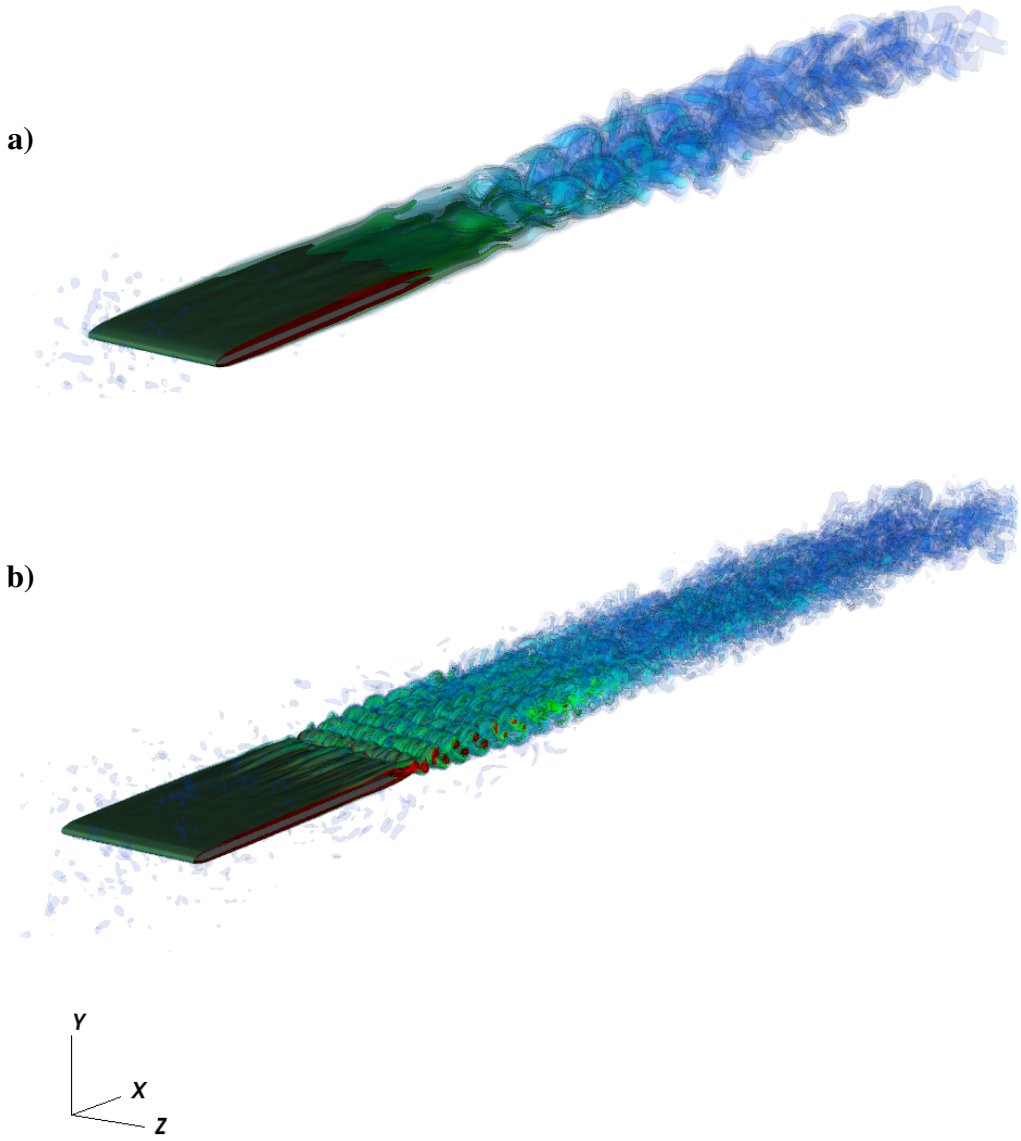

Figure 6.3: Isocontours of $|\boldsymbol{\omega}|B/U = [4, 8, 16, 32]$ from blue to red from simulation of flow past stationary flat plate at time $tU/B = 6.0$: (a) $\mathrm{Re} = 10^4$. (b) $\mathrm{Re} = 10^5$.

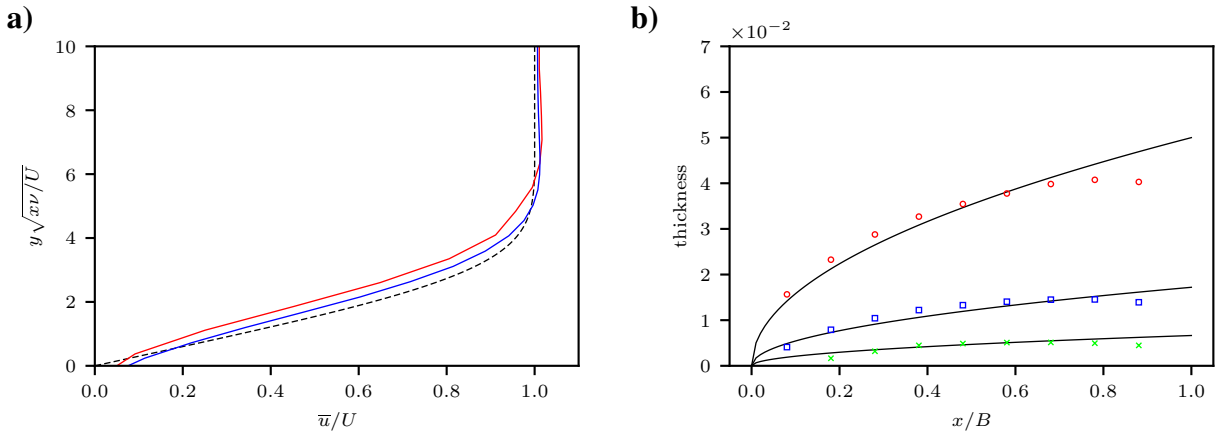

Figure 6.4: Flow past a stationary flat plate at $\mathrm{Re} = 10^4$: (a) Time-averaged velocity profile at $x/B = 0.28$ (—), $x/B = 0.68$ (—) and Blassius' solution (- - -). (b) Boundary layer thickness (○), displacement thickness (□), momentum thickness (+), and Blassius solution (—),

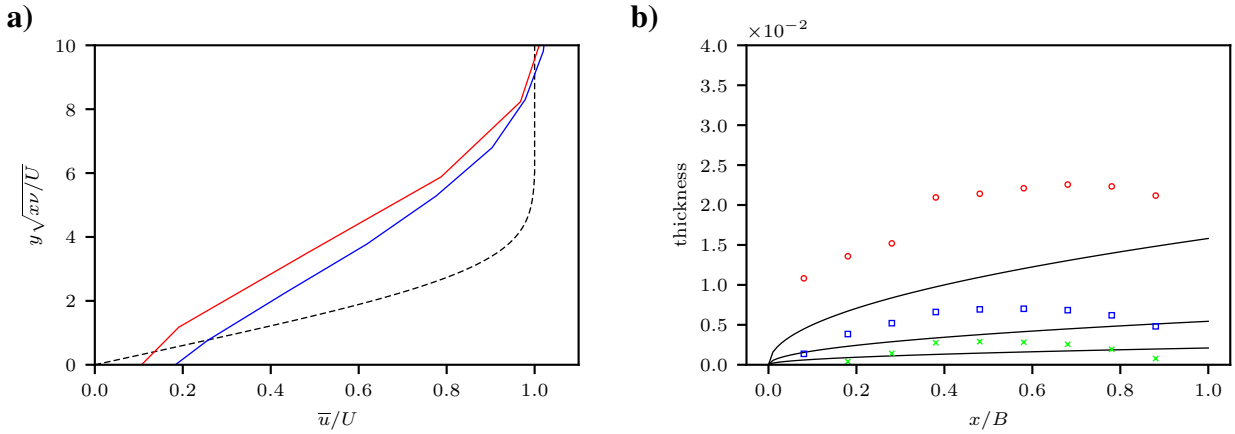

Figure 6.5: Flow past a stationary flat plate at $\mathrm{Re} = 10^5$: (a) Time-averaged velocity profile at $x/B = 0.28$ (—), $x/B = 0.68$ (—) and Blassius' solution (- - -). (b) Boundary layer thickness (○), displacement thickness (□), momentum thickness (+), and Blassius solution (—),

6.1.2 Aerodynamic derivatives extracted by forced oscillations

The aerodynamic derivatives are approximated by measuring the lift and moment of the structure when subjected to harmonic oscillations cf. Eq. (6.7) with amplitudes (A_h, A_θ). For every reduced velocity, and for a pure heave- and pitch motion respectively, the lift and moment force coefficients are approximated. The force and moment are modeled as the harmonic functions in Eq. (6.8) and the amplitudes (A_M, A_L) and phases (ϕ_M, ϕ_L) are fitted from the obtained signal.

$$h = A_h \sin\left(\frac{2\pi}{U_r}\frac{Ut}{B}\right), \qquad \theta = A_\theta \sin\left(\frac{2\pi}{U_r}\frac{Ut}{B}\right), \tag{6.7}$$

$$C_L = A_L \sin\left(\frac{2\pi}{U_r}\frac{Ut}{B} + \phi_B\right), \qquad C_M = A_M \sin\left(\frac{2\pi}{U_r}\frac{Ut}{B} + \phi_M\right). \tag{6.8}$$

By inserting the motions Eq. (6.7) and the models Eq. (6.8) into the linear expressions Eqs. (6.2)–(6.3) the aerodynamic derivatives are obtained as

$$H_1^* = \frac{A_L}{A_h/B}\frac{\sin(\phi_B)}{2K^2}, \qquad H_2^* = \frac{A_L}{A_\theta}\frac{\sin(\phi_B)}{2K^2}, \tag{6.9}$$

$$H_3^* = \frac{A_L}{A_\theta}\frac{\cos(\phi_B)}{2K^2}, \qquad H_4^* = \frac{A_L}{A_h/B}\frac{\cos(\phi_B)}{2K^2}, \tag{6.10}$$

$$A_1^* = \frac{A_M}{A_h/B}\frac{\sin(\phi_M)}{2K^2}, \qquad A_2^* = \frac{A_M}{A_\theta}\frac{\sin(\phi_M)}{2K^2}, \tag{6.11}$$

$$A_3^* = \frac{A_M}{A_\theta}\frac{\cos(\phi_M)}{2K^2}, \qquad A_4^* = \frac{A_M}{A_h/B}\frac{\cos(\phi_M)}{2K^2}. \tag{6.12}$$

The same setup as for the stationary flat plate is used to simulate forced oscillations for the flat plate at a Reynolds number of $\mathrm{Re} = 10^4$. The amplitudes of the forced motions are kept small so that separation of the boundary layer is avoided ($A_h/B = 0.05$ and $A_\theta = 3°$) as the aim is to compare the results to inviscid theory. A range of reduced velocities is swept $U_r \in [2; 12]$ and signals are taken after $0.5U/(U_rB)$ transients during two oscillation periods. The measured and fitted signals for $U_r = 4$ are plotted in Fig. 6.6. The high frequency content may be related to the small scale vortex shedding behind the plate due to the finite thickness of the plate.

The extracted derivatives are compared to those estimated using the inviscid theory by Theodorsen (1935). An overall good agreement is obtained, except when considering the cross damping coefficient H_2^*, which seems to diverge for increasing reduced velocity, likely an artifact from using a plate of finite thickness and a finite Reynolds number.

6.2 1-DOF flutter of H-shaped section

The sharp edges of a cylindrical structure with an H-shaped cross section similar to that of the first Tacoma Narrows Bridge, implies a separating flow at the trailing edge, which cause the von Karman vortex shedding. Additionally, flow separation at the leading edges and reattachment at the along the length of the section leads to 1-DOF flutter instability. This is similar to that of prismatic cylinders and channel shaped sections of moderate length (B) to height (H) ratios

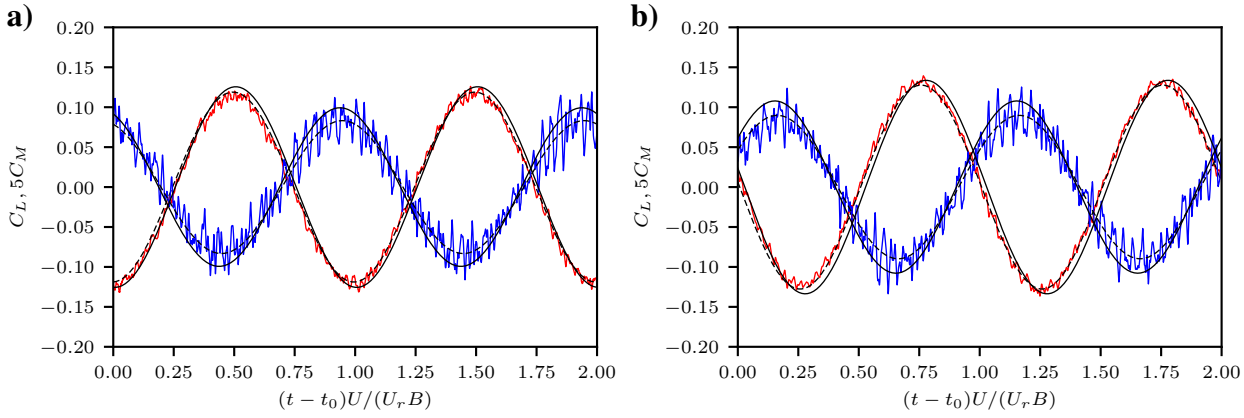

Figure 6.6: Comparison of measured force and moment coefficient with theoretical estimates for flat plate in forced oscillations at $\mathrm{Re} = 10^4$ and $U_r = 4$: (a) Heave. (b) Pitch. Lines indicate simulated lift (—), simulated moment (—), best fit (- - -), and estimates based on inviscid theory (—).

($B/H < 10$) (Matsumoto, 1996). An explanation of the mechanism behind the phenomena is given e.g. by Larsen and Larose (2015) and is related to the position of the vortex center in relation to the center of mass of the structure. Whether a structure is unstable to 1-DOF flutter may be established by considering the aerodynamic derivatives introduced in Sec. 6.1. If the aerodynamic (negative) damping in torsion A_2^* exceeds the structural damping of the system, the torsional motion will increase exponentially. For the case of the plate (a slender prism with $B/H = 50$) $A_2^* < 0$ was obtained, hence it is not unstable to 1-DOF flutter. For small angles of attack the boundary layer of the plate does not separate and reattach, hence vortex convection along the length of the plate is avoided. It is reported for H-shaped sections that A_2^* becomes positive at a reduced velocity, which is about constant for slenderness ratios ($B/H < 10$) as $U_r = 2$ (Scanlan, 1978). In this section free torsional oscillations of an H-shaped section with slenderness ratio $B/H = 5$ is carried out at various reduced velocities and compared to this limit. Initially the stationary loads are obtained and compared to results from the literature.

6.2.1 Stationary loads

A simulation is carried out for $\mathrm{Re} = 10^4$ and the stationary configuration sketched in Fig. 6.8 using time stepping by second order Runge-Kutta scheme with time-step size adapted according to Lagrangian criteria with $C_{LCFL} = 0.5$. As for the flat plate, the simple Smagorinsky subgrid stress model is used for LES modeling and vorticity re-projection is done every time-step. The simulated force coefficients defined as Eq. (6.1) are given in Fig. 6.9. Mean drag and dimensionless shedding frequency $\mathrm{St} = fH/U$ are computed from the signals in the time interval $tU/B \in [20; 100]$, which is considered as a steady oscillatory phase of the flow. The values, which have been listed in Tab. 6.1, compare well to those reported for wind tunnel experiments in Larsen and Walther (1997). The separated shear layers disturb the von Karman shedding pattern as seen from the immediate vorticity field at $tU/B = 30$ in Fig. 6.10, which may explain

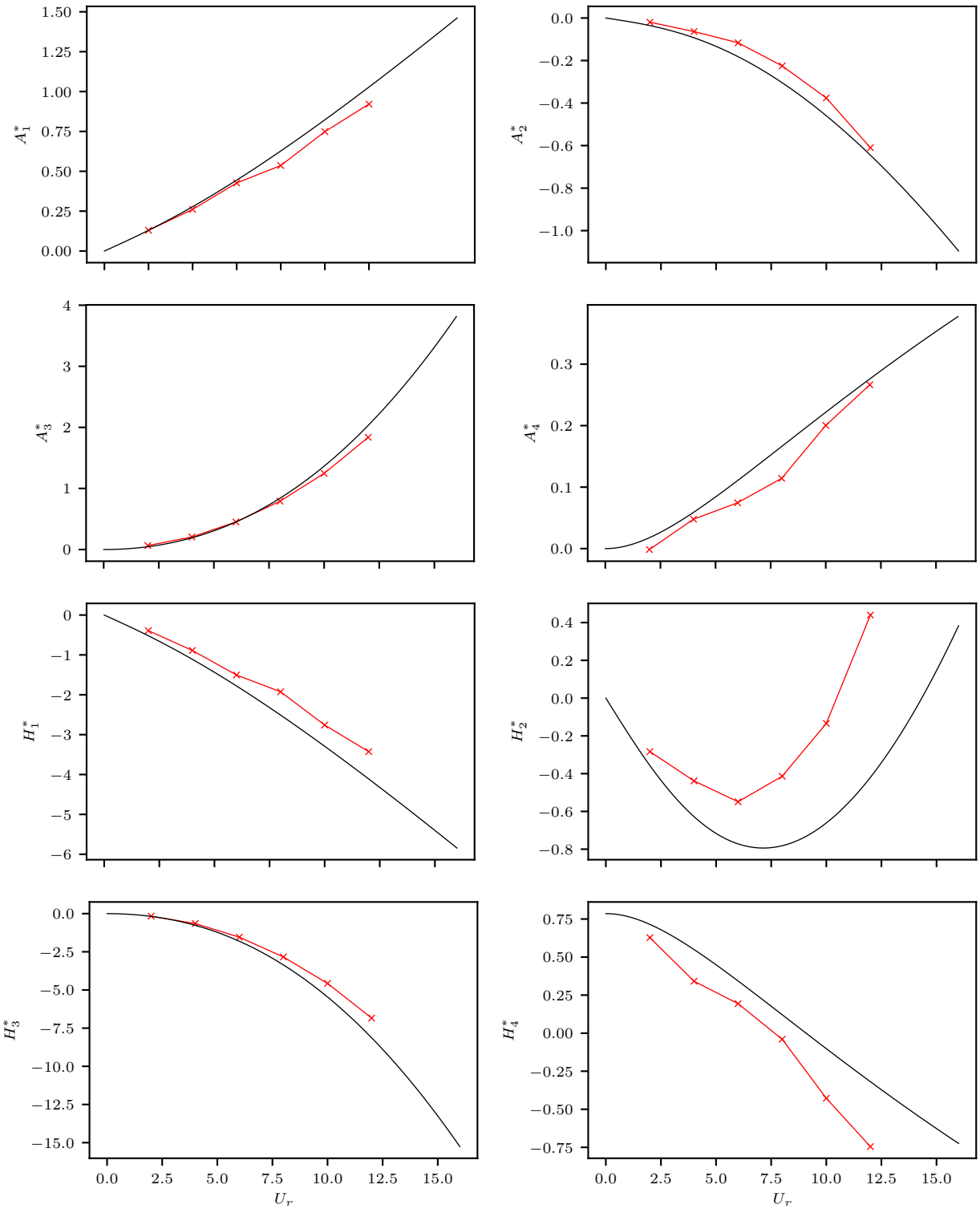

Figure 6.7: Aerodynamic derivatives of the flat plate as function of reduced velocity: Simulated (-×-) and theoretical estimates by Theodorsen (1935) (—)

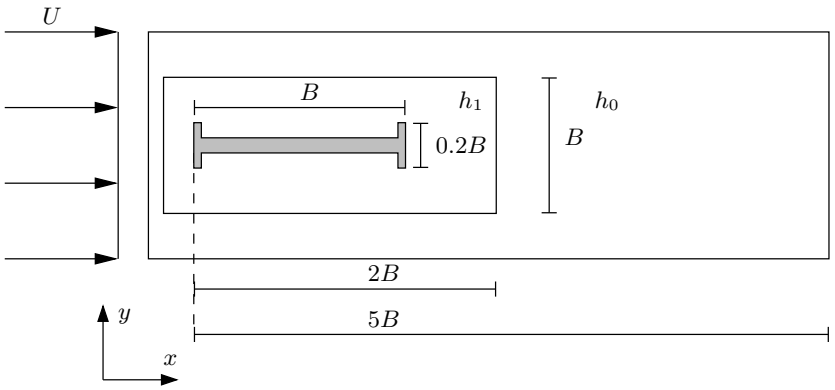

Figure 6.8: Sketch of the computational domain used to simulate the flow past H-shaped section. The extent of the domain is fixed in the x, z-direction whereas it is adapted to the immediate vorticity field in the y-direction. Resolutions are $h_0 = B/128$, $h_1 = B/256$. The domain length in the transverse direction is $L_z = 1L$. The coordinate system is displayed shifted from its origin being the center of section. The thickness of the center plate is $0.06B$ and the thickness of the end plates is $0.02B$.

	Simulation	Experiment
St	0.12	0.115
$\bar{C}_D$	0.28	0.24-0.30
C'_D	0.03	-
C'_L	0.19	-

Table 6.1: Mean and root-mean-square simulated force coefficients and Strouhal number $\mathrm{St} = fH/U$. Also experimental values presented in Larsen and Walther (1997).

the unsteadiness in the signals and presence of time scales slower the one associated with the von Karman shedding.

6.2.2 Flexibly supported section

Free oscillations in pure torsion are simulated by solving the equation of motion of an undamped 1-DOF torsional oscillator along with the flow problem

$$I_m\ddot{\theta} + k_\theta\theta = M, \tag{6.13}$$

where I_m is the mass moment-of-inertia and k_θ is torsional stiffness. Eq. 6.13 is discretized using forward Euler

$$\dot{\theta}^{n+1} = \dot{\theta}^n + \Delta t(M^n - k_\theta\theta^n)/I_m, \tag{6.14}$$

$$\theta^{n+1} = \theta^n + \Delta t\dot{\theta}^n, \tag{6.15}$$

where n is the time-step number. A sequential coupling between the flow problem and the structural problem is applied, as the time scale of the structural dynamics is assumed to be much slower than those of the smallest dynamics of the resolved flow.

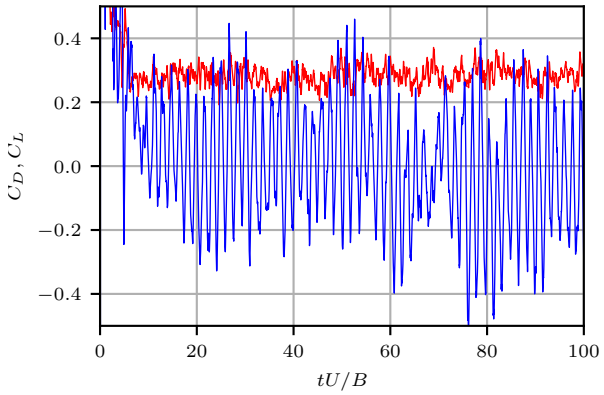

Figure 6.9: Flow past stationary H-shaped section: Evolution of drag (—) and lift (—) coefficients.

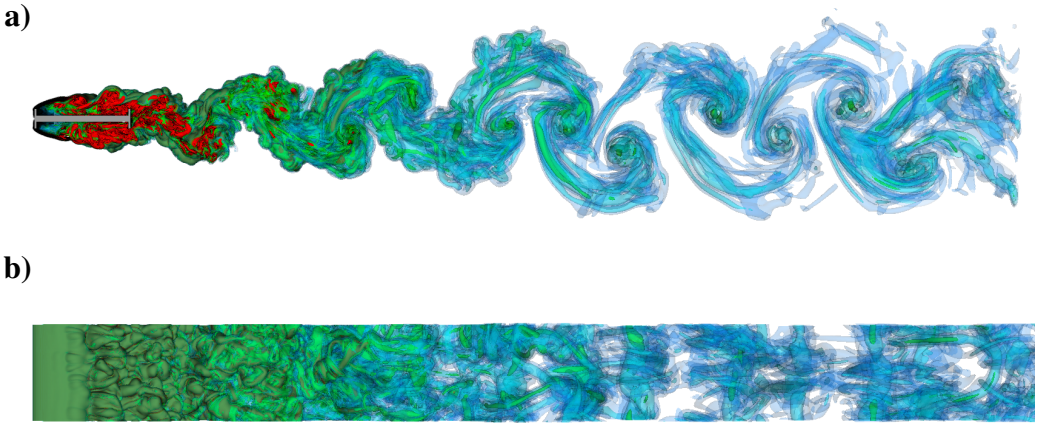

Figure 6.10: Isocontours of $|\boldsymbol{\omega}|B/U = [4, 8, 12, 16]$ from blue to red in simulated flow past stationary H-Shaped section at time $tU/B = 30.0$ at $\mathrm{Re} = 10^4$: (a) xy-view. (b) xz-view.

For comparison with the first Tacoma Narrows Bridge, and model experiments of this, a scaling criteria (Simiu and Scanlan, 1996) implies that a moment of inertia should be used, which is estimated from values given by Larsen et al. (2000) as

$$I_m/(\rho B^2) = 7.143. \tag{6.16}$$

To achieve a certain reduced velocity the stiffness coefficient is varied as

$$U_r = \frac{U}{f_n B} \Rightarrow k_\theta(U_r) = \left(\frac{2\pi}{BU_r}\right)^2 I_m, \tag{6.17}$$

where $f_n = \frac{1}{2\pi}\sqrt{\frac{k_\theta}{I_m}}$ is undamped natural frequency of the system.

The results of four simulations for reduced velocities $U_r = 2, 3, 4, 5$ are presented in Fig. 6.11. The solid is initialized with $\theta = -5^\circ$ and $\dot{\theta} = 0$. For reduced velocity $U_r = 2$ the motion is dampened by aerodynamic moment, whereas for $U_r = 3$ the oscillation amplitude is approximately constant and it increase for $U_r = 4, 5$. The results imply that the onset reduced velocity is $3 < U_r|_{\text{crit}} < 4$ which is above the experimental value $U_r|_{\text{crit}} = 2$ but closer than the numerical result that was also reported in Larsen and Walther (1997) as $U_r|_{\text{crit}} = 4$. This could be a Reynolds number effect, as the Reynolds number of experiments are one to two orders of magnitude larger that the one used for the current simulations. The qualitative explanation of the diverging oscillation amplitude at reduced velocity above the onset velocity may be obtained by considering the motion of the detached vortices generated by the separated shear layer at the leading edge as illustrated in Fig. 6.12. The axial vorticity averaged in z-direction is plotted at six instances during an half an oscillation cycle. As the cross section goes from $\theta = 0$ to $\theta < 0$ (from point 1 to point 2) a vortex is formed behind the leading edge above the section, which travels along the length of the section and reaches a point approximately above its center of mass a quarter period through the cycle (point 3). During this quarter cycle the vortex has applied a negative aerodynamic moment as it has been traveling toward the center of the section. Similarly as the vortex travels away from the center (point 1–6) during the second quarter cycle it generates a positive moment. Below the section the motion of this vortex generates a moment of the same sign, because the cycle is shifted half a period and it has circulation of opposite sign. The reader is referred to Larsen and Larose (2015) for further details on this.

6.3 Summary

In this chapter the VPM method with Brinkman penalization and sgs stress modeling was applied for numerical experiments regarding aerodynamic instability. Rigid body motion was used with the penalization technique by translating and rotating the mesh of the penalization subdomain relative to the background mesh. The approach was verified for a plate of finite thickness which aerodynamic derivatives were extracted by the method of forced oscillations. These compared well with theoretical estimates based on inviscid theory. Furthermore, an H-shaped section was flexibly supported and subject to an oncoming flow. 1-DOF torsional flutter was observed and the onset reduced velocity was identified to be in the range $3 < U_r|_{\text{crit}} < 4$. Although this result deviates by 50%–100% from experimental findings ($U_r|_{\text{crit}} = 2$), the studies demonstrated the versatility of the presented method.

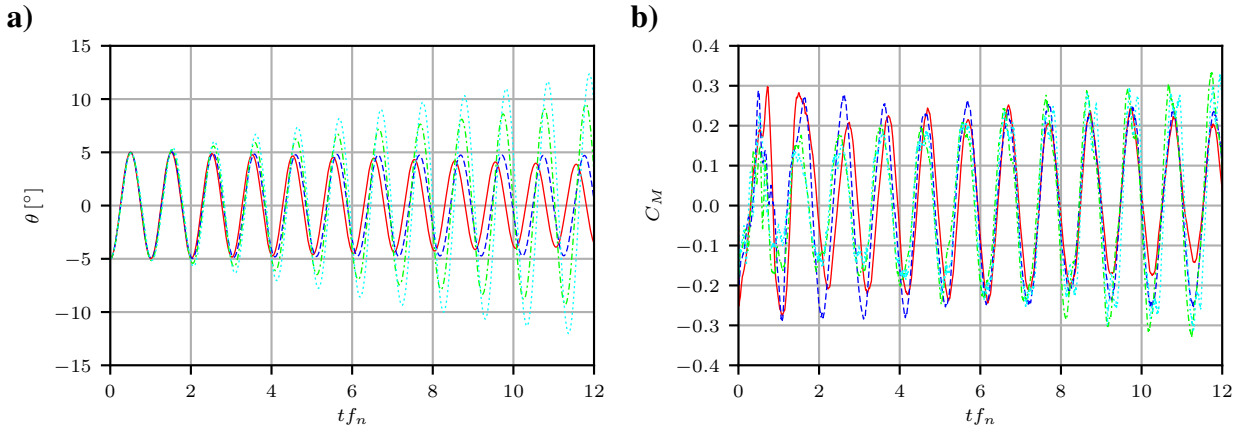

Figure 6.11: Time history of pitch (a) and moment coefficient (b). Lines indicate simulation for reduced velocities $U_r = 2$ (—) , $U_r = 3$ (- - -) , $U_r = 4$ (-·-) and $U_r = 5$ (···) .

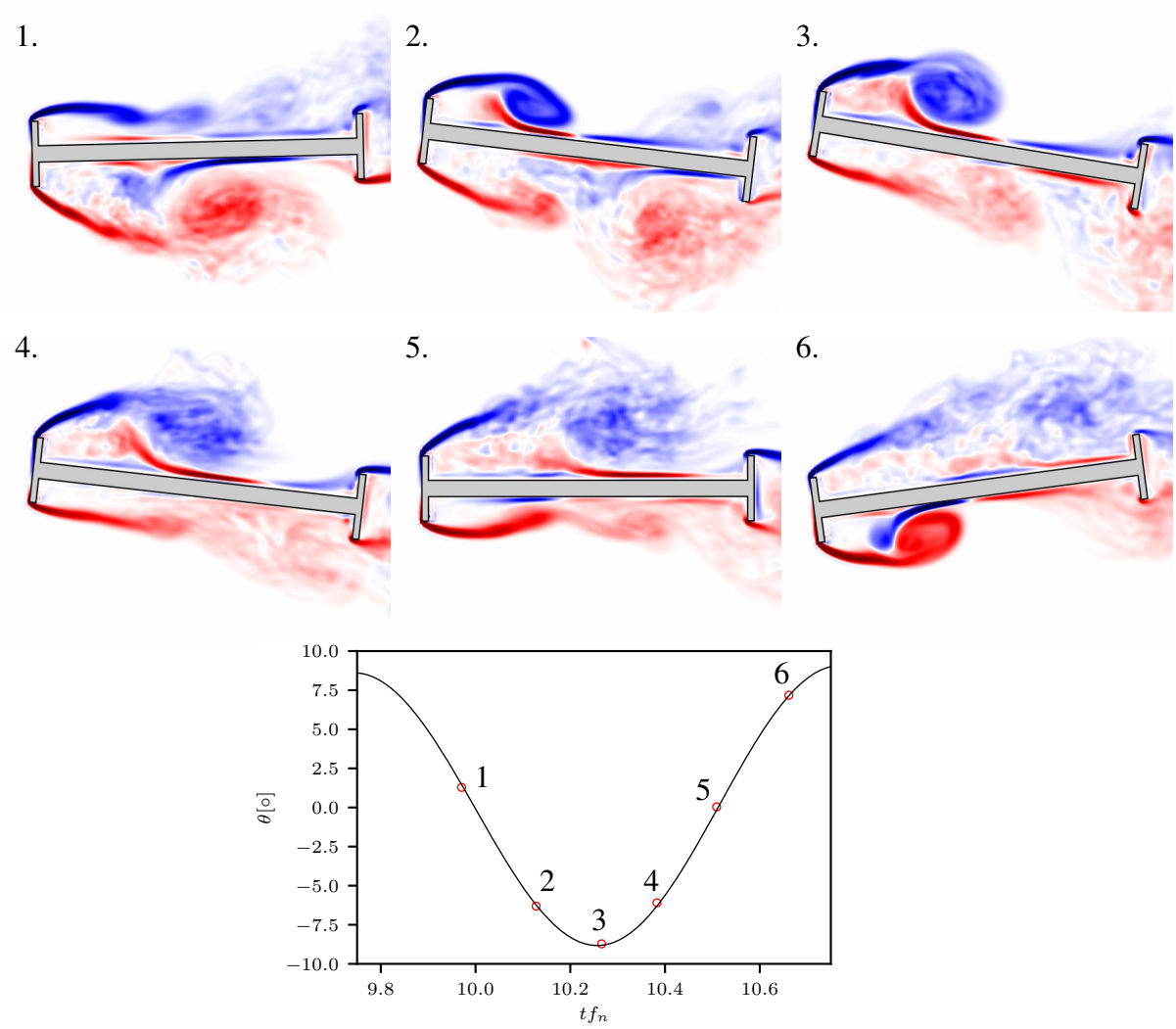

Figure 6.12: Simulated axial vorticity component (ω_z) averaged in the z-direction and plotted at 6 times during an oscillation cycle as indicated on the graph showing the rotation angle as function of time for $U_r = 4$. Colors indicate $\langle\omega_z\rangle_z UB \in [-64 : 64]$ from blue to red.

Conclusions

This dissertation has presented contributions to vortex-particle mesh methods in 3D. One contribution is the derivation and implementation of a parallel, scalable Poisson solver based on regularised Green's functions for any mixture of free-space, periodic and homogeneous Dirichlet or Neumann boundary conditions. This solver is relevant also in other branches of computational physics such as cosmology and molecular dynamics.

The application in this dissertation has been bluff body aerodynamics using Brinkman penalization and a variation of the Poisson solver enabling local mesh refinements, with an emphasize on periodic structures. The Brinkman penalization was used in an iterative formulation for increased accuracy and was extended to handle rigid body motion. The consistency of the combined method was demonstrated for low Reynolds number flows and the method was tested in turbulent flow as well.

Problems at moderate Reynolds numbers was considered through large-eddy-simulation. Here, the simple Smagorinsky model and dynamic variation of this were proposed as subgrid-scale stress models. In the spirit a particle methods, the dynamic Smagorinsky model was used with Lagrangian averaging and test filters were chosen consistently with the regularization used for obtaining smooth Green's function solutions to the Poisson equation. The consistency of the dynamic model was demonstrated for benchmark problems of forced and decaying isotropic turbulence.

Although the combined approach applied for bluff body aerodynamics at moderate Reynolds number yielded results which compared qualitatively well with results found in the literature, the numerical experiments also highlighted several challenges. Among these are: (1) The resolution of turbulent boundary layers in wall-resolved LES is not possible since the vortex method relies on locally isotropic meshes. (2) The poor adaptivity of the multiresolution method in its present form and numerical diffusion at interfaces. (3) Inefficiency of the iterated Brinkman penalization, which constitute a major part computational efforts of the combined solver.

The obvious way to overcome the first point would be to account for bodies through reduced order models, thereby not resolving turbulent boundary layers, or to use wall modeling. Wall-modeling however, is not in line with the simplicity of the Brinkman penalization technique, which conveniently avoids manipulation of the solution near the solid interface, which may be required when reconstructing the unresolved boundary layer.

For the second point, the use of the refinement patches in a block structured framework would enhance the adaptivity. The accuracy at the mesh interfaces still needs to be addressed and possibly more optimal interpolation schemes would need to be used for increased efficiency and accuracy, when super-positioning solutions across levels. Further, the support of the refinement patches must be kept sufficiently low for the sake of inter-processor communication.

Regarding the third point, the Brinkman method is easy to implement and use, however other schemes based on immersed interfaces or domain decomposition methods may formally be more accurate and efficient.

Appendix

Appendix A

Regularized Green's functions in 1D

The 1D Poisson for the regularization function (ζ_m) being the inverse Fourier transform of Eq. (1.21) is derived by radial integration of

$$\frac{d^2 G_m}{dr^2} = -\zeta_m(r), \tag{A.1}$$

as

$$G_m(r) = -\sigma \left(\frac{1}{2} \operatorname{erf}\left(\rho \frac{\sqrt{2}}{2} \right) \rho + P_m \frac{1}{\sqrt{2\pi}} \exp\left(-\frac{1}{2}\rho^2 \right) \right), \tag{A.2}$$

where erf is the error-function defined as

$$\operatorname{erf}(x) = \frac{2}{\sqrt{\pi}} \int_0^x \exp\left(-t^2\right) \, \mathrm{d}t \tag{A.3}$$

and P_m is a polynomial depending on the order of the regularization function

$$P_2 = 1 \tag{A.4}$$

$$P_4 = \frac{1}{2} \tag{A.5}$$

$$P_6 = \frac{1}{8}\left(\rho^2 + 3\right) \tag{A.6}$$

$$P_8 = -\frac{1}{48}\left(\rho^4 - 12\rho^2 - 15\right) \tag{A.7}$$

$$P_{10} = \frac{1}{384}\left(\rho^6 - 23\rho^4 + 141\rho^2 + 105\right). \tag{A.8}$$

The regularized 1D kernel for various m was been plotted in Fig. 1.2(a).

Appendix B

Discrete Transforms

B.1 The Discrete Fourier Transform

The discrete analogy to the continuous Fourier Transform pair cf. Eq. (1.9) and Eq. (1.10) is formally derived by considering the expansion of a 2π-periodic function (f) in a basis of complex exponential functions (a Fourier series expansion)

$$f(x) = \sum_{k=-\infty}^{\infty} \widehat{f}_k e^{\iota k x}. \tag{B.1}$$

Since the basis functions are orthogonal on the interval $x \in [0; 2\pi]$, the coefficients in Eq. (B.1) may be determined as

$$\frac{1}{2\pi} \int_0^{2\pi} f e^{-\iota k x} \, \mathrm{d}x = \widehat{f}_k, \tag{B.2}$$

which corresponds to the Fourier Transform of the continuous function. Approximation of Eq. (B.2) using the trapezoidal rule applied for the function sampled at the equidistant grid points $x_j = \frac{2\pi}{N} j$, $j = 0...N-1$ results in the *discrete Fourier coefficients*

$$\tilde{f}_k = \frac{1}{N} \sum_{j=0}^{N-1} f_j e^{-\iota k x_j}. \tag{B.3}$$

Sampling in real-space implies periodicity in Fourier-space. E.g. a function $a(x)$ sampled at grid points $x_n = nh$, for $n \in \mathbb{Z}$

$$a_n = a(x_j) = a(x) \sum_{n=-\infty}^{\infty} \delta(x - nh). \tag{B.4}$$

can be rewritten by substituting the impulse train for its Fourier series expansion as

$$a_n = a(x) \frac{1}{h} \sum_{n=-\infty}^{\infty} e^{\iota n \frac{2\pi}{h} x}. \tag{B.5}$$

The continuous Fourier transform of this cf. Eq. Eq. (1.9) is

$$\widehat{a}_s(k) = \frac{1}{h} \sum_{n=-\infty}^{\infty} \frac{1}{2\pi} \int_{-\infty}^{\infty} a(x) e^{-\iota [k - n\frac{2\pi}{h}] x} \, \mathrm{d}x = \frac{1}{h} \sum_{n=-\infty}^{\infty} \widehat{a} \left(k + n \frac{2\pi}{h} \right), \tag{B.6}$$

which implies replication of the Fourier transform about the wavenumber $2\pi/h$. Similarly, the sampling associated with the quadrature in Eq. (B.3) reflects this behavior in the discrete coefficients. Using a result from Kopriva (2009)

$$\frac{1}{N}\sum_{j=0}^{N-1} e^{\iota(m-k)\frac{2\pi}{N}j} = \delta_{m-k,\pm pN}, \qquad \text{for } p \in \mathbb{Z} \tag{B.7}$$

a relation between the discrete Fourier coefficients and the true Fourier coefficients (for the continuous function) are obtained upon inserting the expansion of f in Eq. (B.3)

$$\tilde{f}_k = \frac{1}{N}\sum_{j=0}^{N-1}\left[\sum_{m=-\infty}^{\infty}\widehat{f}_m e^{\iota m x_j}\right] e^{-\iota k x_j} = \sum_{m=-\infty}^{\infty}\widehat{f}_m\left[\frac{1}{N}\sum_{j=0}^{N-1} e^{\iota(m-k)\frac{2\pi}{N}j}\right] \tag{B.8}$$

$$= \sum_{p=-\infty}^{\infty}\widehat{f}_{k+pN}. \tag{B.9}$$

From Eq. (B.8) it is directly seen:

- The discrete coefficients are N-periodic ($\tilde{f}_k = f_{k+pN}$ for $p \in \mathbb{Z}$).
- The discrete coefficients are exact ($\tilde{f}_k = \widehat{f}_k$) if $f(x) = \sum_{k=-N/2}^{N/2}\widehat{f}_k e^{\iota k x}$, otherwise they are aliased by higher order terms of the series.

It may be shown (Kopriva, 2009) that the function (N is even)

$$I_N f(x) = \sum_{j=-N/2}^{N/2}\frac{\tilde{f}_k}{c_k}e^{\iota k x}, \qquad c_k = \begin{cases} 1/2 & \text{for } k = \pm N/2 \\ 1 & \text{otherwise} \end{cases} \tag{B.10}$$

interpolates f with the cardinal property ($I_N f(x_j) = f(x_j)$ for $j = 0, 1, ..., N-1$).

N-periodicity of the coefficients implies that ($\tilde{f}_{-N/2} = \tilde{f}_{N/2}$). Hence Eq. (B.10) can be written

$$I_N f(x) = \sum_{j=N/2}^{N/2-1}\tilde{f}_k e^{\iota k x}. \tag{B.11}$$

The derivative of f may be approximated by differentiation of the interpolant (Eq. (B.10)) as in Eq. (B.12)

$$\frac{d^n}{dx^n}\left\{I_N f(x)\right\} = \sum_{j=-N/2}^{N/2}(ik)^n\frac{\tilde{f}_k}{c_k}e^{\iota k x}\begin{cases} \sum_{j=-N/2+1}^{N/2-1}(ik)^n\tilde{f}_k e^{\iota k x} & \text{for } n \text{ odd} \\ \sum_{j=-N/2}^{N/2-1}(ik)^n\tilde{f}_k e^{\iota k x} & \text{for } n \text{ even.} \end{cases} \tag{B.12}$$

Eq. (B.3) and Eq. (B.11) evaluated at the quadrature nodes correspond to the forward and inverse DFT (often multiplied by a scaling factor):

$$\tilde{f}_k = \sum_{j=0}^{N-1} f_j e^{-\iota k\frac{2\pi}{N}j}, \qquad k = -N/2, ..., N/2-1 \tag{B.13}$$

$$f_j = \frac{1}{N}\sum_{k=N/2}^{N/2-1}\tilde{f}_k e^{\iota k\frac{2\pi}{N}j}, \qquad j = 0, ..., N-1. \tag{B.14}$$

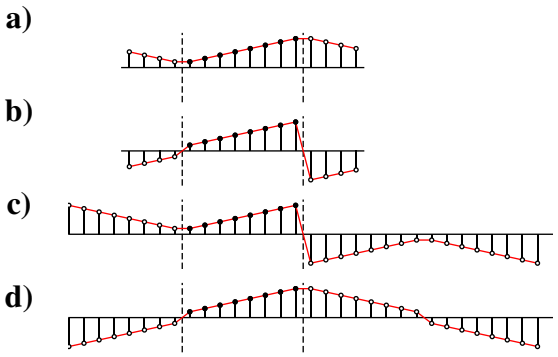

Figure B.1: The DTT of a sequence of length N (filled markers) is derived from the DFT of a symmetrically extended sequence (filled and unfilled markers) of either $2N$ for transforms of type 2 or $4N$ for transforms of type 4. By convolution with an radial symmetric Green's function the output has the same symmetry as implied by the transform of the input (Martucci, 1994), which impose boundary conditions at domain exterior (- -) : (a) DCT-2. (b) DST-2. (c) DCT-4. (d) DST-4.

The discrete transforms may be used to evaluate the derivative as Eq. (B.12) at the quadrature nodes by pre-multiplying the discrete coefficients with $(ik)^n$ and by zeroing the $\tilde{f}_{-N/2+1}$ for n odd before applying the IDFT .

For convenience $\widehat{f_k}$ will be used to denote both continuous Fourier coefficients and discrete Fourier coefficients keeping in mind the principal difference between the two, as emphasized in this section.

The summations in Eqs. (B.13)–(B.14) implies that $\mathcal{O}(N^2)$ operations are required to compute a DFT or an IDFT of an N-point sequence. A rapid evaluation procedure known as the Fast Fourier Transform (FFT) reduces the operations to $\mathcal{O}(N \log(N))$, which is reason that Fourier based methods are practical for numerical simulation. FFT algorithms are widely available in various software-libraries; In this work the implementation relies on algorithms from the Intel Math Kernel Library (MKL) through the library's FFTW wrappers (Frigo and Johnson, 2005) for compatibility with free open-source software.

B.2 The Discrete Trigonometric Transforms

In some cases it may be useful to assume a symmetry of the sequences transformed, e.g. for imposing boundary conditions as illustrated in Fig. B.1. Such an implied symmetry leads to the definition of real valued Discrete Trigonometric Transforms (DTTs). The DTTs used in the current work are derived from the DFT in following. Each of the N-point DTTs has a fast algorithm based on the FFT requiring computational efforts no worse than a $2N$-point FFT (Frigo and Johnson, 2005).

B.2.1 DCT-2

Forward transform

Consider the special case of an even symmetric extension of the N-point real sequence x_n as

$$y_n = \begin{cases} x_n & 0 \leq n \leq N-1 \\ x_{2N-n-1} & N \leq n \leq 2N-1. \end{cases} \tag{B.15}$$

Taking the $2N$-point DFT of the extended sequence y_n cf. (B.13) gives

$$\widehat{y}_k = \sum_{j=0}^{2N-1} y_j e^{-\iota k \frac{2\pi}{2N} j} = \frac{1}{2N} \left[\sum_{j=0}^{N-1} y_j e^{-\iota k \frac{2\pi}{2N} j} + \sum_{j=N}^{2N-1} y_{2N-j-1} e^{-\iota k \frac{2\pi}{2N} j} \right], \tag{B.16}$$

for $k = -N, ..., N-1$.

For the second sum on the right-hand-side of Eq. (B.16), the summation index may be changed, so that summation is over $0 < j < N$. Further it may used that $e^{\iota k 2\pi} = 1$ for $k \in \mathbb{Z}$ to rewrite it

$$\sum_{j=0}^{N-1} y_j e^{-\iota k \frac{2\pi}{2N}(2N-j-1)} = e^{\iota k \frac{2\pi}{2N}} \sum_{j=0}^{N-1} y_j e^{\iota k \frac{2\pi}{2N} j}. \tag{B.17}$$

By substitution Eq. (B.16) then becomes

$$\widehat{y}_k = \frac{1}{2N} e^{\iota \frac{k}{2} \frac{2\pi}{2N}} \sum_{j=0}^{N-1} y_j \left[e^{-\iota k \frac{2\pi}{2N}\left(j+\frac{1}{2}\right)} + e^{\iota k \frac{2\pi}{2N}\left(j+\frac{1}{2}\right)} \right] = e^{\iota \frac{k}{2} \frac{2\pi}{2N}} C_k, \tag{B.18}$$

where

$$C_k = \frac{1}{N} \sum_{j=0}^{N-1} \cos\left(\frac{\pi}{N} k \left[j + \frac{1}{2} \right] \right), \qquad \text{for } k = -N, ..., N-1. \tag{B.19}$$

Eq. (B.19) is the *discrete Cosine Transform of type 2* (DCT2).

Inverse transform

The IDFT of the discrete Fourier coefficients of the $2N$ sequence is

$$y_j = \sum_{k=-N}^{N-1} \widehat{y}_k e^{\iota k \frac{2\pi}{2N} j} = \sum_{k=0}^{N-1} \widehat{y}_k e^{\iota k \frac{2\pi}{2N} j} + \sum_{k=-N}^{-1} \widehat{y}_{-k} e^{\iota k \frac{2\pi}{2N} j} \tag{B.20}$$

for $j = 0, ..., N-1$.

Using that the output of a DFT of a real sequence is Hermitian symmetric

$$\widehat{y}_{-k} = \widehat{y}_k^* \tag{B.21}$$

and from Eq. (B.19) that $\widehat{y}_{-N} = 0$, Eq. (B.20) may be rewritten as

$$y_j = \widehat{y}_0 + \sum_{k=1}^{N-1} \widehat{y}_k e^{\iota k \frac{2\pi}{2N} j} + \sum_{k=-N}^{-1} \widehat{y}_k^* e^{-\iota k \frac{2\pi}{2N} j} = \Re\left\{ \widehat{y}_0 + 2 \sum_{k=1}^{N-1} \widehat{y}_k e^{\iota k \frac{2\pi}{2N} j} \right\}. \tag{B.22}$$

Finally, the substitution of Eq. (B.18) into Eq. (B.22) yields the *inverse discrete Cosine Transform of type 2* (IDCT2)

$$\begin{aligned} y_j =& \Re\left\{ C_0 e^{\iota \frac{k}{2} \frac{2\pi}{2N} j} + 2 \sum_{k=1}^{N-1} C_k e^{\iota k \frac{2\pi}{2N}\left(j+\frac{1}{2}\right)} \right\} && \text{(B.23)} \\ =& 2\left[\frac{1}{2} C_0 + \sum_{k=1}^{N-1} C_k \cos\left(\frac{\pi}{N} k \left[j + \frac{1}{2} \right] \right) \right], && \text{(B.24)} \\ \text{for } j =& 0, ..., N-1. \end{aligned}$$

B.2.2 DST-2

Forward transform

Similarly for the odd symmetric extension of the N-point real sequence x_n

$$y_n = \begin{cases} x_n & 0 \le n \le N-1 \\ -x_{2N-n-1} & N \le n \le 2N-1, \end{cases} \tag{B.25}$$

the $2N$-point DFT is

$$\widehat{y}_k = \frac{1}{2N} e^{\iota \frac{k}{2} \frac{2\pi}{2N}} \sum_{j=0}^{N-1} y_j \left[e^{-\iota k \frac{2\pi}{2N}\left(j+\frac{1}{2}\right)} - e^{\iota k \frac{2\pi}{2N}\left(j+\frac{1}{2}\right)} \right] = -\iota e^{\iota \frac{k}{2} \frac{2\pi}{2N}} S_k, \tag{B.26}$$

with S_k being the *discrete Sine Transform of type 2* (DST2)

$$S_k = \frac{1}{N} \sum_{j=0}^{N-1} \sin\left(k \frac{2\pi}{2N} \left[j + \frac{1}{2} \right] \right), \qquad \text{for } k = 0...N-1. \tag{B.27}$$

Inverse transform

The inverse transform corresponding to Eq. (B.26) is the IDFT of a $2N$ sequence Hermitian symmetric sequence for which $\widehat{y}_0 = 0$ cf. Eq. (B.27)

$$\begin{aligned} y_j =& \Re\left\{ \widehat{y}_0 + 2 \sum_{k=1}^{N-1} \widehat{y}_k e^{\iota k \frac{2\pi}{2N} j} + \widehat{y}_N e^{\iota N \frac{2\pi}{2N} j} \right\} && \text{(B.28)} \\ =& 2\left[\sum_{k=1}^{N-1} S_k \sin\left(k \frac{\pi}{N} \left[j + \frac{1}{2} \right] \right) + (-1)^j \frac{S_N}{2} \right] && \text{(B.29)} \\ \text{for } j =& 0, ..., N-1. \end{aligned}$$

B.2.3 DCT-4

Forward transform

DTTs of type 4 combines the even and odd extensions. E.g. symmetrical extension of the real sequence x_n evenly to the "left" (y_n) and subsequently oddly to the "right" (z_n) (see Fig. B.1) may be written

$$y_n = \begin{cases} x_n & 0 \le n \le N-1 \\ -x_{2N-n-1} & N \le n \le 2N-1 \end{cases} \tag{B.30}$$

$$z_n = \begin{cases} y_n & 0 \le n \le 2N-1 \\ y_{4N-n-1} & 2N \le n \le 4N-1. \end{cases} \tag{B.31}$$

Taking the DFT of z_n gives

$$\widehat{y}_k = \frac{1}{4N}\left[\sum_{j=0}^{N-1} y_j e^{-\iota k \frac{2\pi}{2N} j} - \sum_{j=N}^{2N-1} y_{2N-j-1} e^{-\iota k \frac{2\pi}{2N} j} - \sum_{j=2N}^{3N-1} y_{j-2N} e^{-\iota k \frac{2\pi}{2N} j} + \sum_{j=3N}^{4N-1} y_{4N-j-1} e^{-\iota k \frac{2\pi}{2N} j}\right], \quad \text{for } k = -2N, ..., 2N-1. \tag{B.32}$$

Again, by changing the summation index Eq. (B.32) becomes

$$\widehat{y}_k = \frac{1}{4N}\sum_{j=0}^{N-1} y_j \left(e^{-\iota k \frac{2\pi}{4N} j} - e^{-\iota k \frac{2\pi}{4N}(2N-j-1)} - e^{-\iota k \frac{2\pi}{4N}(j-2N)} + e^{-\iota k \frac{2\pi}{4N}(4N-j-1)}\right) \tag{B.33}$$

$$= \frac{1}{4N} e^{\iota \frac{k}{2} \frac{2\pi}{4N}} \left(1 - e^{-\iota k\pi}\right) \sum_{j=0}^{N-1} y_j \left(e^{-\iota k \frac{2\pi}{4N}\left(j+\frac{1}{2}\right)} + e^{\iota k \frac{2\pi}{4N}\left(j+\frac{1}{2}\right)}\right). \tag{B.34}$$

The term

$$1 - e^{-\iota k\pi} = \begin{cases} 2 & \text{for } n \text{ odd} \\ 0 & \text{for } n \text{ even} \end{cases} \tag{B.35}$$

in Eq. (B.34) implies that every other coefficient is zero. Hence the transform is computed for non-zero coefficients only, by introducing a new index from the relation $k = 2k' + 1$, as

$$\widehat{y}_{k'} = e^{\iota\left(k'+\frac{1}{2}\right)\frac{2\pi}{4N}} C_{k'}. \tag{B.36}$$

In Eq. (B.36) $C_{k'}$ is the *discrete Cosine Transform of type 4* (DCT4)

$$C_{k'} = \frac{1}{N}\sum_{j=0}^{N-1} \cos\left(\frac{\pi}{N}\left(k'+\frac{1}{2}\right)\left(j+\frac{1}{2}\right)\right), \qquad \text{for } k' = 0, 1, ..., N-1. \tag{B.37}$$

Inverse transform

Using that $\widehat{y}_0 = \widehat{y}_{2N} = 0$ cf. Eq. (B.37), the IDFT of the discrete Fourier coefficients of the $4N$ sequence corresponding to Eq. (B.36) is

$$\widehat{y}_j = \sum_{k=-2N}^{2N-1} \widehat{y}_k e^{\iota k \frac{2\pi}{4N} j} = \Re\left\{ 2 \sum_{k'=0}^{N-1} \widehat{y}_{2k'+1} e^{\iota(2k'+1)\frac{2\pi}{4N} j} \right\} \tag{B.38}$$

$$= 2 \sum_{k'=0}^{N-1} C_{k'} \cos\left(\frac{\pi}{N} \left(k' + \frac{1}{2} \right) \left(j + \frac{1}{2} \right) \right), \tag{B.39}$$

for $j = 0, ..., N-1$.

Eq. (B.39) is the *inverse discrete Cosine Transform of type 4* (IDCT4).

B.2.4 DST-4

Forward transform

Alternatively, the real sequence x_n symmetrically extended oddly to the "left" (y_n) and subsequently evenly to the "right" (z_n) (see Fig. B.1) is

$$y_n = \begin{cases} x_n & 0 \le n \le N-1 \\ x_{2N-n-1} & N \le n \le 2N-1 \end{cases} \tag{B.40}$$

$$z_n = \begin{cases} -y_n & 0 \le n \le 2N-1 \\ -y_{4N-n-1} & 2N \le n \le 4N-1. \end{cases} \tag{B.41}$$

The DFT of $z(t)$ then becomes

$$\widehat{y}_k = \frac{1}{4N} \sum_{j=0}^{N-1} y_j \left(e^{-\iota k \frac{2\pi}{4N} j} + e^{-\iota k \frac{2\pi}{4N}(2N-j-1)} - e^{-\iota k \frac{2\pi}{4N}(j-2N)} - e^{-\iota k \frac{2\pi}{4N}(4N-j-1)} \right) \tag{B.42}$$

$$= \frac{1}{4N} e^{\iota \frac{k}{2} \frac{2\pi}{4N}} \left(1 - e^{-\iota k \pi} \right) \sum_{j=0}^{N-1} y_j \left(e^{-\iota k \frac{2\pi}{4N}\left(j+\frac{1}{2}\right)} - e^{\iota k \frac{2\pi}{4N}\left(j+\frac{1}{2}\right)} \right), \tag{B.43}$$

for $k = -2N, ..., 2N-1$.

Again, it may be seen that the coefficients associated with every other mode is zero. Hence redundant modes are avoided by introducing a new index ($k = 2k' + 1$). Using this, Eq. (B.42) is rewritten as

$$\widehat{y}_{k'} = -\iota e^{\iota\left(k'+\frac{1}{2}\right)\frac{2\pi}{4N}} S_{k'}, \tag{B.44}$$

where the $S_{k'}$ is the *discrete Sine Transform of type 4* (DST4)

$$S_{k'} = \frac{1}{N} \sum_{j=0}^{N-1} \sin\left(\frac{\pi}{N} \left(k' + \frac{1}{2} \right) \left(j + \frac{1}{2} \right) \right), \qquad \text{for } k' = 0, 1, ..., N-1. \tag{B.45}$$

Inverse transform

Analogous to the derivation of Eq. (B.39), by substituting Eq. (B.45) into the IDFT of the discrete Fourier coefficients of the $4N$ sequence, the *inverse discrete Cosine Transform of type 4* (IDST4) is

$$y_j = 2\sum_{k'=0}^{N-1} S_{k'} \sin\left(\frac{\pi}{N}\left(k'+\frac{1}{2}\right)\left(j+\frac{1}{2}\right)\right), \tag{B.46}$$
$$\text{for } j = 0, ..., N-1.$$

B.2.5 Derivatives

Approximation of the derivative using the discrete coefficients obtained from a DTT may be derived from Eq. (B.12), but the appropriate inverse transform depends on the type of the forward transform used.

As in Eq. (B.22), Hermitian symmetry is used to evaluate Eq. (B.12) at the grid points as

$$\frac{d}{dx}\left\{I_{2N}y\right\}_j = \sum_{k=-N+1}^{N-1} (ik)\widehat{y}_k e^{\iota k\frac{2\pi}{4N}j} = \frac{1}{2N}\Re\left\{2\sum_{k=1}^{N-1}(ik)\widehat{y}_k e^{\iota k\frac{2\pi}{2N}j}\right\}. \tag{B.47}$$

By of substitution of the discrete Fourier coefficients representation as either Eq. (B.22) or Eq. (B.26) into Eq. (B.47), the inverse transform that restores the first order derivative is seen to be

$$\frac{d}{dx}\left\{I_{2N}y\right\}_j = \begin{cases} 2\sum_{k=1}^{N-1}\left[-k^n C_k\right]\sin\left(k\frac{\pi}{N}\left[j+\frac{1}{2}\right]\right) & C_k \text{ from (B.19)} \\ 2\left[\sum_{k=1}^{N-1}\left[k^n S_k\right]\cos\left(k\frac{\pi}{N}\left[j+\frac{1}{2}\right]\right)\right] & S_k \text{ from (B.24)}, \end{cases}$$
$$\text{for } j = 0, ..., N-1. \tag{B.48}$$

Similar for an $4N$-point representation as either Eq. (B.36) or Eq. (B.44)

$$\frac{d}{dx}\left\{I_{4N}y\right\}_j = \begin{cases} 2\sum_{k'=0}^{N-1}\left[-(2k'+1)C_{k'}\right]\sin\left(\frac{\pi}{N}\left(k'+\frac{1}{2}\right)\left(j+\frac{1}{2}\right)\right) & C_{k'} \text{ from (B.37)} \\ 2\sum_{k'=0}^{N-1}\left[(2k'+1)S_{k'}\right]\cos\left(\frac{\pi}{N}\left(k'+\frac{1}{2}\right)\left(j+\frac{1}{2}\right)\right) & S_{k'} \text{ from (B.45)} \end{cases}$$
$$\text{for } j = 0, ..., N-1. \tag{B.49}$$

Appendix C

Efficiency of the parallel Poisson solver in 3D

The efficiency of the Poisson solver for various boundary conditions has been tested for a problem in a cubic domain of unit side length resolved with N mesh points in all axis directions. The tests were carried out for Intel E5-2650 v4 (2.20GHz) processors. The time to solution has been reported in Fig. C.1(a) and the speedup in Fig. C.1(b). A completely unbounded solution is about 50% more expensive than when using a doubly-bounded condition in the first transform direction due to domain doubling ($N = 1024$) and 80% more expensive than when using the combination of doubly-bounded, unbounded and periodic conditions. The solver shows a good speedup for sufficiently large problems and indicates that a good parallel scalability is obtained with the parallel implementation outlined in Sec. 1.3. Fig. C.2 demonstrates that for a fixed numbers of CPU's ($N_{\text{CPU}} = 48$) the time to solution for the unbounded problem complies with an $\mathcal{O}(N_{\text{tot}} \log(N_{\text{tot}}))$ estimate, where $N_{\text{tot}} = N^3$ is the total number of mesh points.

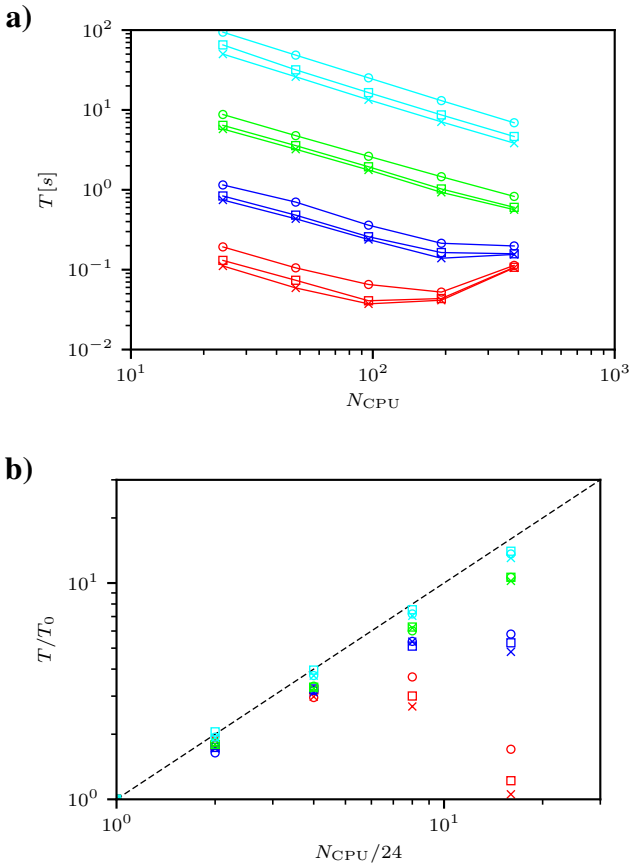

Figure C.1: Efficiency of parallel Poisson solver: (a) Time to solution plotted against number of CPU's used for parallel computation. (b) Speedup with indication of ideal speedup (- - -) . Lines indicate test problem with various unit resolutions; $N = 128$ (—) , $N = 256$ (—) , $N = 512$ (—) and $N = 1024$ (—) . Markers indicate boundary condition in x, y, z-directions as free-free-free (-○-) , bounded-free-free (-□-) and bounded-free-periodic (-×-)

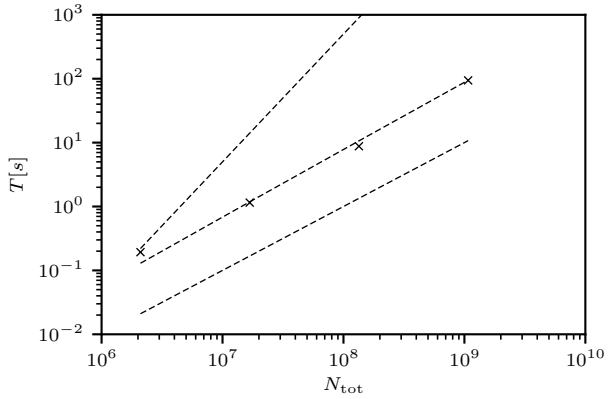

Figure C.2: Time to solution of completely unbounded Poisson solver for a test problem plotted against total number of grid points for fixed number of CPU's ($N_{\mathrm{CPU}} = 48$) (×) . The dashed lines from bottom to top indicate scaling as respectively $\mathcal{O}(N_{\mathrm{tot}})$, $\mathcal{O}(N_{\mathrm{tot}} \log(N_{\mathrm{tot}}))$ and $\mathcal{O}(N_{\mathrm{tot}}^2)$.

Bibliography

Anderson, R., Meneveau, C., 1999. Effects of the similarity model in finite-difference LES of isotropic turbulence using a lagrangian dynamic mixed model. Flow Turbulence and Combustion 62 (3), 201–225.

Angot, P., Bruneau, C.-H., Fabrie, P., 1999. A penalization method to take into account obstacles in incompressible viscous flows. Numer. Math. 81, 497–520.

Atsushi, O., 1982. Strouhal numbers of rectangular cylinders. J. Fluid Mech. 123, 379–398.

Backaert, S., Chatelain, P., Winckelmans, G., 2015. Vortex particle-mesh with immersed lifting lines for aerospace and wind engineering. IUTAM Symposium on Particle Methods in Fluid Dynamics 18, 1–7.

Barkley, D., Henderson, R. D., 1996. Three-dimensional Floquet stability analysis of the wake of a circular cylinder. J. Fluid Mech. 322, 215–241.

Batchelor, G. K., 1967. An Introduction To Fluid Dynamics, 1st Edition. Cambridge University Press.

Beale, J. T., 1988. On the accuracy of vortex methods at lage time. In: et al., B. E. (Ed.), Computational Fluid Dynamics and Reacting Gas Flows. Springer-Verlag, 19–32.

Bergdorf, M., 2007. Multiresolution particle methods for the simulation of growth and flow. Ph.D. thesis, ETH Zürich.

Bergdorf, M., Cottet, G.-H., Koumoutsakos, P., 2005. Multilevel adaptive particle methods for convection-diffusion equations. Multiscale Model. Simul. 4 (1), 328–357.

Berger, M. J., Colella, P., 1989. Local adaptive mesh refinement for shock hydrodynamics. J. Comput. Phys. 82 (1), 64–84.

Brachet, M., Meiron, D. I., Orszag, S. A., Nickel, B. G., Morf, R. H., Frisch, U., 1983. Small-scale structure of the Taylor-Green vortex. J. Fluid Mech. 130, 411–452.

Branlard, E., Papadakis, G., Gaunaa, M., Winckelmans, G., Larsen, T. J., 2015. Aeroelastic large eddy simulations using vortex methods: unfrozen turbulent and sheared inflow. J. Phys.: Conf. Ser. 625, 012019.

Bryan, G. L., et. al, 2014. ENZO: An adaptive mesh refinement code for astrophysics. Astrophysical Journal Supplement Series 211 (2), 19.

Cao, Y., Tamura, T., 2016. Large-eddy simulations of flow past a square cylinder using structured and unstructured grids. Computers and Fluids 137, 36–54.

Carrier, J., Greengard, L., Rokhlin, V., 1988. A fast adaptive multipole algorithm for particle simulations. SIAM J. Sci. Stat. Comput. 9 (4), 669–686.

Chapman, D. R., 1978. Computational aerodynamics development and outlook. Aiaa Journal 17 (12), 1293–1313.

Chasnov, J., 1991. Simulation of the Kolmogorov inertial subrange using an improved subgrid model. Phys. Fluids 3 (1), 188–200.

Chatelain, P., Backaert, S., Winckelmans, G., Kern, S., 2013. Large eddy simulation of wind turbine wakes. Flow, Turbul. Combust. 91, 587–605.

Chatelain, P., Curioni, A., Bergdorf, M., Rossinelli, D., Andreoni, W., Koumoutsakos, P., 2008. Billion vortex particle direct numerical simulations of aircraft wakes. Comp. Meth. Appl. Mech. & Engng. 197, 1296–1304.

Chatelain, P., Koumoutsakos, P., 2010. A Fourier-based elliptic solver for vortical flows with periodic and unbounded directions. J. Comput. Phys. 229, 2425–2431.

Choi, H., Moin, P., 2012. Grid-point requirements for large eddy simulation: Chapman's estimates revisited. Physics of Fluids 24 (1).

Cocle, R., Dufresne, L., Winckelmans, G., 2007. Investigation of multiscale subgrid models for LES of instabilities and turbulence in wake vortex systems. Lecture Notes in Computational Science and Engineering 56, 141–160.

Cocle, R., Winckelmans, G., Daeninck, G., 2008. Combining the vortex-in-cell and parallel fast multipole methods for efficient domain decomposition simulations. J. Comput. Phys. 227, 9091–9120.

Comte-Bellot, G., Corrsin, S., 1971. Simple eulerian time correlation of full-and narrow-band velocity signals in grid-generated, 'isotropic' turbulence. J. Fluid Mech. 48 (2), 273–337.

Coquerelle, M., Cottet, G.-H., 2008. A vortex level set method for the two-way coupling of an incompressible fluid with colliding rigid bodies. J. Comput. Phys. 227 (21), 9121–9137.

Cottet, G.-H., Koumoutsakos, P., 2000. Vortex Methods – Theory and Practice. Cambridge University Press, New York.

Cottet, G.-H., Poncet, P., 2003. Advances in direct numerical simulation of 3D wall-bounded flows by vortex-in-cell methods. J. Comput. Phys. 193, 136–158.

Couchman, H. M. P., 1991. Mesh-refined p3m: A fast adaptive n-body algorithm. The Astrophysical Journal 368, L23–L26.

Crochiere, R. E., Rabiner, L. R., 1981. Interpolation and decimation of digital signals - a tutorial review. Proc. IEEE 69 (3), 300–331.

El Ossmani, M., Poncet, P., 2010. Efficiency of multiscale hybrid grid-particle vortex methods. Multiscale Model. Simul. 8 (5), 1671–1690.

Frigo, M., Johnson, S., 2005. The design and implementation of FFTW3. Proceedings of the Ieee 93 (2), 216–231.

Gazolla, M., van Rees, W. M., Koumoutsakos, P., 2012. C-start: optimal start of larva fish. J. Fluid Mech. 698, 5–18.

Gazzola, M., Chatelain, P., van Rees, W. M., Koumoutsakos, P., 2011a. Simulations of single and multiple swimmers with non-divergence free deforming geometries. J. Phys. Chem. 230 (19), 7093–7114.

Gazzola, M., Chatelain, P., van Rees, W. M., Koumoutsakos, P., 2011b. Simulations of single and multiple swimmers with non-divergence free deforming geometries. J. Comput. Phys. 230, 7093–7114.

Germano, M., Piomelli, U., Moin, P., Cabot, W. H., 1991. A dynamic subgrid-scale eddy viscosity model. Phys. Fluids 3, 1760–1765.

Gholami, A., Malhotra, D., Sundar, H., Biros, G., 2016. FFT, FMM, or multigrid? a comparative study of state-of-the-art Poisson solvers for uniform and nonuniform grids in the unit cube. SIAM J. Sci. Comput. 38 (3), C280–C306.

Ghosal, S., Lund, T. S., Moin, P., Akselvoll, K., 1995. A dynamic localization model for large-eddy simulation of turbulent flows. J. Fluid Mech. 286, 229–255.

Gillis, T., Winckelmans, G., Chatelain, P., 2017. An efficient interative penalization method recycled Krylov subspaces and its application to impulsively started flows. J. Comput. Phys. 347, 490–505.

Gillis, T., Winckelmans, G., Chatelain, P., 2018. Fast immersed interface poisson solver for 3d unbounded problems around arbitrary geometries. J. Comput. Phys. 354, 403–416.

Goldstein, D., Handler, R., Sirovich, L., 1993. Modeling a no-slip flow boundary with an external force field. J. Comput. Phys. 105, 354–366.

Greengard, L., Rokhlin, V., 1987. A fast algorithm for particle simulations. J. Comput. Phys. 73, 325–348.

Hejlesen, M. M., February 2016. A high order regularisation method for solving the Poisson equation and selected applications using vortex methods. Ph.D. thesis, Technical University of Denmark.

Hejlesen, M. M., Koumoutsakos, P., Leonard, A., Walther, J. H., 2015a. Iterative Brinkman penalization for remeshed vortex methods. J. Comput. Phys. 280, 547–562.

Hejlesen, M. M., Rasmussen, J. T., Chatelain, P., Walther, J. H., 2013. A high order solver for the unbounded Poisson equation. J. Comput. Phys. 252, 458–467.

Hejlesen, M. M., Rasmussen, J. T., Chatelain, P., Walther, J. H., 2015b. High order Poisson solver for unbounded flows. Procedia IUTAM 18, 56–65.

Hejlesen, M. M., Rasmussen, J. T., Larsen, A., Walther, J. H., 2015c. On estimating the aerodynamic admittance of bridge sections by a mesh-free vortex method. J. Wind Eng. Ind. Aerodyn. 146, 117–127.

Hejlesen, M. M., Walther, J. H., 2016. A multiresolution method for solving the Poisson equation using high order regularization. J. Comput. Phys. 326, 188–196.

Hejlesen, M. M., Winckelmans, G., Walther, J. H., 2017. Non-singular Green's functions for the unbounded Poisson equation in 2d and 3d derived using spectral cut-off regularization. arXiv:1704.00704v1, 1–5.

Henderson, R. D., 1995. Details of the drag curve near the onset of vortex shedding. Phys. Fluids 7, 2102–2104.

Hockney, R. W., Eastwood, J. W., 1988. Computer Simulation Using Particles, 2nd Edition. Institute of Physics Publishing, Bristol, PA, USA.

Johnson, A. T., Patel, V. C., 1999. Flow past a sphere up to a Reynolds number of 300. J. Fluid Mech. 378, 19–70.

Kabadshow, I., 2012. Periodic boundary conditions and the error-controlled fast multipole method. Ias series volume 11, Forschungszentrum Jülich GmbH.

Kevlahan, N. K.-R., Ghidaglia, J.-M., 2001. Computation of turbulent flow past an array of cylinders using a spectral method with Brinkman penalization. Eur. J. Mech., B 20, 333–350.

Khadra, K., Angot, P., Parneix, S., Caltagirone, J. P., 2000. Fictitious domain approach for numerical modelling of Navier-Stokes equations. Int. J. Numer. Meth. Fluids 34, 651–684.

Kolomenskiy, D., Schneider, K., 2009. A fourier spectral method for the navier-stokes equations with volume penalization for moving solid obstacles. J. Comput. Phys. 228 (16), 5687–5709.

Kopriva, D. A., 2009. Implementing spectral methods for partial differential equations. Springer.

Koumoutsakos, P., 1997. Inviscid axisymmetrization of an elliptical vortex ring. J. Comput. Phys. 138, 821–857.

Koumoutsakos, P., Leonard, A., 1995. High-resolution simulation of the flow around an impulsively started cylinder using vortex methods. J. Fluid Mech. 296, 1–38.

Koumoutsakos, P., Leonard, A., Pépin, F., 1994. Boundary conditions for viscous vortex methods. J. Comput. Phys. 113 (1), 52–61.

Kundu, P. K., Cohen, I. M., Dowling, D. R., 2012. Fluid Mechanics, 5th Edition. Academic Press.

Langston, H., Greengard, L., Zorin, D., 2011. A free-space adaptive FMM-based PDE solver in three dimensions. Commun. Appl. Math. Comput. Sci. 6 (1), 79–122.

Larsen, A., Esdahl, S., Andersen, J. E., Vejrum, T., 2000. Storebælt suspension bridge - vortex shedding excitation and mitigation by guide vanes. J. Wind Eng. Ind. Aerodyn. 88, 283–296.

Larsen, A., Larose, G. L., 2015. Dynamic wind effects on suspension and cable-stayed bridges. J. Sound Vibration 334, 2–28.

Larsen, A., Walther, J. H., 1997. Aeroelastic analysis of bridge girder sections based on discrete vortex simulations. J. Wind Eng. Ind. Aerodyn. 67–68, 253–265.

Larsen, A., Walther, J. H., 1998. Discrete vortex simulation of flow around five generic bridge deck sections. J. Wind Eng. Ind. Aerodyn. 77–78, 591–602.

Lee, B., 1975. Effect of turbulence on surface pressure field of a square prism. J. Fluid Mech. 69 (MAY27), 263–282.

Leweke, T., Williamson, C. H. K., 1998. Cooperative elliptic instability of a vortex pair. J. Fluid Mech. 360, 85–119.

Lilly, D. K., 1967. The representation of small-scale turbulence in numerical simulation experiments,. IBM Scientific Computing Symposium on Environmental Sciences, –.

Luke, Y., 1962. Integrals of Bessel functions. McGraw Hill, Inc.

Lund, T., 2003. The use of explicit filters in large eddy simulation. Computers and Mathematics With Applications 46 (4), 603–616.

Luo, S., Chew, Y. T., Ng, Y. T., 2003. Characteristics of square cylinder wake transition flows. Phys. Fluids 15 (9), 2549–2559.

Lyn, D. A., Einav, S., Rodi, W., Park, J.-H., 1995. A laser-Doppler velocimetry study of ensemble-averaged characteristics of the turbulent near wake of a square cylinder. J. Fluid Mech. 304, 285–319.

Lyn, D. A., Rodi, W., 1994. The flapping shear layer formed by flow separation from the forward corner of a square cylinder. J. Fluid Mech. 267, 353–376.

Malhotra, D., Biros, G., 2015. PVFMM: A parallel kernel independent FMM for particle and volume potentials. Communications in Computational Physics 18 (3), 808–830.

Mansfield, J. R., Knio, O. M., Meneveau, C., 1998. A dynamic LES scheme for the vorticity transport equation: Formulation and *a Priori* tests. J. Comput. Phys. 145, 693–730.

Marichal, Y., Chatelain, P., Winckelmans, G., 2016. Immersed interface interpolation schemes for particle-mesh methods. Journal of Computational Physics 326, 947–972.

Martucci, S. A., 1994. Symmetrical convolution and the discrete sine and cosine transforms. IEEE Transactions on Signal Processing 42 (5), 1038–1051.

Matsumoto, M., 1996. Aerodynamic damping of prisms. Journal of Wind Engineering and Industrial Aerodynamics 59 (2–3), 159–175.

Meneveau, C., Lund, T. S., Cabot, W., 1996. A Lagrangian dynamic subgrid-scale model of turbulence. J. Fluid Mech. 319, 353–385.

Mimeau, C., Cottet, G. H., Mortazavi, I., 2016. Direct numerical simulations of three-dimensional flows past obstacles with a vortex penalization method. Computers & Fluids 136, 331–347.

Mimeau, C., Gallizio, F., Cottet, G. H., Mortazavi, I., 2015. Vortex penalization method for bluff body flows. Int. J. Numer. Meth. Fluids 79 (2), 55–83.

Monaghan, J. J., 1985. Extrapolating B splines for interpolation. J. Comput. Phys. 60 (2), 253–262.

Murakami, S., Iizuka, S., Ooka, R., 1999. Cfd analysis of turbulent flow past square cylinder using dynamic LES. Journal of Fluids and Structures 13 (7–8), 1097–1112.

Noca, F., Shiels, D., D., J., 1999. A comparison of methods for evaluating time-dependent fluid dynamic forces on bodies using only velocity fields and their derivatives. J. Fluids and Structures 13, 551–578.

Noca, F., Shiels, D., Jeon, D., 1997. Measuring instantaneous fluid dynamic forces on bodies, using only velocity fields and their derivatives. J. Fluids and Structures 11, 345–350, special brief note.

Norberg, C., 1993. Flow around rectangular cylinders: pressure forces and wake frequencies. J. Wind Eng. Ind. Aerodyn. 49, 187–196.

Passy, J.-C., Bryan, G. L., 2014. An adaptive particle-mesh gravity solver for ENZO. Astrophysical Journal Supplement Series 215 (1), 8.

Peskin, C., 1972. Flow patterns around heart valves: A numerical study. J. Comput. Phys. 10, 252–271.

Ploumhans, P., Winckelmans, G. S., 2000. Vortex methods for high-resolution simulations of viscous flow past bluff bodies of general geometry. J. Comput. Phys. 165, 354–406.

Ploumhans, P., Winckelmans, G. S., Salmon, J. K., Leonard, A., Warren, M. S., 2002. Vortex methods for direct numerical simulation of three-dimensional bluff body flows: Applications to the sphere at $Re = 300$, 500 and 1000. J. Comput. Phys. 178, 427–463.

Poncet, P., 2004. Topological aspects of the three-dimensional wake behind rotary oscillating circular cylinder. J. Fluid Mech., accepted.

Poncet, P., 2009. Analysis of an immersed boundary method for three-dimensional flow in vorticity formulation. J. Comput. Phys. 228, 7268–7288.

Porte-Agel, F., Meneveau, C., Parlange, M., 2000. A scale-dependent dynamic model for large-eddy simulation: application to a neutral atmospheric boundary layer. J. Fluid Mech. 415, 261–284.

Ramos-García, N., Spietz, H. J., Sørensen, J. N., Walther, J. H., 2018. Vortex simulations of wind turbines operating in atmospheric conditions using a prescribed velocity-vorticity boundary layer model. Wind Energy 21 (11), 1216–1231.

Rasmussen, J. T., Cottet, G.-H., Walther, J. H., 2011. A multiresolution remeshed vortex-in-cell algorithm using patches. J. Comput. Phys. 230 (17), 6742–6755.

Rasmussen, J. T., Hejlesen, M. M., Larsen, A., Walther, J. H., 2010. Discrete vortex method simulations of the aerodynamic admittance in bridge aerodynamics. J. Wind Eng. Ind. Aerodyn. 98, 754–766.

Rodi, W., 1997. Comparison of LES and RANS calculations of the flow around bluff bodies. J. Wind Eng. Ind. Aerodyn. 69, 55–75.

Rodi, W., Ferziger, J., Breuer, M., Pourquie, M., 1997. Status of large eddy simulation: Results of a workshop. Journal of Fluids Engineering-transactions of the Asme 119 (2), 248–262.

Rogallo, R. S., Moin, P., 1984. Numerical simulation of turbulent flows. Annu. Rev. Fluid Mech. 16, 99–137.

Rossinelli, D., Bergdorf, M., Cottet, G.-H., Koumoutsakos, P., 2010. GPU accelerated simulations of bluff body flows using vortex particle methods. J. Comput. Phys. 229 (89), 3316–3333.

Rossinelli, D., Hejazialhosseini, B., Sampinato, Daniele, G., Petros, K., 2011. Multicore/multi-GPU accelerated simulations of multiphase compressible flows using wavelets adapted grids. SIAM J. Sci. Comput. 33 (2), 512–540.

Saffman, P. G., 1992. Vortex Dynamics. Cambridge University Press.

Sagaut, P., 1998. Large Eddy Simulation for Incompressible Flows. Springer.

Scanlan, R. H., 1978. The action of flexible bridges under wind, I: Flutter theory. J. Sound Vibration 60 (2), 187–199.

Simiu, E., Scanlan, R. H., 1986. Wind Effects On Structures, 2nd Edition. John Wiley & Sons.

Simiu, E., Scanlan, R. H., 1996. Wind Effects on Structures: Fundamentals and Applications to Design. John Wiley & Sons.

Smagorinsky, J., 1963. General circulation experiments with the primitive equations, part I: the basic experiment. Monthly Weather Rev. 91 (3), 99–164.

Sohankar, A., Davidson, L., Norberg, C., 2000. Large eddy simulation of flow past a square cylinder: comparison of different subgrid scale models. J. Fluids Engng. 122, 39–47.

Sohankar, A., Norberg, C., Davidson, L., 1999. Simulation of three-dimensional flow around a square cylinder at moderate Reynolds numbers. Phys. Fluids 11 (2), 288–306.

Spietz, H. J., Hejlesen, M. M., Walther, J. H., June 2016. Simulation of bluff-body flows using iterative penalization in a multiresolution particle-mesh vortex method. In: ECCOMAS Congress 2016.

Spietz, H. J., Hejlesen, M. M., Walther, J. H., 2017a. Iterative Brinkman penalization for simulation of impulsively started flow past a sphere and a circular disk. J. Comput. Phys. 336, 261–274.

Spietz, H. J., Hejlesen, M. M., Walther, J. H., 2018. A regularization method for solving the Poisson equation for mixed unbounded-periodic domains. J. Comput. Phys. 356, 439–447.

Spietz, H. J., Walther, J. H., Hejlesen, M. M., November 2017b. A regularized vortex-particle mesh method for large eddy simulation. In: American Physical Society, 70th Annual Meeting of the Division of Fluid Dynamics. American Physical Society, Denver, Colorado.

Stolz, S., Adams, N. A., 1999. An approximate deconvolution procedure for large-eddy simulation. Phys. Fluids 11 (7), 1699–1701.

Stolz, S., Adams, N. A., Kleiser, L., 2001. An approximate deconvolution model for large-eddy simulation with application to incompressible wall-bounded flows. Phys. Fluids 13 (4), 997–1015.

Tamura, T., Miyagi, T., 1999. The effect of turbulence on aerodynamic forces on a square cylinder with various corner shapes. Journal of Wind Engineering and Industrial Aerodynamics 83 (1–3), 135–145.

Tan, B., Thompson, M., Hourigan, K., 2005. Evaluating fluid forces on bluff bodies using partial velocity data. Journal of Fluids and Structures 20 (1), 5–24.

Theodorsen, T., 1935. General theory of aerodynamic instability and the mechanism of flutter. TR 496, NACA.

Tomboulides, A., Orszag, S., 2000. Numerical investigation of transitional and weak turbulent flow past a sphere. J. Fluid Mech. 416, 45–73.

Trias, F. X., Gorobets, A., Oliva, A., 2015. Turbulent flow around a square cylinder at reynolds number 22,000: A DNS study. Computers and Fluids 123, 87–98.

van Rees, W. M., Leonard, A., Pullin, D. I., Koumoutsakos, P., 2011. A comparison of vortex and pseudo-spectral methods for the simulation of periodic vortical flows at high Reynolds numbers. J. Comput. Phys. 230, 2794–2805.

Vasilyev, O. V., De Stefano, G., Goldstein, D. E., Kevlahand, N. K. R., 2008. Lagrangian dynamic sgs model for stochastic coherent adaptive large eddy simulation. Journal of Turbulence 9 (11), 1–14.

Verma, A., Mahesh, K., 2012. A lagrangian subgrid-scale model with dynamic estimation of lagrangian time scale for large eddy simulation of complex flows. Physics of Fluids 24 (8).

Vico, F., Greengard, L., Ferrando, M., 2016. Fast convolution with free-space Green's functions. J. Comput. Phys. 323, 191–203.

Walther, J. H., Larsen, A., 1997. Two dimensional discrete vortex method for application to bluff body aerodynamics. J. Wind Eng. Ind. Aerodyn. 67–68, 183–193.

Wang, E. e. a., 2014. High-performance computing on the intel® xeon phi™. Springer International Publishing, Ch. 7, pp. 167–188.

White, F. M., 2011. Fluid Mechanics, 7th Edition. McGraw Hill, Inc.

Winckelmans, G., Cocle, R., Dufresne, L., Capart, R., 2005. Vortex methods and their application to trailing wake vortex simulations. C. R. Physique 6, 467–486.

Wray, A. A., Moin, P., Hunt, J. C. R., 1988. Eddies, streams, and convergence zones in turbulent flows. Center for Turbulence Research.

Wu, J. C., September 1978. A theory for aerodynamic forces and moments. Technical report, Georgia Institute of Technology.

Zaki, T. A., 2013. From streaks to spots and on to turbulence: Exploring the dynamics of boundary layer transition. Flow Turbulence and Combustion 91 (3), 451–473.

DTU Mechanical Engineering
Section of Fluid Mechanics, Coastal and Maritime Engineering
Technical University of Denmark

Nils Koppels Allé, Bld. 403
DK-2800 Kgs. Lyngby
Denmark
Phone (+45) 4525 1360
Fax (+45) 4588 4325
www.mek.dtu.dk
ISBN: 978-87-7475-536-4

DCAMM
Danish Center for Applied Mathematics and Mechanics

Nils Koppels Allé, Bld. 404
DK-2800 Kgs. Lyngby
Denmark
Phone (+45) 4525 4250
Fax (+45) 4593 1475
www.dcamm.dk
ISSN: 0903-1685